UNIVERSITÀ DEGLI STUDI DI PADOVA

Dipartimento di Fisica e Astronomia "Galileo Galilei"

Master Degree in Physics

Final Dissertation

A Systematic Analysis of the Charge Radii of Medium Mass Nuclei in the Shell Model Framework

Thesis supervisor

Prof. Silvia Monica Lenzi

Candidate

Giacomo Brignolo

Academic Year 2022/2023

Contents

Abstract

Due to the short range interaction of the nucleon-nucleon force, the nuclear surface is well delimited and therefore the nuclear radius. This fundamental nuclear property is so far, however, not satisfactorily described by microscopic nuclear methods. Theoretical models based on different approaches disagree in the predictions and with the available experimental data. In this thesis a systematic study of charge radii and isotopic shifts in nuclei with mass A=16-70 is performed in the framework of the shell model. Nowadays, with the advent of the radioactive beam facilities, it is possible to follow the behaviour of the charge radii as a function of the isospin along isotopic chains towards the drip lines. In the last years it has been put in evidence the fact that nuclear theoretical descriptions are unable to reproduce in detail the experimental findings. On the other hand, shell model analysis of the radii of mirror nuclei has shown very interesting and unexpected behaviour of the radii of single-particle orbits with low angular momentum value. In addition, it has been shown that due to the isovector monopole polarization, neutron and proton radii keep almost equal, independently of the neutron excess. Based on these evidences, a systematic analysis of isotopic shifts of nuclei with protons filling the sd and pf shells is performed in the framework of the shell model, using the available theoretical descriptions, in order to better understand the evolution of charge radii with respect to the isospin.

Chapter 1

Introduction

Even if the nuclear radius is a fundamental property of the nucleus, it is not well reproduced by microscopic calculations. This is not something peculiar of the nuclear system, but also the radii of atoms have puzzled physicist for a long time [1].
While for the atoms the interaction between the charged nucleus and the electrons is the well known electromagnetic one, when considering nuclei the interaction is very troubling, since the nuclear system, with the exception of the lightest nuclei, cannot be treated exactly and the nuclear force is not known analytically.

The density distribution of matter inside the nucleus is usually parameterized via a two-parameter Fermi function [2] (2pF):

$$\rho(r) = \frac{\rho_0}{1 + e^{(r-R)/a}}$$

where R is the half-density radius, a the diffuseness and ρ_0 a constant density. Clearly the mass number is given by $A = \int_0^\infty d^3r\ \rho(r)$. As it can be seen from Fig. 1.1 the distribution of matter inside the nucleus presents a characteristic saturation behaviour close to the center.

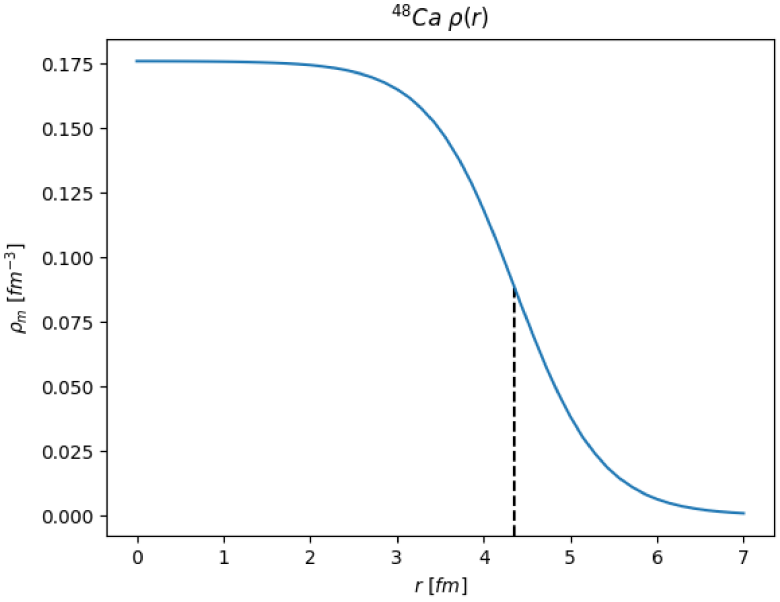

Figure 1.1: Matter density as a function of the radial distance r. In this figure an example of (matter) nuclear density distribution, parametrized as a 2pF function for ^{48}Ca, is shown, The typical values $\rho(0) = 0.176$ fm^{-3}, $a = 0.5$ fm and $R = 1.2A^{1/3}$ fm have been employed (see Ref. [2]). The dashed line is in correspondence of $r = R$.

The nuclear radius associated to the mass distribution inside the nucleus is known as the nuclear "matter" radius. The matter radius is difficult to measure directly, since to determine the distribution of both protons and neutrons one needs a probe which is sensitive to the strong force.
On the other hand the nuclear "charge" radius, that is defined by the distribution of the protons inside the nucleus, can be probed via electron elastic scattering. From these experiments the nuclear saturation properties have been unveiled [3].

However, constructing a target of nuclei is only feasible for stable or long-lived isotopes. An alternative approach, which can be used for exotic nuclei, is to use a beam of isotopes.
Thanks to the development of modern beam facilities, it is now possible to measure with great precision the nuclear charge radii, and in particular the *isotope shifts*, defined as the difference between the mean square charge radii of two isotopes of mass numbers A and A':

$$\delta\langle R_C^2\rangle^{AA'} = \langle R_C^2\rangle^{A} - \langle R_C^2\rangle^{A'} \tag{1.1}$$

where A' usually denotes a reference nucleus of which the charge radius is already known.
Studying a specific atomic transition of the isotopes via laser spectroscopy it is possible to determine directly the isotope shifts.
This basic property of the nucleus is very difficult to reproduce with the current nuclear theoretical methods, even by state of the art *ab initio* calculations.
In this work, the problem of calculating the isotope shifts will be tackled in the framework of the Shell Model, introducing recent developments inspired by phenomenological approaches.

A traditional approximation, due to Fermi, considering the nucleus as a spherical system, of the nuclear radius is (see for example Ref. [4]) $R = r_0 A^{1/3}$, where the constant r_0 is usually taken to be $r_0 \sim 1.1 - 1.2$ fm. This approximation, while giving an idea of the general behavior for the nuclear radii, does not reproduce the peculiar trends that can be seen in the experimental radii, in particular following an isotopic chain. An example of this is reported in Fig. 1.2, where the experimental charge radii for some isotopic chains are shown. It should be clear that the way that the charge radii evolve with the neutron number is not as straightforward as one might expect, and their theoretical determination needs a profound knowledge of the nuclear interaction's details.

The calcium isotopes are an area of great interest, especially after the discovery of the abrupt raise of the charge radius for neutron-rich nuclei after ^{48}Ca [7].
As can be seen from Fig. 1.3, which is taken from ref. [7], the nuclear charge radii are difficult to reproduce along an isotopic chain, even with state of the art *ab initio* (i.e. starting from "first principles" interactions) and DFT (density functional theory) methods.

The mechanism driving the peculiar trends seen in the experimental isotope shifts is not yet well understood. In some cases it is possible to attribute the difference in radii between neighboring isotopes to changes in the does not of nuclei, i.e. deformation. One well-studied isotopic chain is the Hg ($Z = 80$) one [8]. The isotope shifts can be seen in Fig. 1.4, which present a very distinct pattern in the mass region $A = 180 - 187$. In this region the addition of a single neutron produces dramatic effects on the shape of the nucleus (this is known as "shape staggering"), thus driving the staggering in the isotope shifts. As explained in Ref. [8] this happens because of the shape coexistence of a low-energy excited deformed state for even-even Hg isotopes, which becomes the ground state for an odd mass number.
While this can explain the behaviour of mercury isotope shifts, for calcium isotopes this explanation cannot hold. Ca isotopes are in fact characterized by a magic number of protons, thus they are of spherical shape. A new explanation and method of calculating the nuclear radii, especially in a Shell Model framework is needed.

Another important experimental hint, which further enriches the picture of nuclear radii, is the discovery of the peculiar "halo" nuclei. These nuclei, which are typically low mass, are characterised by one or two nucleons in a low angular momentum orbit weakly coupled to a well defined core. This

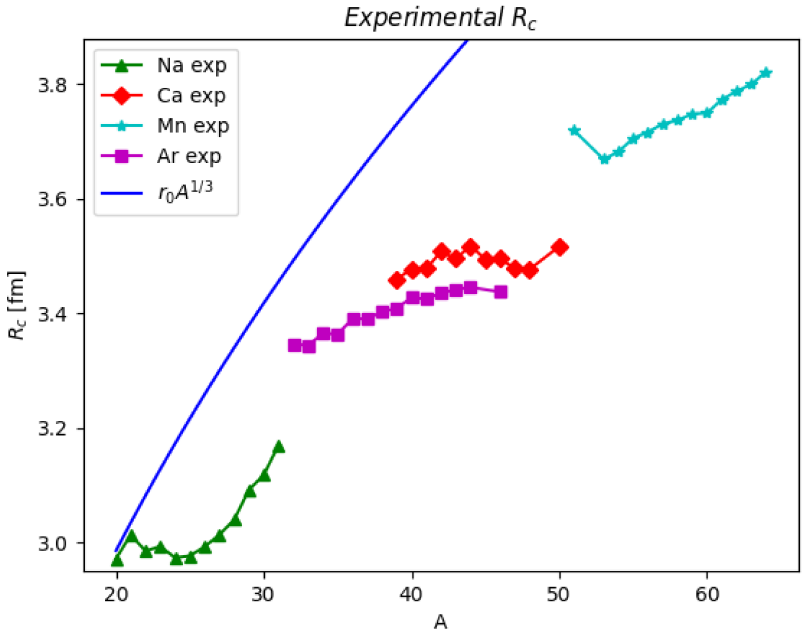

Figure 1.2: Charge radius as a function of the mass number A. In this figure the experimental charge radii for some isotopic chains covering the mass region $A = 20 - 64$; data taken from [5] and [6].

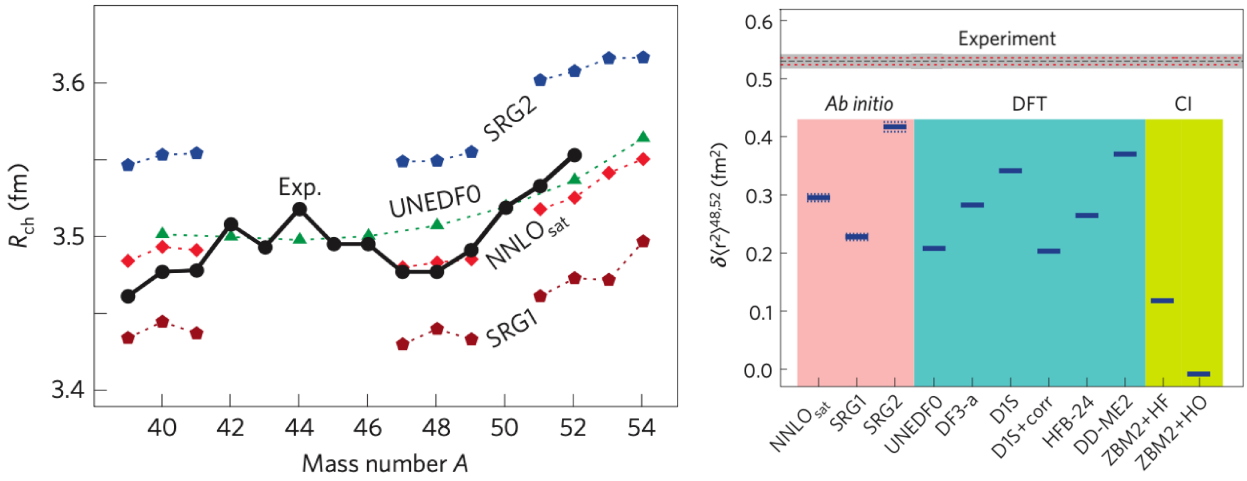

(a) (b)

Figure 1.3: (a) Isotope shifts as a function of the mass number A. (b) Isotope shifts $\delta\langle r^2\rangle^{48,52}$ for different interactions. In these two figures, adapted from Ref. [7], experimental and theoretical results of the Calcium isotopes are presented. On the left the nuclear charge radii (experimental data in black solid line) are reported. On the right the isotope shift $\delta\langle r^2\rangle^{48,52} = \langle r^2\rangle^{48} - \langle r^2\rangle^{52}$ is compared with theoretical predictions, in particular with *ab initio* methods, density functional theory (DFT) and configuration interaction (CI).

weak bound between the core and the halo nucleon(s) allows the latter to have a much larger spatial spreading.

Another interesting fact is that very light nuclei, up until ^{12}C and ^{16}O, probably present a cluster structure. In fact, for these nuclei cluster calculations have been successful.
Their cluster structure highly impact the nuclear radii, which in turn are not reproduced by Shell Model calculations.

With these insights this work's aim is to explore different prescriptions, in the the Shell Model framework, through a systematic analysis of the isotope shifts in medium mass nuclei.

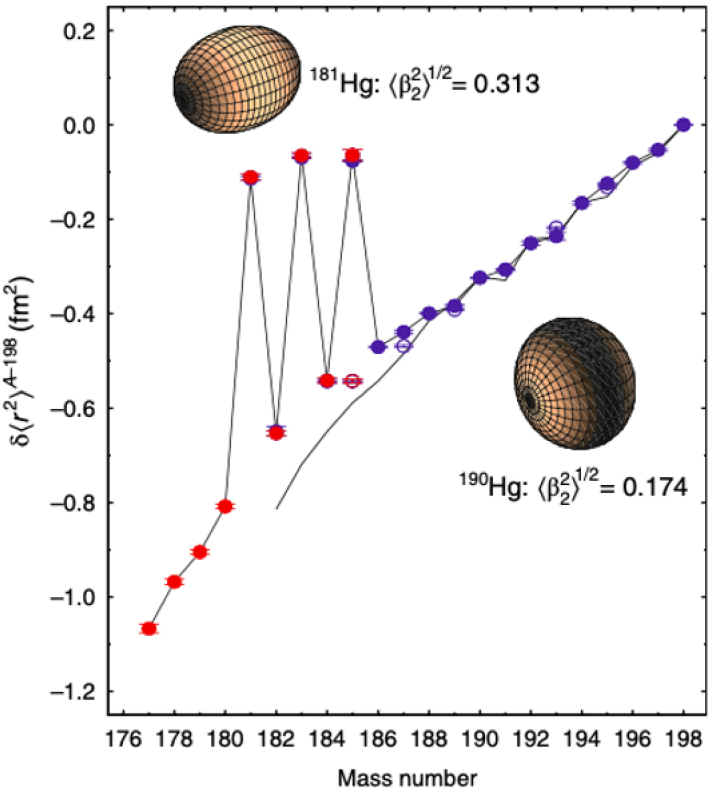

Figure 1.4: Isotope shifts as a function of the mass number. Figure adapted from Ref. [8], showing the experimental isotope shifts, obtained via laser spectroscopy of Hg isotopes with ^{198}Hg as reference. The data is extracted from two different works, Ref. [8] (reported in red circles) and Ref. [9] (reported in blue circles). The difference between filled and empty circles is that for the former the measured state is the ground state and in the latter it is an isomeric state, for both sets of data. Finally, the black solid line reports the results for Pb isotopes ($Z = 82$), measured in Ref. [10], as a comparison with the quasi-spherical trend. One can notice that the error bars are appreciably small. This works show the interesting link of increase in radius to the deformation of the nuclei.

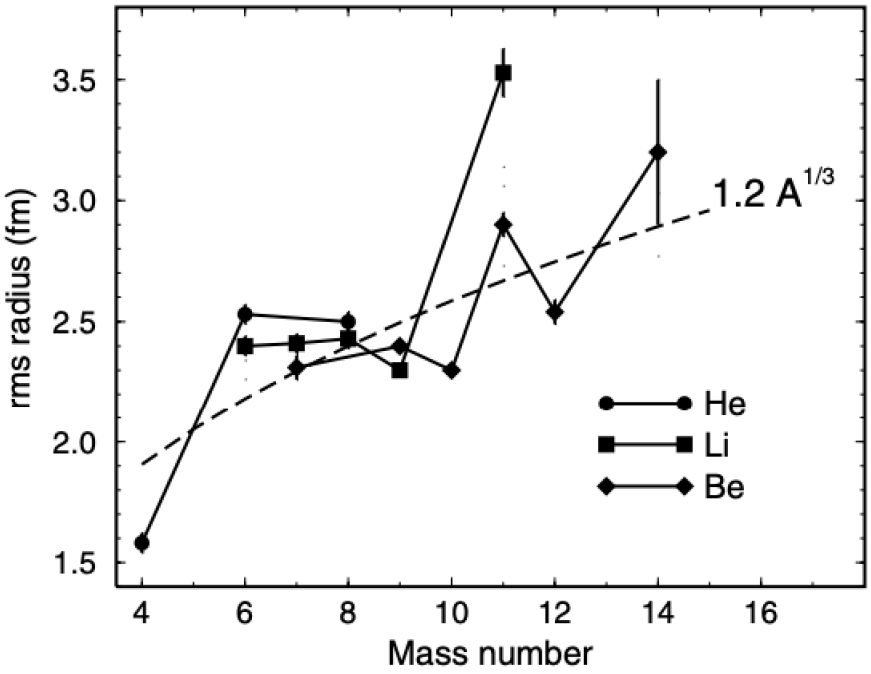

Figure 1.5: Experimental RMS radii of the He, Li and Be nuclei as a function of the mass number. This unveils the "halo" structure, which drives the sudden increase of the observed radius. Image taken from [11].

In Chapter 2 the Shell Model will be introduced, explaining the basics of the theory as well as giving insights about how Shell Model calculations are performed. The relevant effective interactions used to describe the various isotopes will be reported.
In Chapter 3 the problem of calculating the nuclear charge radius will be tackled in both a macroscopic and microscopic approach. In the former approach the main focus will be the Duflo-Zuker [12] phenomenological prescription, a five parameter formula able to reproduce a large number of charge radii. In the latter the challenging task of calculating the isotope shifts in the Shell Model framework will be discussed, following the recent theoretical works [13, 14].
Finally, in Chapter 4 the methods will be applied to a variety of isotopic chains and the result discussed.

Chapter 2

Nuclear Shell Model

In this chapter the nuclear Shell Model (SM) theory, as well as the code used for the calculations, will be presented. The solutions of the Schrödinger equation will give information regarding the behavior of the nucleons inside the nucleus. These information will play a crucial role in determining the nuclear radius, as it is going to be explained in Chapter 3.

2.1 The Non-Interacting Shell Model

The Shell Model (SM) is a microscopic approach in order to treat nuclear systems, which are strongly-interacting quantum many-body systems, first developed in [15] and [16] in order to explain the shell structure and the nuclear "magic numbers".
An exact treatment for the Schrödinger of an A body system is possible only for the lightest nuclei, so one has to resort to a certain degree of approximation; this is due to computational problems, for example the interaction matrix may be too large to be diagonalized.

The non-interacting Shell Model, also referred to as single-particle SM or independent particle SM, is justified by the mean field approximation, considering a single nucleon under the influence of a central mean field generated by the other $A-1$ nucleons present in the nucleus.
Considering the hamiltonian:

$$H_0 = \sum_{i=1}^{A} h_{0i} = \sum_{i=1}^{A} (T_i + U_i) \tag{2.1}$$

where the h_{0i} are the single-particle hamiltonians, sum of the single-particle kinetic term T_i and the single-particle potential U_i.
The single-particle wavefunctions are the solutions of the eigenproblem:

$$h_{0i}\phi_i = \epsilon_i \phi_i \tag{2.2}$$

with ϵ_i the single-particle energy of the i^{th} nucleon.
The many-body wavefunction representing the nuclear state is taken as the anti-symmetrized many-body wavefunction, i.e. the Slater determinant of the single particle wavefunctions of the nucleons:

$$\Psi(\vec{r}_1, \ldots, \vec{r}_A) = \frac{1}{\sqrt{A!}} \det \begin{pmatrix} \phi_1(\vec{r}_1) & \ldots & \phi_A(\vec{r}_1) \\ \phi_1(\vec{r}_2) & \ldots & \phi_A(\vec{r}_2) \\ \vdots & \ddots & \vdots \\ \phi_1(\vec{r}_A) & \cdots & \phi_A(\vec{r}_A) \end{pmatrix} \tag{2.3}$$

where A is the mass number of the nucleus, Ψ is the many-body wavefunction and ϕ the single-particle one.
This approximation can be justified since the mean free path of nucleons inside the nucleus is of the

order of the nuclear radius itself, so they behave like a non-interacting Fermi gas.

In this way, the full eigenproblem can be written as:

$$H_0 \left|\Psi\right\rangle = E \left|\Psi\right\rangle \tag{2.4}$$

where E is the total energy of the many-particle state, $E = \sum_i \epsilon_i$.

2.1.1 The Nuclear Potential

The choice of the single-particle potential that appears in the eigenproblem needs to explain the experimental evidence of the shell structure. Since the theory governing the nucleons cannot be solved analytically, one has to resort to an approximate form.
A typical choice is the Woods-Saxon potential [17]:

$$V(r) = -\frac{V_0}{1 + e^{(r-R)/a}} \tag{2.5}$$

where V_0 is a constant representing the value of the potential in the center of the nucleus, R describes the range of the potential (as a first approximation $R = 1.1 - 1.2A^{1/3}$) and a represents the surface thickness.
This parametrization of the potential takes the form of the one used to describe the matter density distribution inside the nucleus.
The parameters of the Woods-Saxon potential can be fitted in order to obtain a phenomenological realistic potential.
A spin-orbit coupling term is also added to the single particle potential. To account for the surface nature of this coupling, a usual choice is [4]:

$$V_{\ell s} \propto \frac{dV(r)}{dr} \vec{\ell} \cdot \vec{s} \tag{2.6}$$

where $\vec{l}$ and $\vec{s}$ are the angular momentum and spin vector of the nucleon. The effect of the spin-orbit coupling consists splitting the orbits of a given ℓ quantum number into two orbits, respectively with total angular momentum $j = \ell \pm 1/2$.

Although the Woods-Saxon potential describes well the shell structure, it is not analytically solvable. Thus, other approximate forms of the potential can be considered. Another choice for the potential, firstly proposed in [15, 16] consists in:

$$U = \frac{1}{2}\mu\omega^2\vec{r}^2 + C\vec{l} \cdot \vec{s} + D\vec{\ell} \cdot \vec{\ell} \tag{2.7}$$

where the first term is a $3D$ isotropic harmonic oscillator potential of a particle of mass μ and with oscillation frequency ω, and C and D are dimensional quantities.
Considering only the harmonic oscillator potential one would obtain the wrong magic numbers: that is why there are two more terms added. The second term is the the spin-orbit interaction responsible for the splitting of the levels accordingly to their total angular momentum j. The third term $\vec{\ell} \cdot \vec{\ell}$ is added in order to mimic the Woods-Saxon orbits.

Focusing on the first term of Eq. (2.7), that represents an isotropic $3D$ quantum harmonic oscillator, the eigenfunctions of $\hat{H}\psi = E\psi$ can be chosen to be also eigenfunctions of the square angular momentum and its projection over the z axis. This happens because the potential is spherically symmetric. Namely:

$$\begin{cases} \hat{\vec{L}}^2\psi = \hbar^2\ell(\ell+1)\psi \\ \hat{L}_z\psi = \hbar m_\ell \psi \end{cases} \tag{2.8}$$

The solution of the Schrödinger equation for a harmonic oscillator potential can be written in spherical coordinates as:

$$\hat{H}\psi_{n\ell m_\ell} = \left\{ -\frac{\hbar^2}{2\mu}\nabla^2 + \frac{1}{2}m_\ell\omega^2 r^2 \right\} \psi_{n\ell m_\ell} = E_{n\ell}\psi_{n\ell m_\ell} \tag{2.9}$$

with $\psi_{n\ell m_\ell} = R_{n\ell}(r)Y_{\ell m_\ell}(\theta,\phi)$, where $R_{n\ell}$ is the radial part and $Y_{\ell m_\ell}(\theta,\phi)$ are the spherical harmonics. Explicitly the wavefunctions are:

$$\psi_{n\ell m_\ell}(r,\theta,\phi) = R_{n\ell}Y_{\ell m}(\theta,\phi)N_{n\ell}r^\ell L_n^{\ell+1/2}(2\nu r^2)Y_{\ell m_\ell}(\theta,\phi) \tag{2.10}$$

where θ and ϕ are the polar and azimuthal angles, $\nu = \mu\omega/2\hbar$, $L_n^{\ell+2}(2\nu r^2)$ are the generalised Laguerre polynomials, and

$$N_{n\ell} = \sqrt{\sqrt{\frac{2\nu^3}{\pi}}\frac{2^{n+2\ell+3}k!\nu^\ell}{(2(k+\ell)+1)!!}} \tag{2.11}$$

is a normalisation factor.

The energy levels E_{nl} can be described by a single quantum number, the principal quantum number p[1]: $E_p = (p+3/2)\hbar\omega$, where $p = 2n+\ell$, with $n = n_x + n_y + n_z$ is the number of nodes and ℓ the orbital angular momentum of the state.
For a given level $p \geq 0$ we can have $0 \leq \ell \leq p$, and since $p = 2n+\ell$ if p is odd then ℓ must be odd.
The usual notation for the state is $\ell = 0,1,2,3,4,\cdots = s,p,d,f,g,\ldots$
This gives rise to the well known degenerate energy levels, where the degeneration is given by the fact that the harmonic oscillator is isotropic and the nucleons are spin-1/2 particles; the degeneracy of a principal shell (i.e. determined by p) is given by $D_p = (p+1)(p+2)$.

Adding now the second term of Eq. (2.7), we are considering the spin-orbit interaction, and in this case the conserved quantum number is the total angular momentum $j = \ell + s$. The total wavefunction takes the form:

$$\Psi_{jn\ell m}(r) = R_{n\ell}\left[Y^\ell \otimes \chi^s\right]_m^j \tag{2.12}$$

where $R_{n\ell}$ refers to the radial part, Y are the spherical harmonics and χ the spinorial part. The

$$\left[Y^\ell \otimes \chi^s\right]_m^j = \sum_{m_\ell m_s} \langle \ell m_\ell, s m_s | j m\rangle \, Y_{\ell m_\ell}\chi_{s m_s} \tag{2.13}$$

where $m = j_z$, $m_\ell = \ell_z$ and $m_s = s_z$ are the projections along the z-axis of the total angular momentum, orbital angular momentum and spin respectively.
The introduction of the spin-orbit coupling splits the levels: since it can have total angular momentum $j = l \pm 1/2$. This coupling enters the hamiltonian as: $V_{\ell s} = C\vec{l}\cdot\vec{s}$, with $C < 0$.
This way, when considering the effect of this coupling on a state $|\Psi\rangle$, one gets:

$$2\vec{l}\cdot\vec{s}\,|\Psi\rangle = \hbar^2\left[(\vec{l}+\vec{s})^2 - (\vec{s})^2 - (\vec{l})^2\right]|\Psi\rangle = \hbar^2\left[j(j+1) - s(s+1) - \ell(\ell+1)\right]|\Psi\rangle \tag{2.14}$$

where the usual law for the square of a sum was used, as well as $\vec{j} = \vec{\ell} + \vec{s}$.
At this point there are two possibilities: $j = \ell + 1/2$ or $j = \ell - 1/2$:

$$\begin{cases} j = \ell + 1/2 \Rightarrow 2\vec{\ell}\cdot\vec{s}\,|\Psi\rangle = l\hbar^2\,|\Psi\rangle \\ j = \ell - 1/2 \Rightarrow 2\vec{\ell}\cdot\vec{s}\,|\Psi\rangle = -(l+1)\hbar^2\,|\Psi\rangle \end{cases} \tag{2.15}$$

Since the spin-orbit term enters the hamiltonian with an overall negative sign, the energy will be higher for a state with $j = \ell - 1/2$ with respect to the state with $j = \ell + 1/2$. This way the spin-orbit

[1] This is the notation usually employed in the works relevant for this thesis, as in [14, 12, 13]; in other contexts the principal quantum number is usually denoted as N.

interaction breaks the degeneracy.
The substructure created by the splitting due to the spin-orbit coupling are often referred to as orbits, and each orbit of total angular momentum j will have a degeneracy of $D_j = 2j + 1$, for each particle species, due to the possible projections on the third axis.

The addition of the third term $D\vec{\ell} \cdot \vec{\ell}$ changes the energy of the orbits accordingly to their orbital angular momentum ℓ, since

$$\vec{\ell} \cdot \vec{\ell} \, |\Psi\rangle = \hbar^2 \ell(\ell + 1) \, |\Psi\rangle$$

This is added to recover the correct energy spacing of the orbits.

Putting together all these information the structure of the nuclear orbits is described as reported in Fig. 2.1. This agrees with the experimental evidences, in particular with the magic numbers.

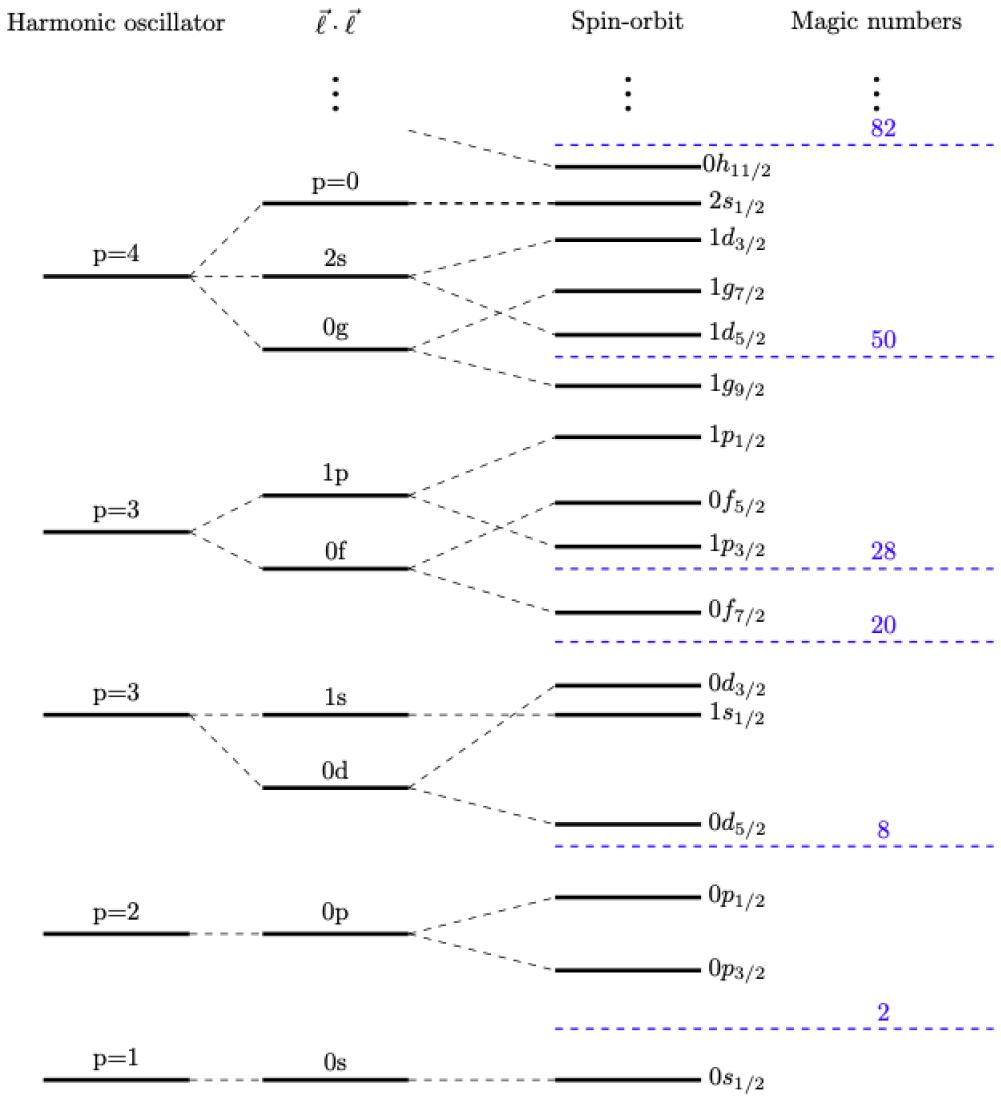

Figure 2.1: Shell Model orbits. In this figure from left to right are present the harmonic oscillator major shells, which are then split by the addition of the spin-orbit interaction (Eq. (2.7)). On the far right the "magic numbers" obtained by the spin-orbit coupling are reported.

In Fig. 2.2 the comparison between the Woods-Saxon potential and the harmonic oscillator can be appreciated.

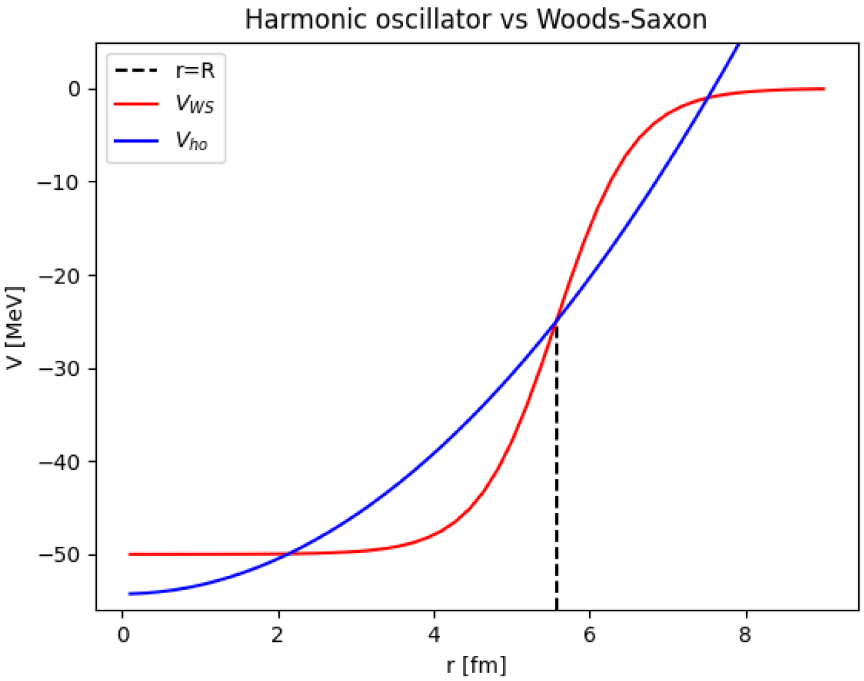

Figure 2.2: Potential as a function of the radial distance r. In this figure a comparison between the harmonic oscillator potential and the Woods-Saxon one is reported. For the Woods-Saxon form, Eq. (2.5), the parameter used are $V_0 = 50$ MeV, $R = 1.1A^{1/3}$ has been chosen (with $A = 100$), and $a = 0.50$ fm. For the harmonic oscillator $\hbar\omega = 8.83$ MeV has been chosen (consistently with the Bohr-Mottelson approximation for $A = 100$), and it has been re-scaled by a constant term, $V_1 = -54.25$ MeV, in order to have the two forms coincide at $r = R$.

2.2 The Interacting Shell Model

The non-interacting Shell Model can work relatively well considering only one closed shells and a nucleon above it. When one has to deal with more than one nucleon the effects of the interaction between them needs to be considered.
However the formalism, as noted in Ref. [18], is still helpful when dealing with more complex systems; the harmonic oscillator orbits define the basis for the many-body Slater determinants in the so-called m-scheme. This will allow to a formulation of the Schrödinger problem in a number representation, and it will be relevant in the following.

In the interacting Shell Model, two-body forces are considered. A common method to obtain the two-body force is to start from a realistic potential, which should fit the data coming from nucleon-nucleon (NN) scattering [19].
Usually these potentials cannot be plugged in the hamiltonian directly, because of the peculiar strong short-range repulsion of the nuclear force; a regularisation procedure has to be employed, in order to overcome these issues.
Schematically, a possible procedure used to construct the interacting SM hamiltonian can be stated as:

- one starts with a realistic bare nucleon-nucleon interaction, V_{NN}, which fits the data coming from NN scattering experiments
- following the methods used in effective field theory, the potential is smoothed-out by integrating out the high-momentum part (i.e. the short-range part), obtaining the potential V_{low-k} (see Ref. [20])
- starting from V_{low-k}, an effective interaction is obtained to be used for the nuclear shell model

calculations

The full nuclear problem, considering all the possible orbits that can be occupied by a nucleon, would be infinite-dimensional. Thus, one must work in a restricted Hilbert space, choosing to consider only a limited amount of orbits, as it will be discussed in more detail afterwards.

A second procedure used in order to obtain the interaction consists in starting from the empirical data, fitting the interaction's matrix elements; this is for example the case of the USDa interaction [21].

Model Space and Effective Hamiltonian

Let's consider two-body interactions; the hamiltonian of an A-nucleon system then reads

$$H = \sum_{i}^{A} T_i + \sum_{i<j}^{A} V_{ij} \tag{2.16}$$

where T_i is the kinetic energy of the i^{th} nucleon and V_{ij} is the interaction potential between the i^{th} and j^{th} nucleons.
The Schrödinger equation can be written as:

$$H\left|\Psi\right\rangle = \left(\sum_{i}(T_i + U_i) + \sum_{i<j} V_{ij} - \sum_{i} U_i\right)\left|\Psi\right\rangle = E\left|\Psi\right\rangle \tag{2.17}$$

where $|\Psi\rangle$ is the many-body state, and an auxiliary single-body potential, U_i, has been added and subtracted. Such a potential can be chosen in a way such that $H_1 = \sum_{i<j} V_{ij} - \sum_i U_i$, i.e. the perturbed hamiltonian, is much smaller than the unperturbed one, i.e. $H_0 = \sum_i (T_i + U_i)$. In this way a perturbative approach can be justified.

The energy E appearing in Eq. (2.17) is the true energy of the system. As already observed, one cannot really treat the full problem, so working in a restricted space is mandatory. To simplify the system the full Hilbert space can be divided into two subspaces. Only one of them will be considered. With this procedure the eigenproblem will be defined on a so-called model space. In this way, one can consider only the projections of the states $|\Psi'\rangle$ into the subspace, requiring:

$$H_{eff}\left|\Psi'\right\rangle = E\left|\Psi'\right\rangle \tag{2.18}$$

where H_{eff} is the effective hamiltonian, and E should be the same energy as the full problem.
The model space is specified by an inert core and a valence space.
The inert core is the interacting vacuum of the theory, made of the fully-occupied orbits; the nucleons inside the inert core are "frozen" and cannot jump to other orbits. Outside the inert core the nucleons can be arranged in different configurations in the valence space. Outside the valence space the orbits cannot be occupied: this can be called external space.
The choice of valence space should be made in a way so that the system is simple enough to be treatable, while still containing all the relevant degrees of freedom.

Working in the model space, the effective hamiltonian can be written as

$$H_{eff} = H_0 + H_{res} = \sum_{i=1}^{A} h_0(i) + H_{res} \tag{2.19}$$

where $h_0(i)$ are the single-particle hamiltonians and H_{res} is the residual hamiltonian.
The total energy of the system can be split into two contributions: $H\left|\Psi\right\rangle = (H_0 + H_{res})\left|\Psi\right\rangle = E\left|\Psi\right\rangle =$

$(E_0 + E_{res})\,|\Psi\rangle$.

One can construct a basis of eigenstates $|\phi_i\rangle$ of the single-particle hamiltonians, each with eigenvalue ϵ_i:

$$h_0(i)\,|\phi_i\rangle = \epsilon_i\,|\phi_i\rangle \tag{2.20}$$

The many-body (anti-symmetric) wavefunction can be constructed as the Slater determinant of the single-particle wavefunctions:

$$\psi_k^0 = \frac{1}{\sqrt{A!}} \det \begin{pmatrix} \phi_1(\vec{r_1}) & \cdots & \phi_1(\vec{r}_A) \\ \vdots & \ddots & \vdots \\ \phi_A(\vec{r_1}) & \cdots & \phi_A(\vec{r}_A) \end{pmatrix} \tag{2.21}$$

where the index k indicates the particular configuration of the many-body state of the system, and obeys the Schrödinger equation $H_0\,|\psi_k^0\rangle = E_k^0\,|\psi_k^0\rangle$, with $E_k^0 = \sum_{i=1}^{A} \epsilon_i$.

Configurations

The possible configurations specify what valence orbits of the model space are occupied by which valence nucleon. The configurations can also include particle-holes pairs. Usually, configurations are represented with the following notation:

$$|\pi(\alpha_1^{m_1} \cdots \alpha_r^{m_r}) \otimes \nu(\beta_1^{n_1} \cdots \beta_s^{n_s})\rangle \tag{2.22}$$

where π and ν indicate the fluids (protons and neutrons respectively), α and β are the valence orbits occupied and m, n the number of protons and neutrons respectively that occupy the orbits. In the *sd* shell the valence space is composed of the orbits $0d_{5/2}$, $1s_{1/2}$ and $0d_{3/2}$, and taking for example ${}^{20}_{11}Na$ some possible configurations are:

$$\left|\pi(0d_{5/2}^3) \otimes \nu(0d_{5/2}^1)\right\rangle, \quad \left|\pi(0d_{5/2}^2 1s_{1/2}^1) \otimes \nu(0d_{5/2}^1)\right\rangle, \quad \left|\pi(0d_{5/2}^3) \otimes \nu(0d_{3/2}^1)\right\rangle, \quad \ldots \tag{2.23}$$

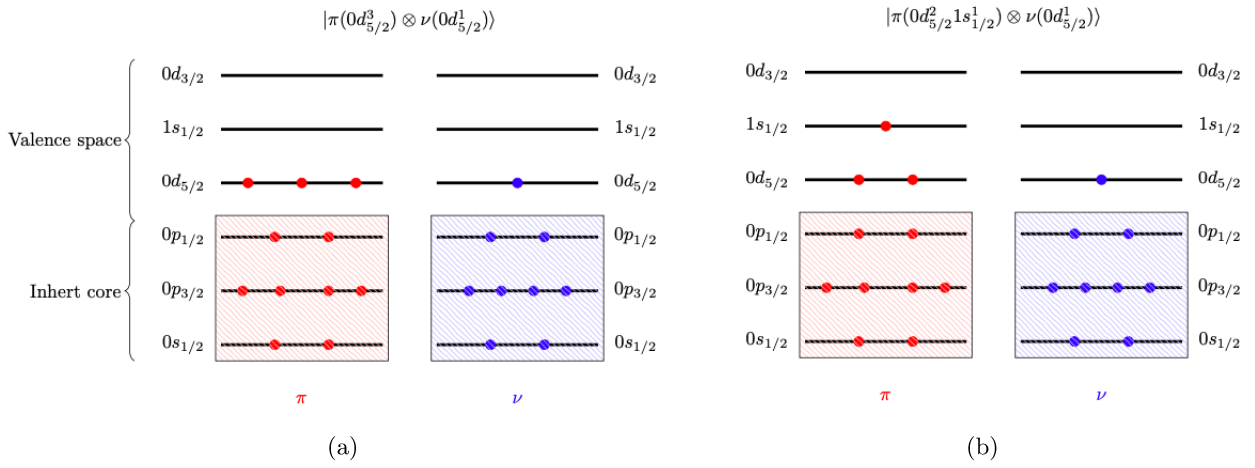

Figure 2.3: Visual representation of two possible configurations for ^{20}Na, where the inert core and the valence space are highlighted. The external space is composed of all the other higher energy orbits not shown

It is clear that the number of configurations rapidly increases with the dimension of the valence space. The full many-body wavefunction will then be constructed by summing over all the possible configurations:

$$|\Psi_p\rangle = \sum_k a_{pk}\,|\psi_k^0\rangle \;\text{ such that }\; \sum_k a_{pk}^2 = 1 \tag{2.24}$$

and the probability that the system will be in the configuration k is given by the square of the amplitude, i.e. $P_k = a_{pk}^2$.

The Schrödinger equation can be rewritten as:

$$H\left|\Psi_p\right\rangle = E_p\left|\Psi_p\right\rangle = E_p\sum_{k=1}^{n} a_{pk}\left|\psi_k^0\right\rangle \iff \sum_{k=1}^{n} a_{pk}\left\langle\psi_l^0\right| H\left|\psi_k^0\right\rangle = E_p a_{lp} \tag{2.25}$$

where both sides of the equation have been multiplied by $\left\langle\psi_l^0\right|$ and the orthonomality conditions $\left\langle\psi_l^0|\psi_k^0\right\rangle = \delta_{lk}$ have been used.
Since $\left|\psi_k^0\right\rangle$ is an eigenfunction of the unperturbed hamiltonian of eigenvalue E_k^0, the matrix elements of the hamiltonian $H_{lk} = \left\langle\psi_l^0\right| H\left|\psi_k^0\right\rangle = \left\langle\psi_l^0\right| H_0 + H_{res}\left|\psi_k^0\right\rangle$ can be split into a diagonal and an off-diagonal part, $H_{lk} = E_k^0\delta_{lk} + \left\langle\psi_l^0\right| H_{res}\left|\psi_k^0\right\rangle$. The value of E_p can be obtained from $\sum_k H_{lk}a_{kp} = E_p a_{lp}$, solving the associated matrix equation $[H][A] = [E][A]$, where $[A]$ is the matrix constructed from the coefficients a_{pk}.
Using then the orthonormalisation condition $\sum_{k=1}^{n} a_{kp}a_{kp'} = \delta_{pp'}$:

$$\sum_{l,k=1}^{n} a_{lp'}E_k^0\delta_{lk}a_{kp} + \sum_{l,k=1}^{n} a_{lp'}\left\langle\psi_l^0\right| H_{res}\left|\psi_k^0\right\rangle a_{pk} = E_p\delta_{pp'} \tag{2.26}$$

which is a matrix equation of the form $[A]^{-1}[H][A] = [E]$.

2.3 Solving the Schrödinger Problem

Considering the discussione above, in the Shell Model, the problem of obtaining the energies of the states and the corresponding occupation of the orbits reduces to a matrix eigenvalue problem.
One has to diagonalize the interaction matrix, and for this purpose the Lanczos method is commonly employed. Then one has to solve Eq. (2.26) in order to obtain the a_{pk} coefficients, and different codes have been written for this aim. In particular in this work the ANTOINE code [22] was used. In the current section the main ideas behind this code will be reported.

2.3.1 The Lanczos Method

The Lanczos method, proposed in Ref. [23], is used in order to diagonalize the hamiltonian matrix, so that the energies of the states can be obtained. This method takes as an input a pivot state, and with an iterative method is able to construct an eigenvector; this way giving an initial state of defined spin (J) and party (P), $\left|J^P\right\rangle$, one can get the energy of the lowest lying state with this spin and parity.
This algorithm is useful in Shell Model calculations since usually only few eigenstates of a given total angular momentum and isospin are needed. Moreover it also benefits from the fact that the matrices involved in these calculations are sparse: the non-zero matrix elements actually increase linearly with the dimension of the matrix, instead of quadratically [18].

Let's consider an hermitean matrix H. The algorithm starts with an orthonomalized pivot state $|1\rangle$, and one defines a new state as $|a_1\rangle = H|1\rangle$, which takes the form $|a_1\rangle = H_{11}|1\rangle + |2'\rangle$, where $H_{11} = \langle 1|H|1\rangle$ and $|2'\rangle$ is an orthogonal state, $\langle 1|2'\rangle = 0$.
The matrix element H_{11} can be obtained also from $H_{11} = \langle 1|a_1\rangle$ (since $|1\rangle$ is orthogonal to $|2'\rangle$), and then the second vector $|2'\rangle$ can be normalised, $|2\rangle = |2'\rangle / \sqrt{\langle 2'|2'\rangle}$.
From this, one can also obtain the matrix element H_{12} as $H_{12} = \langle 1|H|2\rangle = \sqrt{\langle 2'|2'\rangle}$.
This procedure can then be iterated n times, until the $|n\rangle$ vector is found, to which one can associate $|a_n\rangle = H|n\rangle$, that necessarily takes the form $|a_n\rangle = H_{nn-1}|n-1\rangle + H_{nn}|n\rangle + |(n+1)'\rangle$, and again the element H_{nn} can be obtained as $H_{nn} = \langle n|H|n\rangle = \langle n|a_n\rangle$. The "newest" state can be normalised

in the same fashion as before: $|n+1\rangle = |(n+1)'\rangle / \sqrt{\langle (n+1)'|(n+1)'\rangle}$.
In this way, one obtains the matrix:

$$H_n = \begin{pmatrix} H_{11} & H_{12} & \cdots & H_{1n} \\ H_{21} & H_{22} & \cdots & H_{2n} \\ \vdots & \ddots & \ddots & \vdots \\ H_{n1} & H_{n2} & \cdots & H_{nn} \end{pmatrix} \tag{2.27}$$

where $H_{ij} = \langle i| H |j\rangle$, and it is symmetric, so $H_{ij} = H_{ji}$. Notice that, since the matrix H is hermitean, all the elements H_{ij} with $|i-j| > 0$ are null, i.e. the matrix is tridiagonal, and can be now easily diagnalized.
The matrix is diagonalized at each step of the iteration, until the eigenvalues are convergent accordingly to some criterion. Typically it is chosen that the difference in energy of the states between two consecutive iterations, $\Delta E = E_{k+1} - E_k$, should smaller than a set value.

2.3.2 Shell Model Calculations

The Choice of Basis

The choice of the scheme basis is a matter of convenience. There are two main options:

- the *m-scheme*
- the *coupled J* or *JT scheme*

In the *m-scheme*, the basis is given by the set of the Slater determinants of the A particles distributed in k orbits, which can be represented as states $|nlmj\tau\rangle$, defined by their principal quantum number n, orbital and total angular momenta l and j, magnetic quantum number m and isospin τ. This is the harmonic oscillator basis.
The Slater determinants read:

$$\Phi_{a_1,\ldots,a_A}(1,\ldots,A) = \frac{1}{\sqrt{A!}} \det \begin{pmatrix} \phi_{a_1}(1) & \cdots & \phi_{a_A}(1) \\ \vdots & \ddots & \vdots \\ \phi_{a_1}(A) & \cdots & \phi_{a_A}(A) \end{pmatrix} = a^\dagger_{a_1} \cdots a^\dagger_{a_A} |0\rangle \tag{2.28}$$

The main reason why the m-scheme is appealing is due to the fact that in this basis the many-body matrix elements of H reduce to the two-particle matrix elements of H with a phase ([22]); however the flip of the coin is that in this basis only the projections J_z and T_z are good quantum numbers. This implies that all the possible (J,T) states are in this basis, so the dimension of the basis of Slater determinants will depend on the total degeneracy of the protons and neutrons in the valence spaces D_π and D_ν:

$$\#\text{ of SD} = \binom{D_\pi}{n_\pi} \times \binom{D_\nu}{n_\nu} \tag{2.29}$$

The J and JT coupled schemes split the full matrix, considered in the m-scheme, into much smaller boxes.
In the coupled schemes the basis is constructed in order to have a good total angular momentum (and total isospin) quantum number. For example in the J coupled scheme the states should be eigenstates of J^2; in order to have this, one defines a state for the i^{th} orbit having j_i angular momentum, n_i particles, v_i seniority and other additional quantum numbers x_i as $|\gamma_i\rangle = |(j_i)^{n_i} v_i x_i J_i\rangle$. Then for a system with A particles distributed in k orbits, the total state is found by applying successive angular momentum couplings [18]:

$$\left[[|\gamma_1\rangle\, |\gamma_2\rangle]^{J_2 T_2} \ldots |\gamma_k\rangle\right]^{J_k T_k} \tag{2.30}$$

The ANTOINE Code

The ANTOINE code [22] is an efficient implementation of the already discussed Lanczos algorithm, and is based on the ideas developed by the Glasgow group [24], working in the m-scheme basis and representing the Slater determinant basis as an integer to be stored in the calculator.
The input it takes is composed of:

- the valence space, i.e. the considered orbits that the valence nucleons can occupy, which depends on the nucleus considered and the relevant degrees of freedom;
- the number of valence nucleons of the nucleus, separated between protons and neutrons
- an effective interaction valid in that model space, e.g. USDa, USDb, zbm2, ...
- a set of initial states, J^p, each characterised by its total angular momentum J and its parity p

Let's proceed with the description of how the ANTOINE code works. First of all, each state $|nljm\tau\rangle$ gets an associated value, either 1 or 0, which indicates if that state is occupied or not, respectively.
The two-body operators of the interaction can be represented, in the context of the 2^{nd} quantization, in terms of annihilation and creation operators, $\hat{a}$ and $\hat{a}^\dagger$. The application of $\hat{a}^\dagger$ to a certain unoccupied state will switch the associated value from 0 to a 1, while the application of $\hat{a}$ will do the opposite.

The states can be written, in an m-scheme basis, separating the neutrons and protons Slater determinants: $|I\rangle = |i, \alpha\rangle$, where the uppercase latin characters, I, indicates the full space states, the lowercase latin ones, i, the protons subspace states and the greek ones, α, the neutron subspace states.
These states can be classified by the values of M, and $M = M_1 + M_2$, being M_1 the value of the M quantum number for one particle species and M_2 for the other. M will be the total projection of the angular momentum, associated to the full state, $|I\rangle$.
In this way, since M is fixed, only if $M = M_1 + M_2$ the Slater determinants of the two states will be associated; given a value of M, for each $|i\rangle$ (with associated M_1) one will have a minimum and maximum possible value of M_2 associated to the neutron state $|\alpha\rangle$.
It is then possible to build an array $R(i)$ that points to the $|I\rangle$ state: $I = R(i) + \alpha$. Here with i is denoted the position in the basis of the $|i\rangle$ states, α of the $|\alpha\rangle$ state and so on.
The values of $R(i)$, $R(j)$, α, β and the non-zero many-body matrix elements for proton-proton ($\langle i| H |j\rangle$) and neutron-neutron ($\langle \alpha| H |\beta\rangle$) interactions are pre-calculated, therefore with the Lanczos method a simple loop on α and i generates all the non-zero values $\langle I| H |J\rangle$.
For proton-neutron interactions the procedure is slightly less straightforward. Let's assume that $|I\rangle = |i, \alpha\rangle$, $|J\rangle = |j, \beta\rangle$, and that the $|i\rangle$ and $|j\rangle$ states are connected by a one-body operator, at the position s, $\hat{a}^\dagger_q \hat{a}_r$, with $q = |nljm\rangle$, $r = |n'l'j'm'\rangle$, and let's define $\Delta m = m' - m$. In the same fashion let's assume that $|\alpha\rangle$ and $|\beta\rangle$ are connected by a one-body operator, at the position μ.
Being the total M conserved, necessarily the values of m and m' for the neutrons will have difference $-\Delta m$, so that it cancels out with the difference in the quantum numbers for the protons.
One can then define a new array Q. In this way, $K = Q(s) + \mu$ will label the two-body matrix elements $V(K)$. As before $I = R(i) + \alpha$ and $J = R(j) + \beta$, are pre-calculated, so that the non-zero matrix elements $V(K) = \langle I| H |J\rangle = \langle J| H |I\rangle$ can be calculated and stored.

Effective Interactions

For the calculations, different effective interactions have been chosen: the USDa interaction [21], the zmb2 [25], the SDPF-U-MIX [26], the GXPF1a [27] and the LNPS [28]. The choice of the interaction clearly depends on the particular isotope that one wants to study, since its behaviour needs to be well reproduced in the valence space in which the effective interaction is defined. The most important aspect is that the valence space needs to be large enough in order to include all the relevant degrees of freedom, but not too large, in order to make the calculation feasible. What can happen, especially when dealing with neutron rich isotopes, is that the valence space considered by a specific interaction

becomes too limited.

The USDa interaction [21] has been used to perform calculations for nuclei with valence nucleons in the *sd* shell: the core is composed by the $0s_{1/2}$, $0p_{5/2}$ and $0p_{3/2}$ orbits (i.e. the *s* and *p* shells) for both protons and neutrons, so the core is the ^{16}O nucleus. The valence space is composed by $0d_{5/2}$, $1s_{1/2}$ and $0d_{3/2}$ for both protons and neutrons.
This interaction is obtained starting from the shell-model effective hamiltonian, specialised to the *sd* shell, written as (Ref. [21]):

$$H_{eff} = \sum_a \epsilon_a \hat{n}_a + \sum_{a \leq b, c \leq d} \sum_{JT} V_{JT}(ab;cd) \hat{T}_{JT}(ab;cd) \tag{2.31}$$

where ϵ_a is the usual one-body energy, $\hat{n}_a = \hat{a}_a^\dagger \hat{a}_a$ the number operator for the a orbit, $V_{JT}(ab;cd)$ is the two-body matrix element and the operator $\hat{T}$ can be expressed as :

$$\hat{T}_{JT}(ab;cd) = \sum_{MT_z} \hat{A}^\dagger_{JMTT_z}(ab) \hat{A}_{JMTT_z}(cd) \tag{2.32}$$

which represents the scalar two-body density operator for nucleon pairs.
In order to ease the notation the authors propose to write the effective hamiltonina as $H_{eff} = \sum_i x_i \hat{O}_i$, where x_i can stand for both ϵ_a and V_{JT}, and the operator O_i for both $\hat{n}$ and $\hat{T}$. In this way the hamiltonian can be fully determined by the vector $\vec{x}$, and it will have eigenstates $|\phi_k\rangle$ with corresponding eigenvalues λ_k:

$$\lambda_k = \langle \phi_k | H_{eff} | \phi_k \rangle = \sum_i x_i \langle \phi_k | \hat{O}_i | \phi_k \rangle \equiv \sum_i x_i \beta_i^k \tag{2.33}$$

where $\beta_i^k = \langle \phi_k | \hat{O}_i | \phi_k \rangle$.
In this way the derivation from experimental data of the matrix elements of the hamiltonian can be done by minimizing the χ^2:

$$\chi^2 = \sum_k \left(\frac{E^k_{exp} - \lambda_k}{\sigma^k_{exp}} \right)^2 \tag{2.34}$$

where E^k_{exp} and σ^k_{exp} are respectively the experimental energy and errors. The dataset used in Ref. [21] was composed of 608 states distributed in 77 *sd*-shell nuclei.

For the zmb2 interaction [25] the core is composed by the *s* shell, *p* shell and the $0d_{5/2}$ orbit for both protons and neutrons, so it is the ^{28}Si nucleus. The valence space is composed by the $1s_{1/2}$, $0d_{3/2}$, $0f_{7/2}$ and $1p_{3/2}$ orbits for both kinds of nucleons.
This interaction is based on three building blocks, which are:

- the USD interaction [29] for the nucleons in the *sd* shell
- a modified Kuo-Brown (KB) interaction [30] for the nucleons in the *fp* shell
- the G-matrix[2] of Lee, Kahanna and Scott [32] for cross-shell excitations.

The SDPF-U-MIX interaction [26] also has been employed for the Ca isotopes. This interaction has a core of ^{16}O and as valence space the *sd* and *pf* shells for both protons and neutrons, where the *pf* shell is composed of the orbits $0f_{7/2}$, $1p_{3/2}$, $0f_{3/2}$ and $1p_{1/2}$.
This interaction is an evolution of the SDPF-U interaction [26] based on the USD one for the *sd* shell, a variant of the KB one for the *pf* shell.
In the SDPF-U-MIX interaction the off-diagonal $sd - pf$ elements have been added, as well as a re-tuning of the interaction matrix has been performed, so that the shell gap between the *sd* and *pf* shells is in accordance with the experimental data.

[2]For the G-matrix method see Ref. [31]

The GXPF1a [27] is another example of interaction with fitted matrix elements, as the USDa interaction. In this case the inert core is the ^{40}Ca nucleus, and the valence space is composed of the pf shell for both protons and neutrons, so it is suited for nuclei with $20 < N, Z \leq 40$. It has been employed for the $^{50-59}$Mn and $^{54-64}$Ni isotopes.

The LNPS [28] interaction has been employed for the $^{60-65}$Mn and $^{65-70}$Ni isotopes. For this interaction the core is ^{48}Ca, while the valence space considered is the pf shell for protons and for neutrons the orbits $0f_{5/2}$, $1p_{3/2}$, $1p_{1/2}$, $0g_{9/2}$ and $1d_{5/2}$.
Also in this case the interaction has been built by considering different blocks, such as a variant of the KB interaction for the pf shell nucleons, the renormalized G-matrix presented in Ref. [31] for the neutron orbits $1p_{3/2}$, $1p_{1/2}$, $0f_{5/2}$ and $0g_{9/2}$ and finally the G-matrix based on Ref. [32] for the matrix elements involving the neutron $1d_{5/2}$ orbit. As for the other cases the final tuning of the matrix elements has been performed considering experimental constraints, such as the proton gap at $Z = 28$ and the neutron $N = 50$ gap.

The results coming from the ANTOINE code Shell Model calculations will be reported in Appendix A. In particular the occupation numbers for the ground states will be presented, as well as a selection of energy levels. This is done to provide a comparison with experimental data, in order to have an indicator of the goodness of the interaction.

Chapter 3

Nuclear Radii Theory

In this chapter the problem of a theoretical definition and formula for the nuclear radii is tackled, from both a macroscopic and a microscopic approach. As it will be here explained, one can build the formula for the nuclear radius starting from global properties of the nuclear system, devising a macroscopic phenomenological formula for the radius.
Another way to look at the same problem is to start from a harmonic oscillator potential, which is only an approximation for the far more complex real nuclear potential. The main problem in this microscopic formulation is to account for the needed corrections.

3.1 Macroscopic Approach

In the Ref. [12] Duflo and Zuker proposed a *phenomenological formula* for the proton and neutron radii of nuclei, in a macroscopic framework.
Their work was based on the isospin conservation assumption, and the fact that the proton radii can be written in the form of a Coulomb energy, so that through the same arguments that lead to the Isobaric Multiplet Mass Equation [33] (IMME) one can write:

$$\langle r_\pi^2 \rangle = \alpha(A,T) + \beta(A,T)T_z + \gamma(A,T)T_z^2 \tag{3.1}$$

where A is the mass number of the nucleus, T is the isospin and T_z its projection.

3.1.1 Isobaric Multiplet Mass Equation

The IMME can be derived assuming a macroscopic approach, treating the total hamiltonian as resultant of the effects of a charge invariant (CI) and a charge violating (CV) part, $H = H_{CI} + H_{CV}$. In this case, employing an isospin representation of the states, $|\alpha, T, T_z\rangle$ is an eigenstate of H_{CI}, of energy $E_{\alpha,T}$, while the contribution of the charge violating part can be further split into three separate contributions, considering nucleon-nucleon forces only:

$$H_{CV} = \sum_{k=0}^{2} H_{CV}^{(k)} \tag{3.2}$$

with $H_{CV}^{(0)} = (V_{pp} + V_{nn} + V_{pn})/3$ the isoscalar term, $H_{CV}^{(1)} = V_{pp} - V_{nn}$ the isovector term and $H_{CV}^{(2)} = V_{pp} + V_{nn} - V_{pn}$ the isotensor term, having identified V_{nn} as the potential between two neutrons, V_{pp} between two protons and V_{pn} between a neutron and a proton.
At this point one can calculate the binding energy $BE(\alpha, T, T_z) = \langle \alpha T T_z | H | \alpha T T_z \rangle$, however the charge invariant part will produce $E_{\alpha T}$, independently of the projection of the isospin, while for the

charge violating part the Wigner-Eckart theorem can be used in order to work with the reduced matrix elements only, giving:

$$\Delta BE(\alpha,T,T_z) = \frac{1}{\sqrt{2T+1}}M^{(0)} + \frac{T_z}{\sqrt{T(2T+1)(T+1)}}M^{(1)} + \\ + \frac{3T_z^2 - T(T+1)}{\sqrt{(2T-1)T(2T+1)(T+1)(2T+3)}}M^{(3)} \tag{3.3}$$

where Δ denotes that we are only considering the CV part and $M^{(k)} = \langle \alpha T | \, | H^{(k)}_{CV} | \, | \alpha T \rangle$ are the reduced matrix elements.
At this point the relation between the binding energy and the isospin projection can be made schematic:

$$BE(\alpha,T,T_z) = a(\alpha,T) + b(\alpha,T)T_z + c(\alpha,T)T_z^2 \tag{3.4}$$

which is the usual formulation of the isobaric multiplet mass equation.
One simplified example is the Coulomb energy, which can be written in terms of T_z:

$$E_c = \frac{3}{5R_c}e^2Z(Z-1) = \frac{3e^2}{5r_0A^{1/3}}\left[\frac{A(A-2)}{4} + (1-A)T_z + T_z^2\right] \tag{3.5}$$

having considered the rough approximation of a spherically symmetric nucleus of radius $R_c = r_0A^{1/3}$, and having exploited $T_z = N - Z$, $A = N + Z$.

3.1.2 Duflo-Zuker Phenomenological Formula

The link to the proton radii is given by [12]:

$$r_\pi^2 = \frac{1}{A^2}\left[\sum_{i<j}(1/2 - t_z^i)(1/2 - t_z^j)r_{ij}^2\right] \tag{3.6}$$

where r_{ij} is the distance between the i^{th} and j^{th} nucleons and t_z^i is the isospin of the i^{th} nucleon. This expression takes on a form similar to the Coulomb energy, if one exchanges r_{ij}^2 with r_{ij}^{-1}, thus one can make the same reasoning which brings to Eq. (3.1).

In particular Duflo and Zuker proposed in [12], specializing to mirror nuclei with $T_z = 2t = N - Z$, the formula:

$$\rho_\pi = A^{1/3}\left(\rho_0 - \frac{\zeta}{2}\frac{t}{A^\sigma} - \frac{v}{2}\frac{t^2}{A^2}\right)e^{g/A} \tag{3.7}$$

where $A^{1/3}$ is the general asymptotic behaviour for self-bound systems ($r \sim \rho_0 A^{1/3}$), $e^{g/A}$ is a correction made to account for the experimental fact that we observe larger radii for small A.
The ζ term measures the difference in radii between the fluids (the neutrons and the protons, i.e. the neutron skin if $\zeta > 0$) and v is the measure of the overall dilatation or contraction.
In particular it is possible to also calculate the proton radius by flipping the sign of t in Eq. (3.7).
By taking the difference between the neutron and the proton radii, it is possible to estimate the neutron skin:

$$\Delta r_{\nu\pi} = \frac{\zeta t}{A^{\sigma-1/3}}e^{g/A} \tag{3.8}$$

Finally, it is possible to interpret the exponent σ; there are two interesting cases:

- $\sigma = 1 \Rightarrow$ "volume skin", which would be what one would expect if there was strong attraction between particles of the same fluid (i.e. if $\nu - \nu$ and $\pi - \pi$ interactions were the strongest)
- $\sigma = 4/3 \Rightarrow$ "surface skin", which is the proposed one since $\nu - \pi$ interactions are the strongest (so the interaction between particles belonging to different fluids)

Starting from the experimental data sets available at the time of the publication of Ref. [12], the authors fitted the data, finding that ρ_0 and g had consistent values for different (v, ζ) couples, and to discriminate the optimal choice of (v, ζ) they resorted to the Coulomb displacement energies, $CDE = BE(Z_>, N_<) - BE(Z_<, N_>)$.

Note that the results found in Ref. [12] are only valid as long as the isospin is a conserved quantity, which was one of the assumptions made. In this macroscopic formula there is no mention of the underlying shell structure of the nucleus: a correction is needed in order to account for the shell effects.

The Extruder-Intruder Space

An important concept, needed in order to introduce the correction for shell effects for the phenomenological Duflo-Zuker formula for the nuclear proton and neutron radii is the so called extruder-intruder (EI) shell structure.
These shells are constructed starting from the harmonic oscillator levels, plus the spin-orbit interaction which splits them into orbits. As already stated, the energy of those orbits depends on their total angular momentum.

The extruder-intruder main shells are constructed starting from the p harmonic shell. From this shell, the highest-angular momentum one (i.e. the lowest-energy orbit) is shifted towards the $p-1$ harmonic oscillator shell. This will be called the "extruder" orbit. Then the lowest-angular momentum one (i.e. the highest energy orbit) is shifted towards the $p+1$ harmonic oscillator shell. This will then be called the "intruder" orbit.
One can graphically appreciate the construction of the four lowest-lying EI shells in Fig. 3.1.

The Phenomenological Duflo-Zuker Formula

Following Ref. [12], in order to account for shell-corrections Duflo and Zuker introduced a new term, $\mathcal{D} = \lambda S_\pi S_\nu + \mu Q_\pi Q_\nu$, which is a functional of the occupancy numbers in the EI (extrunder-intruder) space, where:

$$S_\pi = \frac{z(D_\pi - z)}{D_\pi^2}, \quad Q_\pi = \frac{z(D_{r\pi} - z)}{D_\pi^2}$$

where z is the number of valence protons in the EI shells, $D_\pi = (p_\pi+1)(p_\pi+2)+2$ and $D_{r\pi} = p_\pi(p_\pi+1)$ are the degeneracy of intruder and non-intruder orbits respectively. The expression for S_ν and Q_ν are the same of S_π and Q_π, exchanging only $z \leftrightarrow n$ and $\pi \leftrightarrow \nu$.
The λ term refers to spherical nuclei, while the μ term to deformed ones; the $\mathcal{D}$ term is referred to as the Duflo term or Duflo correction.
In this way, the shell-corrected radii result to be $\rho_\pi^{sc} = \rho_\pi + \mathcal{D}$. Notice that the shell correction term $\mathcal{D}$ is constructed in a way such that it vanishes at the EI closures, since $z, n = 0$.

Considering only the corrections for spherical nuclei one obtains [14]:

$$\rho_\pi^c = \rho_\pi^n + \lambda \left(\frac{n(D_\nu - n)}{D_\nu^2} \times \frac{z(D_\pi - z)}{D_\pi^2} \right) A^{-1/3} \rightarrow \text{correlated radius} \tag{3.9}$$

$$\rho_\pi^n = A^{1/3} \left(\rho_0 - \frac{\zeta}{2} \frac{t_z}{A^{4/3}} - \frac{v}{2} \left(\frac{t_z}{A} \right)^2 \right) e^{g/A} \rightarrow \text{naive radius}$$

where $t_z = N - Z$, $n[z]$ is the number of valence neutrons between the extruder-intruder magic numbers and $D_\nu[D_\pi]$ are the corresponding degeneracies.
In particular, we can define the neutron skin thickness as $\Delta r_{\nu\pi} = \rho_\nu^{n,c} - \rho_\pi^{n,c} = \frac{\zeta}{At} e^{g/A}$; notice that this is the only term that depends on the sign of t_z, meaning that if we were to consider two mirror nuclei (i.e. nuclei with the number of neutrons N and number of protons Z exchanged) this is the only term which can account for a difference in their radii.

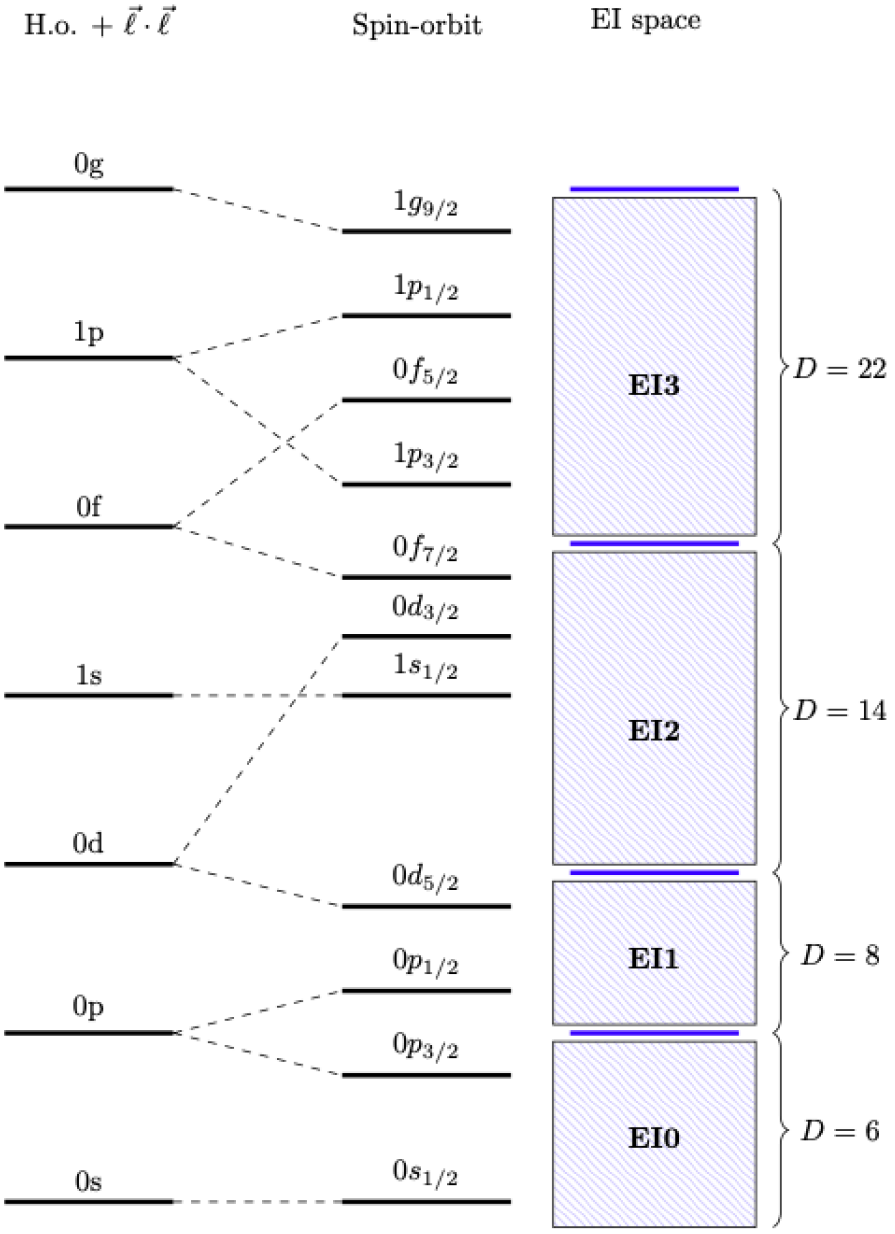

Figure 3.1: Graphic depiction of the construction of the extruder-intruder (EI) space shells, which are found inside the shaded blue areas, starting from the harmonic oscillator shells. The first four extruder-intruder shells are here called EI0, EI1, EI2 and EI3. D is the degeneracy of these shells.

3.2 Harmonic Oscillator Radii

In the previous part of this chapter the calculation of the nuclear radius by means of a macroscopic formula has been described. In order to introduce now a microscopic formula, first of all it is easier to consider the calculation of the radius in the approximation of an harmonic oscillator potential, and afterwords the corrections due to shell effects will be added.

3.2.1 The 3D Harmonic Oscillator Radius

Let's consider a $3D$ isotropic harmonic oscillator hamiltoninan:

$$H = \frac{\vec{p}^2}{2m} + \frac{m}{2}\omega^2\vec{r}^2 \tag{3.10}$$

where m is the mass, ω the oscillation frequency and $\vec{p} = (p_x, p_y, p_z)$ and $\vec{r} = (r_x, r_y, r_z)$ in a cartesian coordinate system.

Following the usual first quantization, the momentum and position of the particle are promoted to operators,

$$\vec{p} \to \hat{\vec{p}}, \quad \vec{x} \to \hat{\vec{x}}$$

and ladder operators $\hat{a}_i$ and $\hat{a}_i^\dagger$ (with $i = x, y, z$) are introduced, which are related to the position and momentum operator as:

$$\begin{cases} \hat{a}_i = \sqrt{\frac{m\omega}{2\hbar}} \left(\hat{r}_i + \frac{i}{m\omega}\hat{p}_i\right) \\ \hat{a}_i^\dagger = \sqrt{\frac{m\omega}{2\hbar}} \left(\hat{r}_i - \frac{i}{m\omega}\hat{p}_i\right) \end{cases} \iff \begin{cases} \hat{r}_i = \sqrt{\frac{\hbar}{2m\omega}}(\hat{a}_i^\dagger + \hat{a}_i) \\ \hat{p}_i = i\sqrt{\frac{\hbar m\omega}{2}}(\hat{a}_i^\dagger - \hat{a}_i) \end{cases} \tag{3.11}$$

They follow the commutation relations:

$$[\hat{a}_i, \hat{a}_j^\dagger] = \delta_{ij}, \quad [\hat{a}_i, \hat{a}_j] = 0 = [\hat{a}_i^\dagger, \hat{a}_j^\dagger], \quad \text{with } i = x, y, z \tag{3.12}$$

Let's then introduce an orthonormal basis of eigenstates of the energy, $\{|\vec{n}\rangle_\alpha = |n_x, n_y, n_z\rangle_\alpha\}_{\alpha=0,1,\ldots}$ (Fock states). The application of the $\hat{a}$ and $\hat{a}^\dagger$ ladder operators to an energy eigenstate gives:

$$\hat{a}_i |\vec{n}\rangle = \sqrt{n_i}\, |\vec{n} - 1\rangle\,, \quad \hat{a}_i |\vec{n}\rangle = \sqrt{n_i + 1}\, |\vec{n} + 1\rangle \tag{3.13}$$

It is then possible to define the number operator as $\hat{N}_i = \hat{a}_i^\dagger \hat{a}_i$, which is such that $\hat{N}_i |\vec{n}\rangle = n_i |\vec{n}\rangle$ due to the relations listed above.
Now it is possible to calculate the expectation value of the radial dimension for a given eigenstate of the energy.
For a given Fock state $|\vec{n}\rangle$:

$$\langle\vec{n}| r^2 |\vec{n}\rangle = \langle\vec{n}| (r_x^2 + r_y^2 + r_z^2) |\vec{n}\rangle \tag{3.14}$$

and considering, e.g., only the contribution along x, using the relation $a_x^\dagger a_x |n_x\rangle = n_x |n_x\rangle$ as well as the commutation relation $[\hat{a}_x, \hat{a}_x^\dagger] = 1$, one obtains:

$$\begin{aligned} \langle n_x| r_x^2 |n_x\rangle = \frac{\hbar}{2m\omega} \langle n_x| \left[(a_x^\dagger)^2 + a_x^2 + a_x a_x^\dagger + a_x^\dagger a_x\right] |n_x\rangle = \frac{\hbar}{2m\omega} \langle n_x| \left[2a_x^\dagger a_x + 1\right] |n_x\rangle = \\ = \frac{\hbar}{m\omega}(n_x + 1/2) \end{aligned} \tag{3.15}$$

Thus, summing over the three spatial directions:

$$\langle\vec{n}| r^2 |\vec{n}\rangle = \frac{\hbar}{m\omega}(n_x + n_y + n_z + 3/2) = \frac{\hbar}{m\omega}(p + 3/2) \tag{3.16}$$

where the principal quantum number $p = n_x + n_y + n_z$ has been made explicit.

Spherical Coordinates

Since the $3D$ harmonic oscillator has spherical symmetry, one can pass to spherical coordinates and construct eigenstates with quantum numbers n, ℓ and m; in this basis the principal quantum number is $p = 2n + \ell$, $p \geq 0$, $0 \leq \ell \leq p$.
The same relation for the mean square radius holds, however now the principal quantum number can also be written in term of the spherical quantum numbers.

3.2.2 Harmonic Oscillator Radius for Nuclear Orbits

Starting from the $3D$ harmonic oscillator result Eq. (3.16), one can generalize then the formula for the radius of the nuclear system by summing over all the harmonic oscillators orbits [14]:

$$\langle r_{ho}^2 \rangle = \sum_i \langle i| r^2 |i\rangle = \frac{41.47}{\hbar\omega[\text{MeV}]} \sum_i \frac{m_i}{A}(p_i + 3/2)\ \text{fm}^2 \tag{3.17}$$

where the possible orbits $|i\rangle = |n_i \ell_i j_i\rangle$ are specified by the principal quantum number $p_i = 2(n_i - 1) + \ell_i$, and $m_i = z_i + n_i$ is the total occupation number of the orbits, which tells us how many particles are, on average, present in that orbit (z_i is the proton occupation number and n_i is the neutron one). Notice that also the inert core orbits are considered, and these are always fully occupied.
In order to retrieve the second equality, it is useful to introduce the size parameter:

$$b^2 = \frac{\hbar}{m\omega} = \frac{\hbar^2 c^2}{mc^2} \frac{1}{\hbar\omega} = \frac{41.47}{\hbar\omega} \text{ MeV fm}^2 \tag{3.18}$$

where $mc^2 = m_{\text{nucleon}} c^2 \simeq 938$ MeV (since the case of interest in this work is the nuclear system), and the relation $\hbar c = 197$ MeV fm was used. In this way, when expressing the $\hbar\omega$ parameter in MeV units, it is possible to obtain the mean square radius directly in fm^2 units.
From now on the parameter $\hbar\omega$ will be implicitly assumed to be expressed in MeV.

Eq. (3.16) only considers an harmonic potential, which is known to not be able to describe the nuclear system. This result will not be used as it is in order to perform calculations: starting from Eq. (3.16) one can provide corrections in order to make realistic calculations.

3.3 Microscopic Formulation of Mean Square Radii

In this section the various methods that have been identified to calculate the nuclear charge radii, in particular accounting for corrections due to the correlations, will be introduced and discussed. They will then be applied to the calculations of the isotope shifts.
Starting from the expression for the mean square radius given in Eq. (3.17), Bonnard and Zuker in Ref. [14] proposed to link the microscopic formulation to the phenomenological Duflo-Zuker formula via the relation[1]:

$$\langle r^2_{ho} \rangle = \frac{41.47}{\hbar\omega} \sum_i \frac{m_i}{A} (p_i + 3/2) \sim (\rho^n_\pi)^2 \tag{3.19}$$

where the mean square radius is expressed in fm^2, and ρ^n_π refers to the "naive" proton radius as calculated in Eq. (3.7).
Thus, the authors linked the naive form of the phenomenological formula to the mean square radius in a microscopic framework obtained by considering an harmonic oscillator potential.

Since the relation in Eq. (3.19) holds for the "naive" radius, one should account for corrections to the microscopic formula in order to integrate the contributions coming from the addition of the Duflo term, present in Eq. (3.9). The Duflo term, as already mentioned, accounts for shell effects.
The corrections will be twofold: firstly the presence of the so-called δ_i terms, needed to account for the presence of "halo" orbits, will be discussed. Secondly, a correction concerning the harmonic oscillator energy parameter $\hbar\omega$ will be introduced. These corrections will then be applied to Eq. (3.19), producing an expression for the corrected proton radius which will then be related to the "correlated" form of the Duflo-Zuker formula, Eq. (3.9).

3.3.1 The δ Correction

The first correction that is going to be discussed is the δ correction term, related to "halo" orbits. In the study done in Ref. [13], the Bonnard, Lenzi and Zuker studied mirror nuclei, i.e. nuclei with interchanged N, Z, with $T_z = 1/2$. The authors considered nuclei with mirror nuclei with $A = 15$, focusing on the first $1/2^-$ and $3/2^-$ states, $A = 17$, focusing on the $5/2^+$ and $1/2^+$ states, $A = 39$, focusing on the $3/2^+$ and $1/2^+$ states, and $A = 41$ focusing on the $7/2^-$, $3/2^-$, $1/2^-$ and the first two $5/2^-$ states. The authors investigated the mechanism behind the observed mirror energy differences

[1] In this work the notation used for the square radii is $\langle r^2 \rangle$ for the ones calculated via a microscopic formula, and ρ^2 for the ones coming from the phenomenological approach. In a microscopic approach one always deals with the expectation value of the radius operator.

(MED) and mirror displacement energies (MDE). The former refers to the differences in the spectra of two mirror nuclei, the latter to the differences between the ground states.
Exploiting the knowledge of the Duflo-Zuker equation Eq. (3.9), the authors have linked the MED to the enlargement of an orbit; the idea behind this consists in adjusting the ζ parameter, which is related to the neutron halo dimension in order to solve the so called Nolen-Schiffer anomaly [34]. This anomaly is the discrepancy between the prediction and the experimental results of the differences in binding energies between the two mirror nuclei.
The results of the study [13] predict an enlargement of the $1s_{1/2}$, $1p_{3/2}$ and $1p_{5/2}$ orbits.
In particular, from the mirror nuclei with $A = 17$ the prediction is that the $1s_{1/2}$ orbit is about 1.2 fm larger than the $0d_{5/2}$, while from the mirror nuclei with $A = 41$ that the p orbits in the pf shell are larger than the f orbits by about 0.7 fm. Thus, the authors propose to attribute the experimental isotope shifts to the "halo" nature of these orbits. Moreover the enlargement was found to not be constant: considering the $A = 39$ mirror nuclei the s orbit is still larger than the d ones, but not at the same extent.

In a subsequent study, Ref. [14], Bonnard and Zuker proposed a microscopic parametrization of the mean square proton radii accounting for the results presented in Ref. [13].
The authors proposed to add a correction to Eq. (3.19) would account for the "halo" orbits, as well as for the Duflo correction λ present in the phenomenological formula Eq. (3.9):

$$\langle r_\pi^2 \rangle = \frac{41.47}{\hbar\omega} \sum_i \frac{m_i}{A}(p_i + 3/2 + \delta_i) \sim (\rho_\pi^c)^2 \tag{3.20}$$

where ρ_π^c refers to the "correlated" proton radius of Eq. (3.9), and δ_i are the corrections mentioned above.
These δ_i terms should be referred to the "halo" orbits, and should act as a correction of the harmonic oscillator result.
In this study, Bonnard and Zuker focused on two dataset composed of 21 and 24 *sd* shell nuclei with $2T_z = N - Z = 0, 1, 2$ respectively, and fitted them with Eq. (3.20), adopting a step-function form for the δ correction discontinuous at the EI closure $N, Z = 14$:

$$\delta_s = \begin{cases} \delta_s^> & \text{if } N, Z < 14 \\ \delta_s^< & \text{if } N, Z > 14 \end{cases}$$

The calculation of the occupation numbers m_i have been performed via two different interactions: the USDa [21] and the monopole corrected interaction [35] (MCI).

Then the authors have estimated the radius of the i^{th} orbit as:

$$\rho_i^2 = \langle im_{j_i} | \, r^2 \, | im_{j_i} \rangle = \frac{41.47}{\hbar\omega}(p_i + 3/2 + \delta_i) \tag{3.21}$$

and their results have been reported in Fig. 3.2.

In the paper Ref. [14] the authors tackled systematically the *sd* shell. However also the other shells will contain "halo" orbits, as proposed in Ref. [13]. In particular a recent study [36] showed experimentally that the difference between the radius of the p and f shells of ^{52}Ca is indeed about 0.61 fm, compatible with what predicted in Ref. [13] for the p "halo" orbit. So in the same fashion as the *sd* shell, one can also introduce:

$$\delta_p = \begin{cases} \delta_p^> & \text{if } N, Z < 28 \\ \delta_p^< & \text{if } N, Z > 28 \end{cases}$$

where this time the correction refers to the $1p_{3/2}$ and $1p_{1/2}$ "halo" orbits of the pf shell. The step-function form of the δ_p correction is now discontinuous at $N, Z = 28$, since this represents the closure of the next EI shell after $N, Z = 14$.

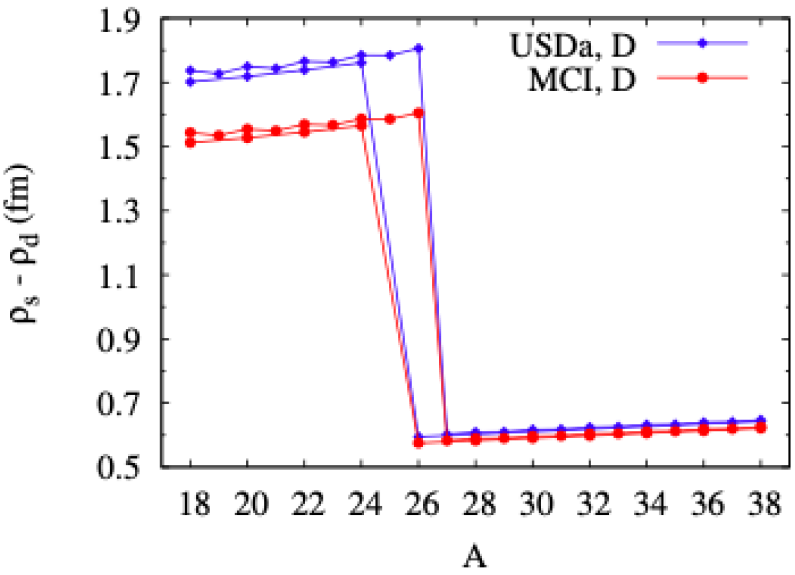

Figure 3.2: Difference between the s and d orbits radii as a function of A. In this figure, taken from Ref. [14], the estimated difference between the radius of the s orbit (ρ_s) and the one of the d orbit (ρ_d), obtained using Eq. (3.21), is displayed. In blue are reported the results obtained using $\delta = 4.90 - 1.40$, while in red using $\delta = 5.50 - 1.35$. The values of $\delta_<$ and $\delta_>$ are obtained using two different interactions (USDa and MCI).

A consideration which may arise regards the fact that the the proton radius depends only on m_i and does not have any term which depends on the protons and neutrons occupation numbers separately. As shown in Ref. [12], considering Eq. (3.9), it is always possible, for different values of ζ, to reproduce the same root-mean-square deviation by changing the value of v, so that the isovector term does not actually influence the radius. Another consideration is the fact that the Duflo term λ is itself isoscalar, thus an isospin representation is actually justified.
The $\hbar\omega$ parameter, i.e. the energy of the harmonic oscillator, is crucial for Shell-Model calculations, since it scales the 2-body matrix elements, for given a reference value $\hbar\omega_r$ of the harmonic oscillator energy, as $V(\hbar\omega) = V(\hbar\omega_r)\frac{\hbar\omega}{\hbar\omega_r}$. This will be later discussed in more detail, as it will play an important role in the calculations.

The Charge Radius

The radius calculated in Eq. (3.20) or Eq. (3.9) is called "point proton radius". The point proton radius can be related to the experimentally observed "charge radius" via Ref. [37]:

$$\langle R_c^2 \rangle = \langle r_\pi^2 \rangle + \langle r_p^2 \rangle + \frac{N}{Z}\langle r_n^2 \rangle + \frac{3\hbar^2}{4m_p^2c^2} \tag{3.22}$$

where $\langle r_p^2 \rangle = 0.77$ fm^2 is the mean square charge radius of the proton [38] and $\langle r_n^2 \rangle = -0.1149$ fm^2 is the mean square charge radius of the neutron [5]. Finally the term $3\hbar^2/4m_p^2c^2 = 0.033$ fm^2, where m_P is the proton mass, is the Darwin-Foldy correction, which takes into account the "zitterbewegung" of the proton due to virtual particle-antiparticle pairs.
This is the charge radius that can then be compared with the experimental data.
Notice that in this work the focus is actually on the isotope shifts, i.e. the differences $\delta\langle R_c^2 \rangle^{AA'} = \langle R_c^2 \rangle^A - \langle R_c^2 \rangle^{A'}$ between two isotopes of mass numbers A and A'; the constant terms will cancel out, however the correction related to the point neutron radius will remain since it is proportional to N/Z, which indeed changes along the isotopic chain.

3.3.2 The Harmonic Oscillator Parameter

Now the second correction that can be employed will be tackled, concerning the energy parameter $\hbar\omega$ of the harmonic oscillator.

The usual Shell Model assumption for the oscillator energy is:

$$\hbar\omega = 45A^{-1/3} - 25A^{-2/3} \text{ MeV} \tag{3.23}$$

being A the mass number of the nucleus. This is the classical assumption [4] referred to as the Bohr-Mottelson $\hbar\omega$ parameter. Notice that it is the same for neutrons and protons.
The main problem with the Bohr-Mottelson form of the parameter is that it is smooth and monotonically decreasing for $A > 2$, and being inversely proportional to the square radius its contribution makes the radius grow monotonically as well. This is not compatible with experimental observations of isotope shifts, and thus one may try to look into this parameter in order to provide corrections to the microscopic formula.

A possible procedure that can be used in order to modify the Bohr-Mottelson parameter is to use the correlated radius formula, given by Eq. (3.9), for protons and neutrons, which is a function of 5 parameters (ρ_0, ζ, v, g and λ) and find the best fit for the experimental data, thus obtaining the Duflo-Zuker (DZ) form of $\hbar\omega$.
Here one has to be careful in the interpretation of this fact. In particular a fit of (3.20) has been performed in order to retrieve the five parameters and finds the values of the radii and of the oscillator energies. In particular, the $\hbar\omega$ parameter is extracted by considering that each nucleon occupies the first lowest-lying available orbit, and then the relation:

$$\rho_\pi^2 = \frac{41.47}{\hbar\omega} \sum_i m_i(p_i + 3/2)/A$$

is inverted, where ρ_π is the value of radius coming from Eq. (3.9). In this case, the implication is that the Duflo correction is actually only modifying the value of $\hbar\omega_\pi$ (the correlated "DZ" parameter).

Another way to tackle this is to perform the five-parameter fit of Eq. (3.9), and setting $\lambda = 0$ afterwords: in this way one should obtain the "uncorrelated" $\hbar\omega_\pi(\lambda = 0)$, which should represent only a correction to the Bohr-Mottelson approximation.
Then one should be able to reproduce the result of the full fit by adding the δ_i terms to the correct the dimension of the halo orbits.

One can then compare the $\hbar\omega$ obtained by fitting a set of data with the Duflo-Zuker formulae Eq. (3.9) and Eq. (3.7); for example taking the Na isotopes with $A = 20 - 28$ the difference between the Duflo-Zuker and Bohr-Mottelson parameters is striking (see Fig. 3.3).

These considerations will be later applied in order to get a prescription which will account for both sources of corrections.

3.4 Microscopic Description

Following what was discussed previously in this chapter, the goal is now to devise a way to calculate and reproduce the experimental isotope shifts, reproducing as closely as possible the observed values and trend.

The starting point is the Duflo-Zuker phenomenological formula, given by Eq. (3.9) and Eq. (3.7). One can use the correlated form for the nuclear proton radius in order to perform a five-parameter fit of a set of experimental nuclear charge radii. Notice that this will not be done for each isotopic chain that will be considered, but only fitting a set of experimental data in order to preserve the "universality" of the formula: one set of the five values should be able to reproduce all the isotope shifts, and it should not change for different isotopic chains.
This procedure allows to extract the "correlated" $\hbar\omega_\pi$ parameter inverting the relation given by

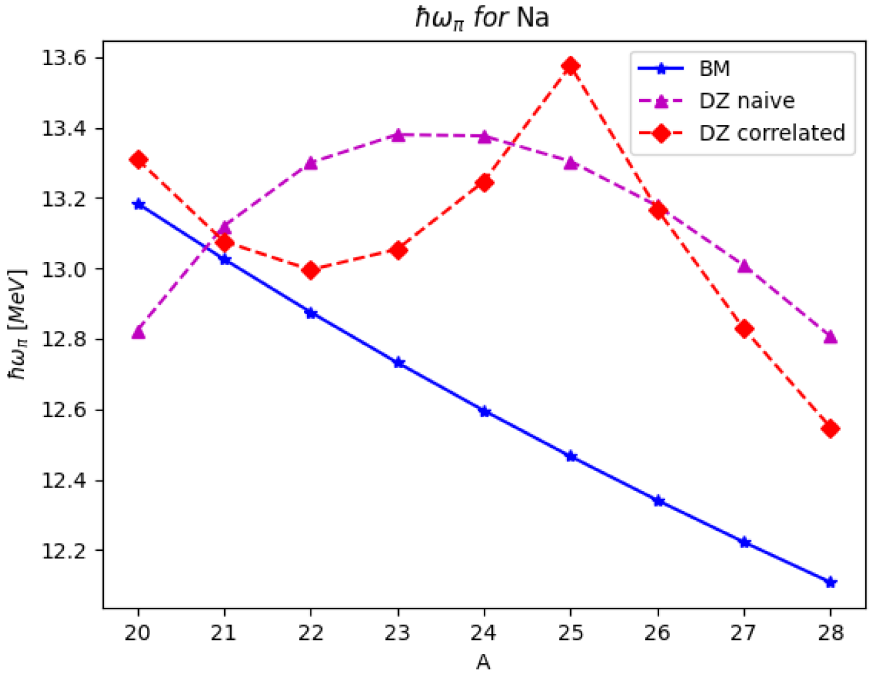

Figure 3.3: $\hbar\omega_\pi$ parameter as a function of the mass number A. In this figure the difference between the $\hbar\omega_\pi$ parameter of the Bohr-Mottelson (BM) form (blue stars), usually employed for shell model calculations, and the Duflo-Zuker (DZ) form is highlighted. The "DZ naive" curve (magenta triangles) refers to the result coming from the fit of Eq. (3.7), while the "DZ correlated" curve (red diamonds) comes from the fit of Eq. (3.9), which accounts for shell corrections. Notice that the BM form is the same for protons and neutrons, while the DZ form is specifically for the protons.

Eq. (3.20) by considering the approximation in which each nucleon occupies the lowest-lying free orbit, as already explained. The extracted $\hbar\omega_\pi$ parameter can in turn be used to calculate the proton radii directly via the harmonic oscillator formula, and one can think of this parameter to be the only responsible for the trend of the isotope shifts.
This procedure does not really help in understanding what drives the isotope shifts, however a possible explanation is, as already stated, the presence of the so-called "halo" orbits.

By taking the parameters coming from the fit of Eq. (3.9) and setting $\lambda = 0$ afterwords, the result should be the "uncorrelated" radius and $\hbar\omega_\pi$ parameter. In this sense the Duflo-Zuker formula tells us how the oscillator parameters deviates from the Bohr-Mottelson one, just because of the form of the potential itself, and not because of correlations. The idea is thus to use the fitted "uncorrelated" energy parameter, $\hbar\omega_\pi(\lambda = 0)$, since the theoretical energy is limited by the current knowledge of the nuclear force itself. In this way, one should find a phenomenological form of the $\hbar\omega$ parameter, which is more accurate with respect to the Bohr-Mottelson one.

Notice that this is not going to solve all the discrepancies between the h.o. result and the experimental isotope shifts, since the Duflo term has been left out: the correlations will then be tackled using the already discussed δ_i corrections for the "halo" orbits.

In order to calculate the proton radii, three different methods have been identified and they will be discussed in the following.

3.4.1 The "BZ10" Method

The first method comes from equation (10) of Ref. [14] by Bonnard and Zuker (and it will thus be referrer to as "BZ10" method). Here the proposed form for the calculation of the proton radii is:

$$\langle r_\pi^2 \rangle = [\rho_\pi(\lambda = 0)]^2 + \frac{41.47}{\hbar\omega_\pi(\lambda = 0)} \sum_i \frac{m_i}{A} \delta_i \tag{3.24}$$

where $\rho_\pi(\lambda = 0)$ and $\hbar\omega_\pi(\lambda = 0)$ are the important parameters coming from the "uncorrelated" fit, and in particular $\rho_\pi(\lambda = 0)$ represents the "uncorrelated" proton radius. In Eq. (3.24) the larger radius of the "halo" orbits is accounted for by the δ_i terms.

3.4.2 The "BZ3c" Method

A second method consists in proceeding directly from the formula proposed by Bonnard and Zuker in [14] for the "correlated" proton square radius:

$$\langle r_\pi^2 \rangle = \frac{41.47}{\hbar\omega_\pi(\lambda = 0)} \sum_i \frac{m_i}{A} (p_i + 3/2 + \delta_i) \tag{3.25}$$

This methods has been called "BZ3c" since it comes from equation (3) in Ref. [14] and the "c" stands for the correlated form of the proton radius.
Essentially, the difference between Eq. (3.24) and Eq. (3.25) lies in the fact that for the former $\rho_\pi(\lambda = 0)$ is taken directly from the "uncorrelated" Duflo-Zuker fit, while in the second is calculated using $\hbar\omega_\pi(\lambda = 0)$ (it is given by Eq. (3.25) taking $\delta_i = 0\ \forall i$). In this way, also the "uncorrelated" part accounts for the occupation numbers of the orbits m_i, while in the "BZ10" method comes directly from a macroscopic formula.

3.4.3 The "BLZ9" Method

A final alternative approach, proposed in equation (9) of Ref. [13] and thus referred to as "BLZ9", is:

$$\langle r_\pi^2 \rangle = \frac{41.47}{\hbar\omega_\pi(\lambda = 0)} \sum_i \frac{z_i}{Z} (p_i + 3/2 + \delta_i) \tag{3.26}$$

where z_i is the occupation number of the proton orbits only. Notice that in this case the $\hbar\omega_\pi(\lambda = 0)$ parameter extraction will be different from the previous two cases, since in this formula only the protons occupations are relevant, as explained in Section 3.3.2.

3.4.4 The Choice of the δ Correction

The δ_i terms need to account for the effects of the Duflo term of the phenomenological formula in the microscopic approach. As discussed, Bonnard and Zuker predict an abrupt change of the charge radii in correspondence of the extruder-intruder shell closure, i.e. at $N, Z = 14, 28$ in the cases relevant for this work.
As explained in Section 3.3.1, Bonnard and Zuker [14] performed a comprehensive study of *sd* shell nuclei, considering a set of 21 nuclei with $2T_z = 0, 1,\ 2$. Considering a step-function form for the δ_s correction:

$$\delta_{1s_{1/2}} = \begin{cases} \delta^< \text{ if } N, Z < 14 \\ \delta^> \text{ if } N, Z \geq 14 \end{cases}$$

the authors fitted this dataset with Eq. (3.24), using the occupation numbers coming from the USDa [21] interaction. The fitted values $\delta^< = 4.9$ and $\delta^> = 1.4$ described well the experimental data.
For the *pf* shell a hint of the value of $\delta_<$ for the *p* orbits can be found in the Ref. [13], where the

authors predicted a difference between the p and f orbits of about 0.7 fm. In a recent study [36] the authors experimentally measured the difference in radius of the p and f orbits for ^{52}Ca, finding a difference of 0.61(32) fm, compatible with what suggested by Bonnard, Lenzi and Zuker.
In this way, employing a step-function form also for the δ_p correction discontinuous at the $N, Z = 28$ EI closure one can estimate the corresponding value of the $\delta_p^>$ term via the difference:

$$\rho_{1p_{3/2}} - \rho_{0f_{7/2}} = 0.61 \text{ fm} = \sqrt{\frac{41.47}{\hbar\omega}(9/2 + \delta_p^>)} - \sqrt{\frac{41.47}{\hbar\omega}(9/2)} \tag{3.27}$$

since $p_{1p_{3/2}} = p_{0f_{7/2}} = 3$.
By taking the value of $\hbar\omega(\lambda = 0)$ from the fit for ^{52}Ca one finds that for $\delta = 1.5$ the difference of radii is indeed compatible with 0.61(32) fm, as it can be seen in Fig. 3.4.
Since ^{52}Ca has 32 neutrons, we expect this to be $\delta_p^>$, suitable when $N, Z \geq 28$, while for $N, Z < 28$ the value for $\delta_>^p$ has been assigned in order to reproduce a drop similarly to the one followed by δ_s (see figure Figs. 3.2 and 3.4):

$\delta_s^<$	$\delta_s^>$	$\delta_p^<$	$\delta_p^>$
4.9	1.4	4	1.5

Table 3.1: Summary of the values of δ chosen following the *sd* shell systematic study in Ref. [14] and the experimental result from Ref. [36].

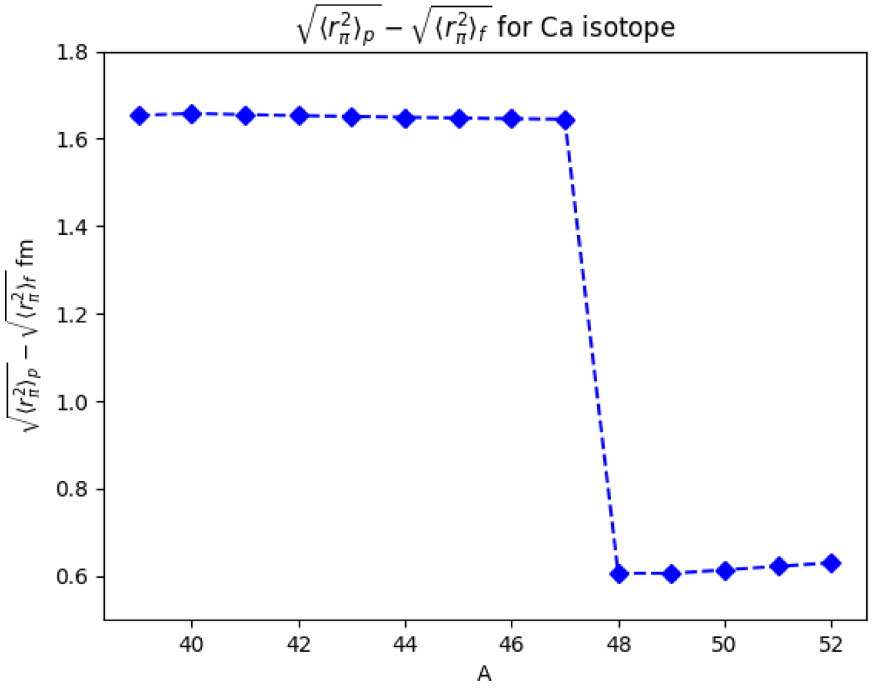

Figure 3.4: Difference between the p and f orbits radii as a function of A. In this figure the difference between the p and f orbits calculated for the $^{39-52}$Ca isotopes has been shown. Notice that this actually depends on the $\hbar\omega_\pi$ parameter: in this case it was chosen to use the "uncorrelated" energy parameter, as explained in Section 3.3.2 (i.e. the one referred to as $\hbar\omega_\pi(\lambda = 0)$).

Remember that what is calculated by the three methods or by the Duflo-Zuker formula is the proton radius of the nucleus, and in order to compare it with the experimental data a correction has to be made, given by Eq. (3.22).

Notice that the extrapolation of $\hbar\omega(\lambda = 0)$, provided that the fit is good enough, allows for a more accurate form of such parameter. Indeed, the smooth Bohr Mottelson form does not really work in reproducing the main features of the observed isotope shifts.

3.4.5 The Caurier Method

The chapter will be concluded by reporting a different method introduced by Caurier, Langanke, Martínez-Pinedo, Nowacki and Vogel in Ref. [25] used to calculate the isotope shifts for $^{40-48}$Ca. Calcium isotopes have $Z = 20$, and the explanation for the peculiar behaviour of the experimental isotope shifts reported in Fig. 3.5 has been attributed to cross-shell excitations of the protons, between the sd and pf shells.
An interaction has been proposed in Ref. [25], based on the work in Ref. [39]. In particular the model space has a ^{16}O core, and the valence space is composed by the $d_{3/2}$, $s_{1/2}$, $f_{7/2}$ and $p_{3/2}$ orbits for both protons and neutrons, in order to describe neutron rich calcium isotopes.
The mechanism driving the trend of the isotope shifts has been attributed to the excitations of the protons to the pf shell.
The differences in the square radii of the isotopes with respect to ^{40}Ca can then be estimated as:

$$\delta\langle r_\pi^2\rangle^{A,40} = \left(\frac{b_\pi^2}{Z}(z_{0f_{7/2}} + z_{1p_{3/2}})\right)^A - \left(\frac{b_\pi^2}{20}(z_{0f_{7/2}} + z_{1p_{3/2}})\right)^{A=40} \tag{3.28}$$

where z_i is the occupation of the proton i^{th} shell, b_π^2 is the oscillator parameter for the calcium isotopes considered.
In general, the size parameter b_π depends on the mass number A, however in Ref. [25] the authors opted for a constant $b_\pi = 1.974$ fm has been employed, arriving to the result shown in Fig. 4.8. The general trend of the isotope shifts is well represented, however the staggering features are less pronounced in the calculations with respect to the experimental data.

This method will be later discussed in Chapter 4, when considering the results for the calcium isotope shifts.

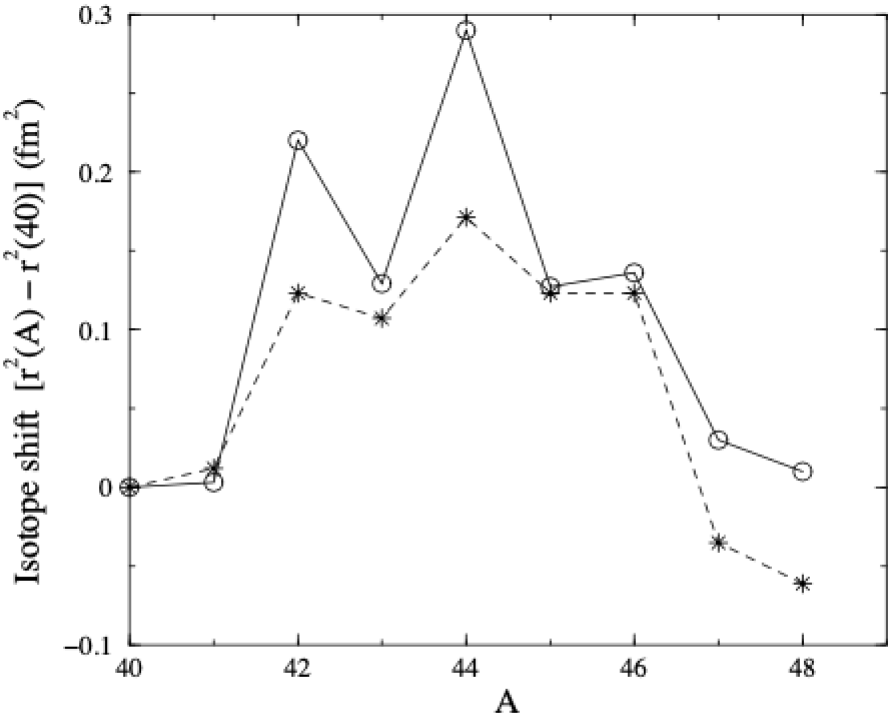

Figure 3.5: Isotopes shifts of calcium isotopes as a function of the mass number A. This figure, taken from Ref. [25], presents a comparison between the experimental data (hollow circles connected by a solid line) and their calculations (stars connected by a dashed line). For the details of the calculation see text.

Chapter 4

Systematic Study of Isotope Shifts

In this chapter the main methods used in this work in order to calculate the isotope shifts, both in a macroscopic and microscopic framework, are applied to the isotopic chains of Na, Mg, Ar, Ca, Mn and Ni are then the results reported and discussed.

4.1 Application of the Empirical Formula

In this section the empirical Duflo-Zuker formula will be applied, and the results will be analyzed.
It is important to remind that the fit of Eq. (3.9) involves 5 parameters, of which one can be roughly set by studying the neutron skin, i.e. $\zeta = 0.8$ fm; moreover, it has been shown that different values of this parameter ranging between $0.0 < \zeta < 1.2$ fm do not really change the quality of the fit [14].
The fitted function depends on the isospin of the nucleus and on the valence neutrons and protons between the E.I. orbits, as well as on the corresponding degeneracy of the orbits.
For consistency of notation's sake, one can distinguish three different fits:

- "DZ correlated fit", meaning the fit coming from the correlated Duflo-Zuker Eq. (3.9);
- "DZ naive fit", meaning the fit coming from the uncorrelated Duflo-Zuker formula Eq. (3.7).

The fit has been performed on a dataset, reported in Appendix B, which consisted of measured charge radii up to $Z = 30$. The results of the fitting procedure are shown in Table 4.1:

Fit	ρ_0 [fm]	g	λ [fm]	ν [fm]	ζ [fm]	rmsd [fm]
"DZ correlated"	0.944	0.985	5.561	0.368	0.8	0.0176
"DZ naive"	0.957	1.280	0	−1.139	2.039	0.0390

Table 4.1: Values obtained from fitting Eq. (3.9) ("DZ correlated") and Eq. (3.7) ("DZ naive") with the set of data reported in Appendix B, where the rmsd are the root-mean-square deviation.

The corresponding isotope shifts are then reported in Fig. 4.1, where both the "correlated" and "naive" fit results are shown, with the intent of understanding if they reproduce the experimental data. Moreover the necessity of the Duflo term should be clear from this comparison.

In order to quantify the goodness of the agreement between the results form of the Duflo-Zuker phenomenological formula better and the experimental data, one can compare the mean differences between the observed values O_i and the calculated ones E_i:

$$\text{rmsd} = \sqrt{\frac{\sum_{i=1}^{n}(O_i - E_i)^2}{n}} \tag{4.1}$$

Overall, the "DZ correlated" fit works well for the isotopic chains chosen in this work, however it is clear that all the staggering features, which are caused by the underlying shell structure, are lost in

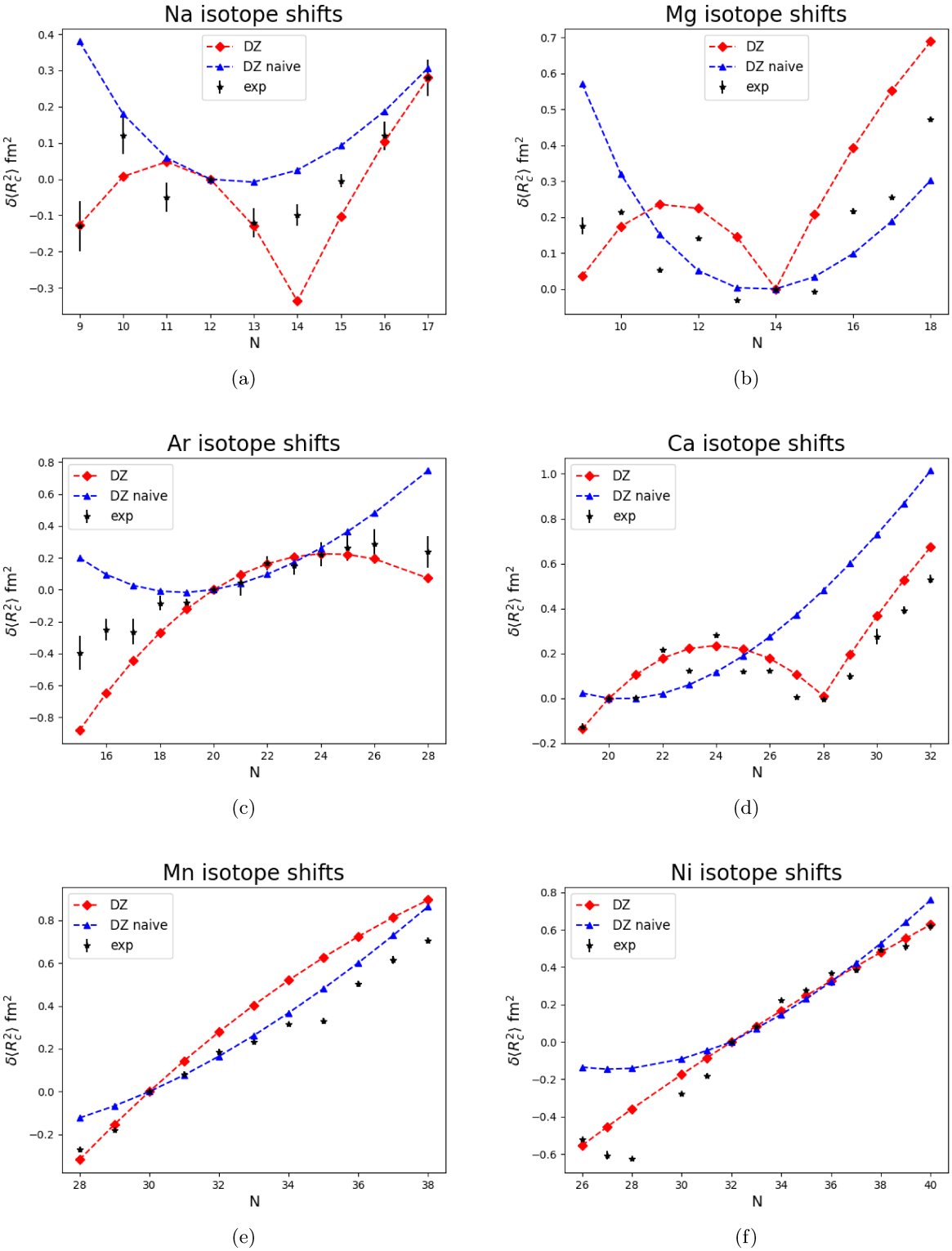

Figure 4.1: Isotope shifts for different isotopi chains. The results of the fit of Eq. (3.9) are shown in red (diamonds) and of Eq. (3.7) in cyan (triangles), compared to the experimental data in blue (stars), which come from Ref. [5] for the Na, Ar and Ca isotopic chains, from Ref. [40] for the Mg isotopic chain, from Ref. [6] for the Mn isotopic chain and from Ref. [41] and [42] for the Ni one.

the macroscopic formula.
Note that the E.I. closure for Na, at $A = 25$, is largely overestimated, as well as for Mg, at $A = 26$, meaning that at the closure the resulting isotope shift is much smaller than the neighbouring ones. Considering then the Ar nuclei, for the $N = 15 - 18$ isotopes the isotope shifts are underestimated, while the trend afterwords seems to be well described.

Isotopic chain	Na	Mg	Ar	Ca	Mn	Ni
rmsd for DZ [fm^2]	0.0990	0.1746	0.1978	0.0862	0.1644	0.0935
rmsd for DZ naive [fm^2]	0.1881	0.1537	0.2603	0.3174	0.0991	0.2231

Table 4.2: In this table the mean differences calculated via Eq. (4.1), between the experimental isotope shifts and the results from the fits obtained from Eq. (3.9) (DZ) and Eq. (3.7) (DZ naive) are reported.

Considering to the Ca isotopes, the "correlated" fit works very well, also predicting the increase after $N = 28$.
For the Mn isotopes the "correlated" fit deviates significantly from the experimental result, always overestimating the isotope shifts after $N = 30$.
Finally for the Ni isotopes the "correlated" fit follows well enough the rather linear experimental trend; notice that the Ni isotopes have $Z = 28$, so the Duflo correction does not contribute.

Considering then the "naive" fit results, it is clear that they do not really reproduce the data, but the isotope shifts predicted are always of parabolic shape, and can reproduce the data only in a limited mass region, deviating then greatly in the neutron and proton rich sides (look at the Ar isotopes for example). Another feature that they fail to predict is the decrease near the EI closure (for example this is clear in the Ca isotopes).

From the "DZ correlated" fit parameters, and thus from the calculated ρ_π^2, it is possible to obtain the corresponding "correlated" oscillator energy, $\hbar\omega_\pi$, by inverting (3.7):

$$\hbar\omega_\pi = \frac{41.47}{\rho_\pi^2} \sum_i \frac{m_i}{A}(p_i + 3/2) \tag{4.2}$$

Here an approximation is needed in order to extract $\hbar\omega_\pi$; in particular the occupation number will be determined assuming that each nucleon will occupy the next lowest-energy free orbit. Notice that this has a subtle and important difference with respect to the procedures listed above; in fact in this way all the orbits have the same radial extension, and what changes is only the $\hbar\omega_\pi$ for each nucleus. Clearly, the extracted h.o. energy parameter will have a different meaning depending on the radius used. If one plugs the result from the DZ "correlated" fit into Eq. (4.2), the corresponding extracted $\hbar\omega_\pi$ can be considered as the "correlated" energy parameter.
As it was already introduced in Chapter 3, one can also start from the "DZ correlated" fit, and *then* set $\lambda = 0$; doing this the result is the "uncorrelated" proton radii. Namely, the parameters used for the calculation of the radii using the Duflo-Zuker formula, i.e. Eq. (3.9), are the ones that are found in Table 4.1 but with $\lambda = 0$.
Using now this "uncorrelated" $\rho_\pi(\lambda = 0)$, inverting equation Eq. (4.2) one obtains the "uncorrelated" energy parameter $\hbar\omega_\pi(\lambda = 0)$, which will be employed for the microscopic calculations.

The same procedure holds for the "BLZ9" method introduced in Chapter 3 (Eq. (3.26)), which however takes into account only the proton occupations; in this case one has to replace m_i with z_i and A with Z.

It is important to stress that the fit has not been performed for each isotopic chain. This choice has been done so that only one set of parameters describes all the proton radii. This is the reason why for the nickel isotopes the DZ and DZ "naive" fit do not provide the same result: in fact, having the Ni isotopes $Z = 28$, the Duflo correction term is actually vanishing.

4.2 Theoretical Description of Isotopic Shifts

Following the description provided in Chapter 3 relative to the calculations of the isotope shifts, here the methods used are briefly summarized.
The first method is labelled as "BZ10", as it was proposed by Bonnard and Zuker in Eq. (10) of Ref. [14], and here it was reported as Eq. (3.24):

$$\langle r_\pi^2 \rangle = [\rho_\pi(\lambda = 0)]^2 + \frac{41.47}{\hbar\omega_\pi(\lambda = 0)} \sum_i \frac{m_i}{A} \delta_i$$

where $\hbar\omega_\pi(\lambda = 0)$ and $\rho_\pi(\lambda = 0)$ are obtained from the "uncorrelated" fit as discussed, so they are respectively the "uncorrelated" energy and proton radius.

The second method essentially represents a variant of the "BZ10" one, where this time the "uncorrelated" proton radius is calculated in a microscopic approach from the knowledge of $\hbar\omega_\pi(\lambda = 0)$ and of the occupation numbers m_i, as described in Eq. (3.25):

$$\langle r_\pi^2 \rangle = \frac{41.47}{\hbar\omega_\pi(\lambda = 0)} \sum_i \frac{m_i}{A} (p_i + 3/2 + \delta_i)$$

The results coming from this method will be labelled as "BZ3c".

In the last method, which was introduced in Ref. [13], the isospin representation is ditched, and only the proton occupancy are considered in the calculation of the proton radius, as described in the previously introduced Eq. (3.26):

$$\langle r_\pi^2 \rangle = \frac{41.47}{\hbar\omega_\pi(\lambda = 0)} \sum_i \frac{z_i}{Z} (p_i + 3/2 + \delta_i)$$

Concerning the values of the δ_i corrections, following the experimental status of the "halo" orbits (Ref. [14], [36]), a step function form has been employed, that is:

$$\delta^i = \begin{cases} \delta^i_> \text{ for } N, Z < 14, 28, \dots \\ \delta^i_< \text{ for } N, Z > 14, 28, \dots \end{cases}$$

depending on the i orbit in consideration. The values assumed are here reported:

$\delta^s_<$	$\delta^s_>$	$\delta^p_<$	$\delta^p_>$
4.9	1.4	4	1.5

Table 4.3: Summary of the values of δ assumed in this work

Notice that for isotopic chains which can be described by valence nucleons in only one shell, e.g. the *sd* shell, the "BZ10" and "BZ3c" methods will provide the same result. This happens because of the specific extraction method of the $\hbar\omega_\pi(\lambda = 0)$ parameter: when dealing with only one major shell, the principal quantum number p_i will not change, thus summing the mean occupations will give the same result as the approximation used.
This will be relevant for the Na and Mg isotopic chains, since they can be described by the valence *sd* shell.

Finally the occupation numbers have been calculated using the ANTOINE code explained in Section 2.3.2 using different interactions depending on the isotope considered. The quality of the interaction has been tested considering some excited states, comparing the results with the available experimental data. The comparison and the occupation numbers are reported in Appendix A.

4.3 Microscopic Description of the Isotope Shifts

4.3.1 The Na Isotopic Chain

In Fig. 4.2 the results of the isotopes shifts for the isotopic chain $^{20-28}$Na are reported.
For these nuclei the interaction chosen is the USDa [21], since the model space in which the effective interaction is employed consists of an ^{16}O inert core, while the valence space is composed of the *sd* shell for both nucleon types, and such valence space can then accommodate from 1 up to 12 valence neutrons and protons.

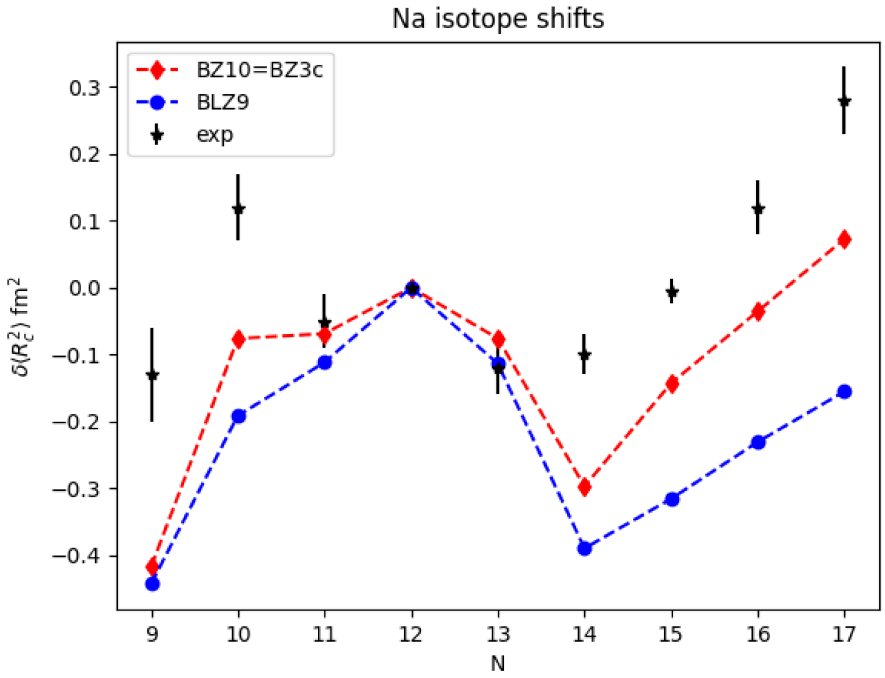

Figure 4.2: Isotope shifts in Na. The values of the isotope shifts from experimental data (black stars) are taken from Ref. [5]. The results coming from Eqs. (3.24) and (3.25) (red diamonds) and from Eq. (3.26) (blue dots) are reported. The reference isotope is ^{23}Na.

Since these isotopes are described using only the *sd* shell valence space, the "BZ10" and "BZ3c" methods are equivalent, thus one may refer to them collectively as "BZ".
All the methods overestimate the E.I. closure at $A = 25$, i.e. $N = 14$, in the sense that the results present a lower value for the isotope shift. This can be interpreted as the fact that at $N = 14$ the neutrons close a shell. Thus, one expects that such isotope should be more bound, so the radius is expected to be smaller.

The method that seems to better describe the data is "BZ" (Eqs. (3.24) and (3.25)), which works well also for $^{26-28}$Na in the neutron rich part, while "BLZ9" (Eq. (3.26)) underestimates the isotope shift for these isotopes.
All the methods present a sudden drop at $N = 9$, i.e. in the proton-rich isotope.
One can also appreciate that the slope after $N = 14$ is more closely followed by the "BZ" method, which however underestimates the isotope shifts. On the other hand the "BLZ9" method provides a less steep increase.

The values reported in table 4.4 suggest that the "BZ10" and "BZ3c" methods (i.e. obtained using Eqs. (3.24) and (3.25)), better reproduce the experimental data for the Na isotopic chain.

Method	"BZ10"	"BZ3c"	"BLZ9"
rmsd	0.1662 fm^2	0.1662 fm^2	0.2774 fm^2

Table 4.4: Calculated root mean square difference values via Eq. (4.1) for the three different method displayed in Fig. 4.2

4.3.2 The Mg Isotopic Chain

In Fig. 4.3 the results of the isotopes shifts for the isotopic chain $^{21-30}$Mg are reported.
For these nuclei the interaction chosen is the USDa [21]. The model space in which the effective interaction is employed consists of an ^{16}O inert core, while the valence space is composed of the *sd* shell for both nucleon types.

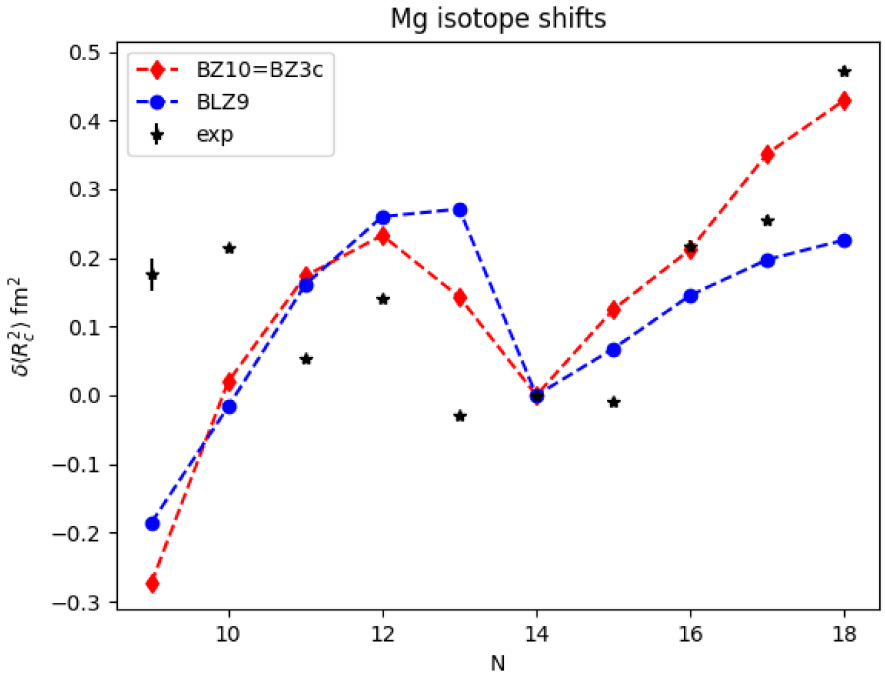

Figure 4.3: Isotope shifts in Mg. The values of the isotope shifts from experimental data (black stars) are taken from Ref. [40]. The results coming from Eqs. (3.24) and (3.25) (red diamonds) and from Eq. (3.26) (blue dots) are reported. The reference isotope is ^{26}Mg.

As in the previous case, the "BZ10" and "BZ3c" methods give the same result, so they can be collectively referred to as "BZ".

While both the "BZ" and "BLZ9" curves tend to deviate for odd-A isotopes of Mg, for the neutron-rich part the Eq. (3.24) formula tends to be in better agreement, while "BLZ9" tends to underestimate the values.
In the proton-rich part, in particular for the $^{21-22}$Mg isotopes, both methods largely underestimate the data.
It is clear that both curves tend to overestimate the closure at $A = 26$, where $N = 14$; this feature has also been found using chiral effective field theory methods in [43]. In this work only even-A Mg isotopes are reported, however it is clear that even with state of the art three-nucleon forces calculations the values of ^{24}Mg and ^{28}Mg are overestimated, while the isotope shift for ^{28}Mg is quite in agreement when Eqs. (3.24) and (3.25) are used.
Notice also that in [43] 13 harmonic oscillator orbits are considered, while in this work the valence space is only composed of the *sd* shell.

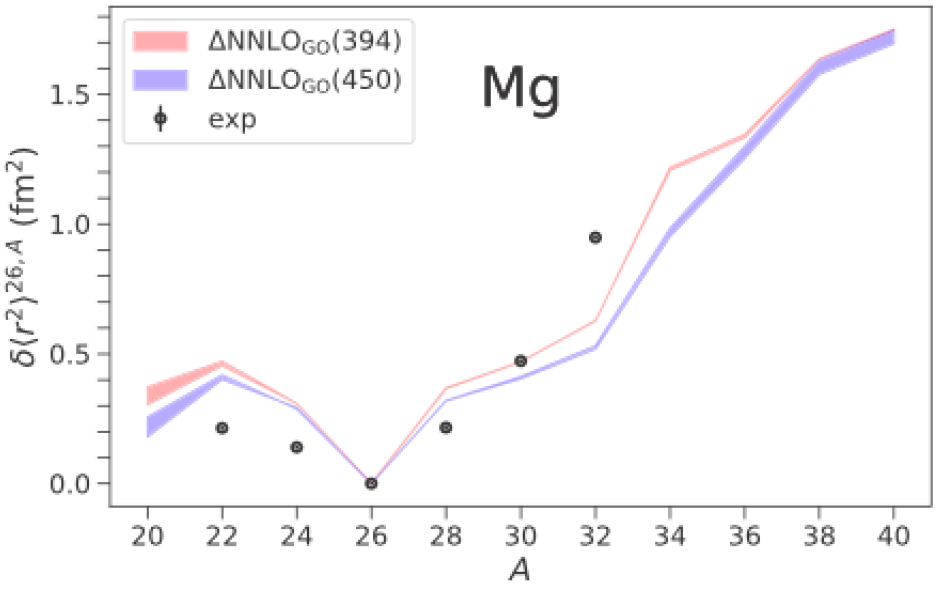

Figure 4.4: Isotope shifts in Mg. In this figure the results for the isotope shifts are shown; the predictions are labelled as $\Delta NNLO_{GO}(394/450)$, where 394/450 are the momentum cut-off in Mev units, and the bands represent the difference between an harmonic oscillator frequency of $\hbar\omega = 12$ MeV and 16 MeV.
The experimental data is also in this case taken from Ref. [5], and the reference isotope is ^{26}Mg. Figure taken from Ref. [43].

Method	"BZ10"	"BZ3c"	"BLZ9"
rmsd	0.1795 fm^2	0.1795 fm^2	0.1939 fm^2

Table 4.5: Calculated root mean square difference values via Eq. (4.1) for the three different method displayed in Fig. 4.4

Comparing the values present in Table 4.5 one concludes that the "BZ3c", obtained using Eq. (3.25), and "BZ10", obtained via Eq. (3.24), are the best in reproducing the experimental data for the Mg isotopic chain.

4.3.3 The Ar Isotopic Chain

In Fig. 4.5 the results for the isotope shifts for $^{33-45}Ar$ are reported.
In this case the number of protons is 18, just under the maximal number of protons that can be accommodated in the *sd* shell, so the chosen interaction is the USDa for ^{33}Ar only, while the calculations for all the other isotopes have been performed using the zbm2 interaction [25], which is defined on the model space composed of an inert core that is ^{28}Si, so it is suited for nuclei with $N, Z > 14$. The valence space consists of the orbits $1s_{1/2}$, $0d_{3/2}$, $0f_{7/2}$ and $1p_{3/2}$.

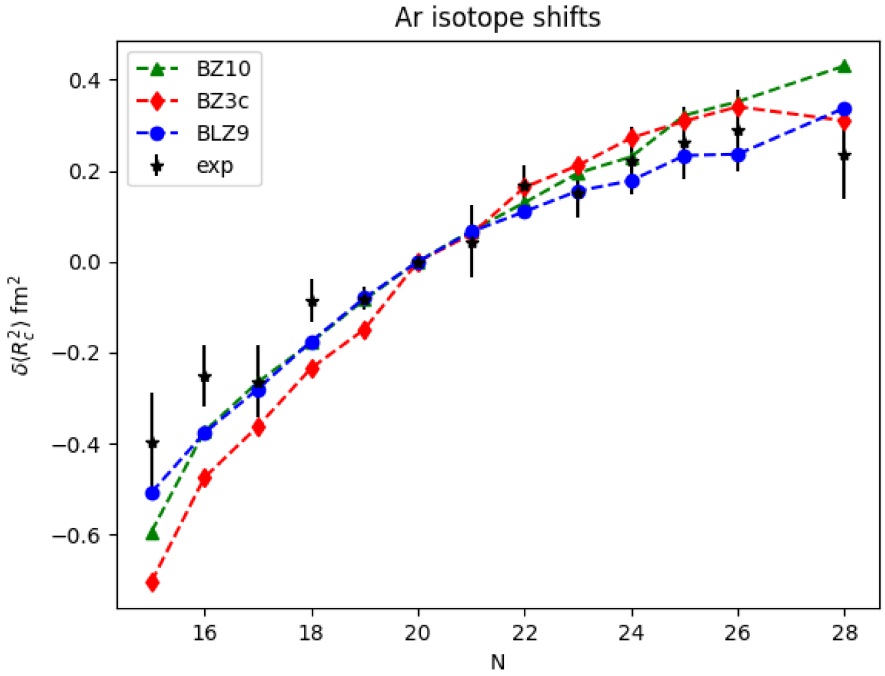

Figure 4.5: Isotope shifts in Ar. The values of the isotope shifts from experimental data (black stars) are taken from Ref. [5]. The results coming from Eq. (3.24) (green triangles), from Eq. (3.25) (red diamonds) and from Eq. (3.26) (blue dots) are reported. The reference isotope is ^{38}Ar.

All three methods do a good job and are mostly within 3σ from the experimental data.
"BZ3c" produces the lowest values for the isotope shifts in the range $^{33-37}$Ar, but it predicts well the decrease at ^{36}Ar.

Method	"BZ10"	"BZ3c"	"BLZ9"
rmsd	0.0929 fm^2	0.1238 fm^2	0.0658 fm^2

Table 4.6: Calculated root mean square difference values via Eq. (4.1) for the three different method displayed in Fig. 4.5

Comparing the values present in Table 4.6 one concludes that the "BLZ9" method (i.e. obtained using Eq. (3.26)), is the best in reproducing the experimental data for the Ar isotopic chain.

4.3.4 The Ca Isotopic Chain

In Fig. 4.6 the results for the isotope shifts for $^{40-52}$Ca are reported.
In this case the interaction chosen is the SDPF-U-MIX [26]. This interaction has a core composed of the $0s_{1/2}$, $0p_{3/2}$ and $0p_{1/2}$ orbits for both neutrons and protons (^{28}O core). The valence space is composed of the *sd* and *pf* shells for both neutrons and protons.

In this case the "correlated" DZ fit worked well, especially in reproducing the experimental fact that

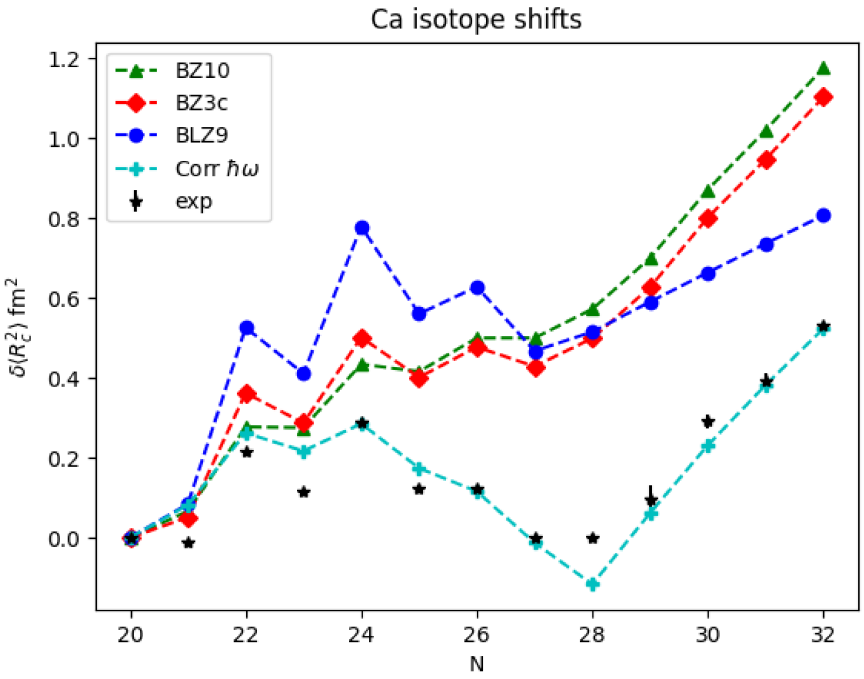

Figure 4.6: Isotope shifts in Ca. The values of the isotope shifts from experimental data (black stars) are taken from Refs. [5] and [7]. The results coming from Eq. (3.24) (green triangles), from Eq. (3.25) (red diamonds), from Eq. (3.26) (blue circles) and form Section 4.3.4 (cyan crosses) are reported. The reference isotope is ^{40}Ca.

^{40}Ca and ^{48}Ca have nearly the same radius.
The three methods employed, i.e. "BZ10", "BZ3c" and "BLZ9", present problems in producing the drop at $A = 48$, all remaining very high above the experimental data.
This seems to be due to the fact that the naive $\hbar\omega_\pi(\lambda = 0)$ and $\rho_\pi(\lambda = 0)$ bring on a major contribution, leading to the increase. Indeed looking at the "uncorrelated" fitted isotope shifts for Ca isotopes in Fig. 4.7 it is clear that they are well above the experimental results, and adding the correction for the "halo" orbits only further worsen the situation. In this case the Duflo correction is necessary in order to obtain the right trend, and the microscopic formulation cannot explain it starting from the "uncorrelated" energy parameter $\hbar\omega_\pi(\lambda = 0)$ and radius $\rho_\pi(\lambda = 0)$.
One can notice that the "BZ10" and "BZ3c" methods actually provide the right slope for the sudden increase in the isotope shifts after $A = 28$, while the "BLZ9" method has a much less steep slope.

A fourth method has been added in this case, also present in Fig. 4.6 which comes from:

$$\langle r_\pi^2\rangle = \frac{41.47}{\hbar\omega_\pi}\sum_i \frac{m_i}{A}(p_i + 3/2)$$

where $\hbar\omega_\pi$ is now the correlated value extracted from the fit, so the δ's are not needed since in this oscillator energy the effect of the λ term is already accounted for. This reproduces the results arguably better than the "correlated" fit presented in Fig. 4.1, also having the wanted staggering, and even the data after $A = 48$ is reproduced better.

Being the shape so peculiar, considering only the occupations of the $s_{1/2}$ orbit (which has a high occupation number, for the protons it has a mean occupation of 1.58 and for the neutrons of 1.73) and the $p_{3/2}$ (which is not occupied, at least for protons it has a mean occupation of 0.1, and also for neutrons since up to ^{49}Ca it never reaches 1 full neutron in that orbit), it fails to be reproduced starting from the monotonic naive fitted parameters.

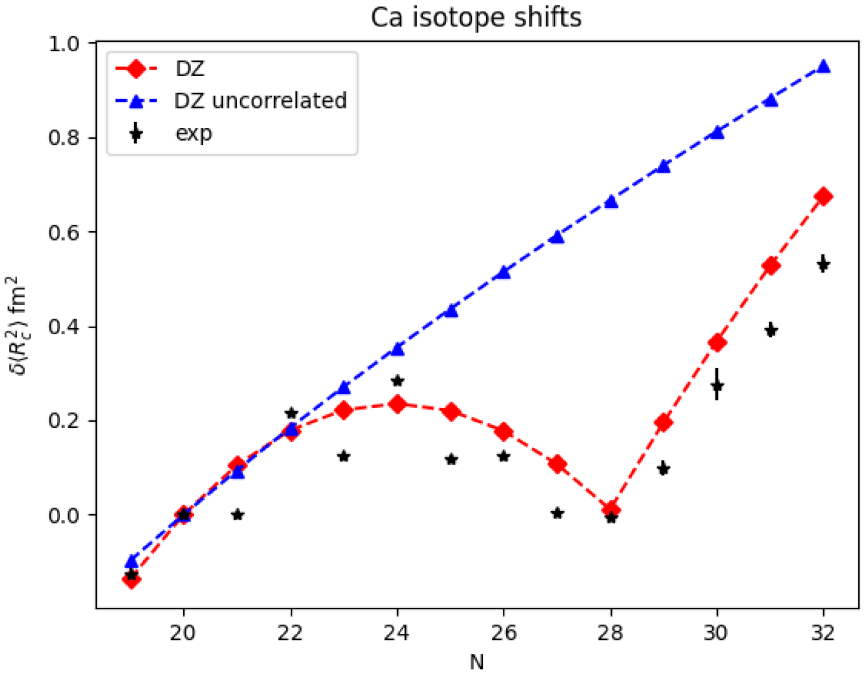

Figure 4.7: Isotope shifts in Ca. In this figure the results from the "uncorrelated" Duflo-Zuker formula (blue triangles) and the "correlated" one (red diamonds) are compared. The experimental data (black stars) is taken from [5]. The reference isotope is ^{40}Ca.

Another method has been explored, which comes from the procedure explained in [25], where the isotope shifts are considered to be only due to cross-shell excitations of the protons from the *sd* to the *pf* shell. In this way Eq. (3.28) can be used in order to estimate the isotope shifts:

$$\delta\langle r_\pi^2\rangle^{A,40} = \left(\frac{41.47}{\hbar\omega_\pi}\cdot\frac{z_{0f_{7/2}}+z_{1p_{3/2}}}{Z}\right)^A - \left(\frac{41.47}{\hbar\omega_\pi}\cdot\frac{z_{0f_{7/2}}+z_{1p_{3/2}}}{Z}\right)^{A=40}$$

where it is subtracted the value for $\delta\langle r_\pi^2\rangle^{A=40}$.
Considering Fig. 4.8, this methods work well for reproducing the downfall at $A = 48$, and the staggering feature is present. However the estimate from Eq. (3.28) does not predict the rapid increase after ^{48}Ca, and it actually continues to diminish.

4.3.5 The Mn Isotopic Chain

In Fig. 4.9 the results for the isotope shifts for the $^{53-63}$Mn isotopes are shown.
The effective interaction used for the calculations is the GXPF1a [27] for the $^{50-59}$Mn isotopes, which is defined on the model space composed of the ^{40}Ca nucleus inert core, while the valence space is the *pf* shell for both fluids. This means that the number of valence nucleons and protons that can be accommodated is 20.
The interaction employed for the $^{60-63}$Mn isotopes is the LNPS [28], which has a inert core composed of ^{48}Ca. The valence space is composed of the *pf* shell for the protons, while for the neutrons it is composed of the $0f_{5/2}$, $1p_{3/2}$, $1p_{1/2}$, $0g_{9/2}$ and $1d_{5/2}$. The change of interaction is done since after $N = 35$ the $0g_{9/2}$ and $1d_{5/2}$ neutron orbits starts to be occupied: for ^{60}Mn the neutron occupation predicted by the LNPS interaction is $n_{0g_{9/2}+1d_{5/2}} = 0.24$, and for ^{61}Mn is $n_{0g_{9/2}+1d_{5/2}} = 1.37$, so the contributions of these two orbits start to be important.

In this case the curves "BZ10" and "BZ3c" only differ appreciably after $A = 59$. in the neutron rich region after $A = 56$ the "BLZ9" curve is always lower then the other two. In this case this makes it better agree with the experimental data, well reproducing the experimental trend.

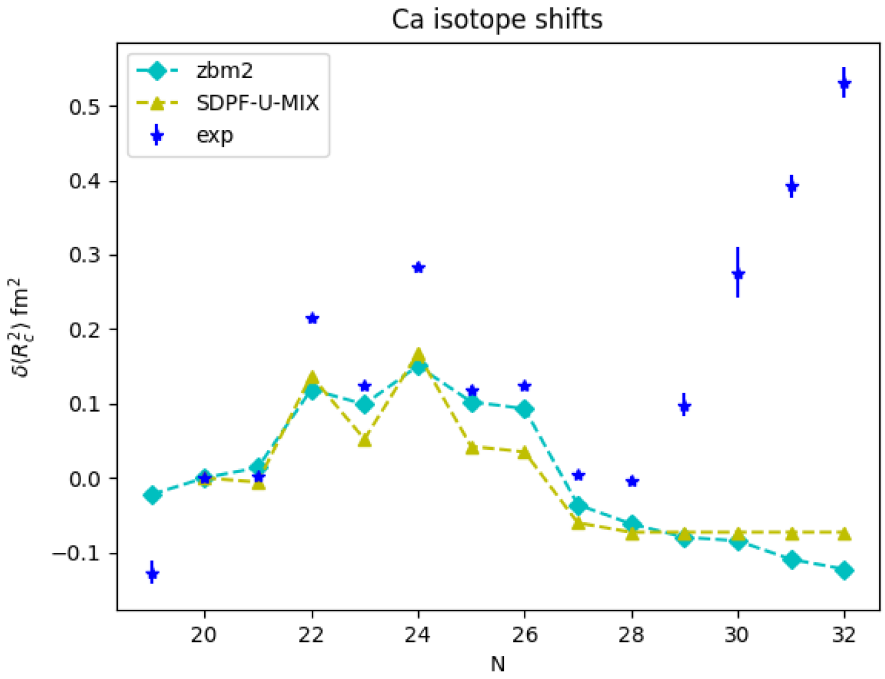

Figure 4.8: Isotope shifts in Ca. The values of the isotope shifts from experimental data (blue stars) are taken from Ref. [5] and [7]. The results from Eq. (3.28) using the interactions zbm2 (cyan diamonds) and SDPF-U-MIX (yellow triangles) are reported. The employed energy parameter is the "uncorrelated" $\hbar\omega_\pi(\lambda = 0)$.The reference isotope is ^{40}Ca.

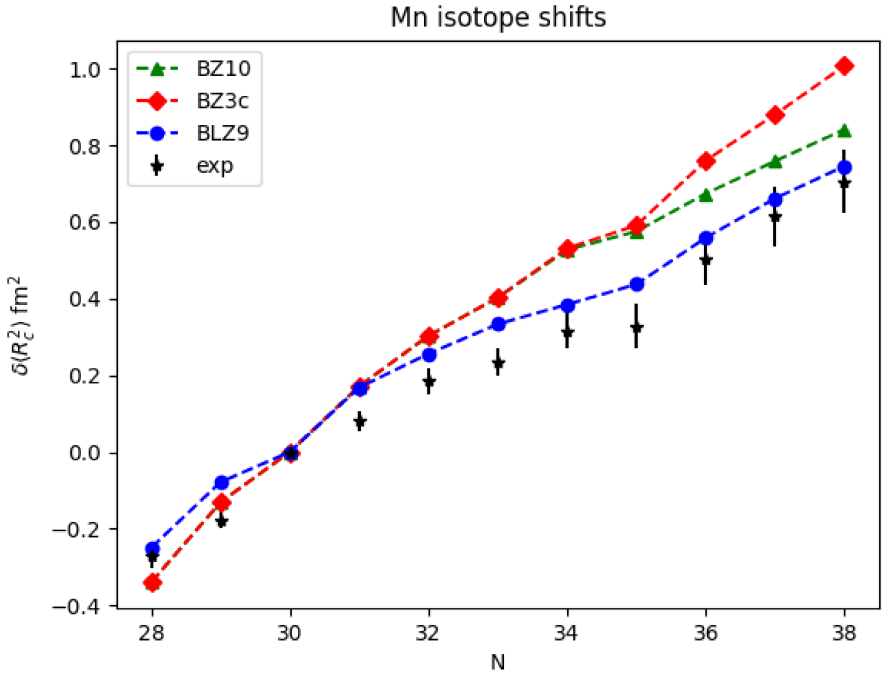

Figure 4.9: Isotope shifts in Mn. The values of the isotope shifts from experimental data (black stars) are taken from Ref. [6]. The results from Eq. (3.24) (green triangles), from Eq. (3.25) (red diamonds) and from Eq. (3.26) (blue dots) are reported. The reference isotope is ^{55}Mn.

A change of trend can be appreciated at $N = 35$, presented by all three methods. However only the "BZ3c" and the "BLZ9" methods predict the right slope.

Notice that from the interaction used in order to calculate the occupancy numbers of the ground states of the various Mn isotopes the $0g_{9/2}$ and $2d_{3/2}$ are also contained in the valence space, only for the neutrons. So one should also add a δ_d term in order to take into account the fact that the d orbit is the "halo" orbit in this shell; not having much information about it, having only considered two isotopic chains which include these orbits (Mn and Ni), and also considering the fact that the d orbit is scarcely populated, δ_d was set to zero.
However, it seems that a smaller value for it would work better, at least for "BZ10" and "BZ3c", since it will tend to give higher values of the isotope shifts for the highest-mass isotopes, and those methods already overestimate them. Moreover, as it can be seen in Section 4.1, the DZ fit itself overestimates the isotope shifts in the $N = 32-38$ region, so one may also conclude that a better fit would provide a more accurate $\hbar\omega_\pi(\lambda = 0)$ parameter, which in turn would lower the calculated isotope shifts.

Method	"BZ10"	"BZ3c"	"BLZ9"
rmsd	0.1448 fm^2	0.1905 fm^2	0.0712 fm^2

Table 4.7: Calculated mean difference values via Eq. (4.1) for the three different method displayed in Fig. 4.9

Comparing the values present in Table 4.7 one concludes that the "BLZ9" method (i.e. obtained using Eq. (3.26)), is the best in reproducing the experimental data for the Mn isotopic chain.

4.3.6 The Ni Isotopic Chain

In Fig. 4.10 the results for the isotope shifts for the $^{54-66}$Ni isotopes are shown.

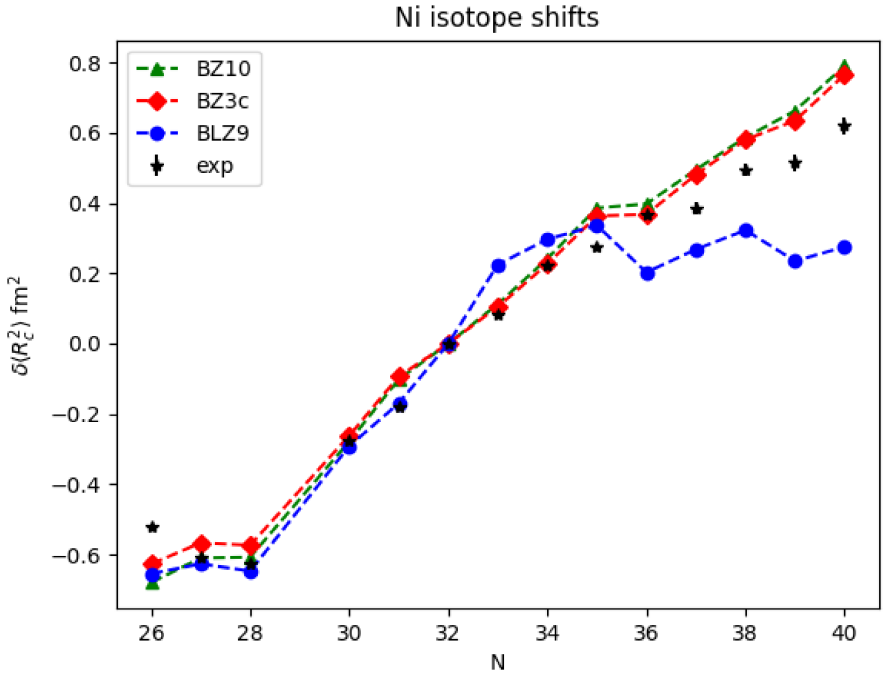

Figure 4.10: Isotope shifts in Ni.The values of the isotope shifts from experimental data (black stars) are taken from Ref. [41] for $^{54-58/60}$Ni and in Ref. [42] for $^{61-68}$Ni. The results from Eq. (3.24) (green triangles), from Eq. (3.25) (red diamonds) and from Eq. (3.26) (blue dots) are reported. The reference isotope is ^{60}Ni.

The effective interaction used for the calculations is the GXPF1a [27] for the $^{54-64}$Ni isotopes, which is defined on the model space composed of the ^{40}Ca inert core, while the valence space is the pf shell for both fluids. The interaction employed for the $^{65-70}$Ni isotopes is the LNPS [28], which has a inert core composed of ^{48}Ca. The valence space is composed of the pf shell for the protons, while for

the neutrons it is composed of the $0f_{5/2}$, $1p_{3/2}$, $1p_{1/2}$, $0g_{9/2}$ and $1d_{5/2}$. The change of interaction is done since after $N = 37$ the $0g_{9/2}$ and $1d_{5/2}$ neutron orbits starts to be occupied: for ^{65}Ni the neutron occupation predicted by the LNPS interaction is $n_{0g_{9/2}+1d_{5/2}} = 0.48$, and for ^{66}Ni is $n_{0g_{9/2}+1d_{5/2}} = 0.77$, so the contributions of these two orbits start to be important.

Nickel is a special case, since it has $Z = 28$ and this implies a zero Duflo term in Eq. (3.9); in this case the correlated and naive fit will give the same result.
The overall behaviour of the isotope shift is followed quite closely by both "BZ10" and "BZ3c" curves, while "BLZ9" predicts lower values of the isotope shifts for $^{64-68}$Ni.

Method	"BZ10"	"BZ3c"	"BLZ9"
rmsd	0.0916 fm^2	0.0772 fm^2	0.1497 fm^2

Table 4.8: Calculated root mean square difference values via Eq. (4.1) for the three different method displayed in Fig. 4.10

Comparing the values in Table 4.8 one concludes that the "BZ3c" method (i.e. obtained using Eq. (3.25)), is the best in reproducing the experimental data for the Ni isotopic chain.

Summing all the calculated rmsd for the three methods employed for each isotopic chains, one obtains:

Method	"BZ10"	"BZ3c"	"BLZ9"
Total rmsd	0.675 fm^2	0.7372 fm^2	0.758 fm^2

Table 4.9: Calculated total root mean square difference values, obtained by summing the values present in Tables 4.4 to 4.8.

The best method considering the isotopic chains Na, Mg, Ar, Mn and Ni has been found to be the "BZ10".

Chapter 5

Conclusions

The nuclear radius is a fundamental property of the nucleus. It represent an important probe of the nuclear interaction which dictates the behaviour of the nucleons inside the nucleus. Investigations of the exotic nuclei regions, i.e. the proton- and neutron-rich isotopes, are a crucial goal for future experimental campaigns as well as for the theoretical developments. In this regard, recent experimental findings [7] for the neutron-rich Ca isotopes have put in evidence a sudden rise of the isotope shifts after $N = 28$. While an increase in radii is related to nuclear deformations, for Ca isotopes this is not the case since they are spherical. This has puzzled the theoretical interpretations.

This work aimed to find, discuss and apply a method, based on previous studies, which could describe the behaviour of the experimental isotope shifts and, at the same time, help with the interpretation of the results. In particular, Shell Model calculations have been performed, in the harmonic oscillator basis, and two main ingredients have been crucial to get a satisfactory description of the experimental data.
The first one concerns the harmonic oscillator energy, the $\hbar\omega$ parameter. This can be obtained from the Duflo-Zuker phenomenological formula [12], and it represents an improvement with respect to the monotonic Bohr-Mottelson form.
The second ingredient consists of corrections that account for the larger spatial extension of the lowest-ℓ orbits in a main shell, which are the so-called "halo" orbits [13]. These corrections have been suggested in Ref. [14] to account for the Duflo-Zuker correlations in a microscopic approach. Notably, the studies done by Bonnard and collaborators [13, 14] suggest that δ_i correction factors are not constant with respect to the neutron and proton numbers, but they can be described in a first approximation as a step function discontinuous at the extruder-intruder shell closures (e.g. $N, Z = 14, 28$). Indeed, the orbital radii of low-ℓ orbits reduce considerably when these orbits are occupied by at least a nucleon.

Three different microscopic prescriptions have been applied:

- the "BZ10" method, given by Eq. (3.24), which employs an isospin representation (thus only involve the total occupation number $m_i = n_i + z_i$) and uses the result coming from the Duflo-Zuker formula for the "uncorrelated" square radius;
- the "BZ3c" method, given by Eq. (3.25), which also uses an isospin representation but calculates the "uncorrelated" square radius in a microscopic approach;
- the "BLZ9" method, given by Eq. (3.26), which only considers the contributions from the protons.

Overall, of these three methods, the one that described better the Na, Mg, Ar, Mn and Ni isotopic chains was found to be the "BZ10" method.

In the future these methods can be applied to other isotopic chains, allowing for a better understanding of their merits as well as their shortcomings. The evolution of the δ_i correction factors with respect to the mass number A as well as its dependence on the isospin t_z is still not understood: one may try to find an ansatz for a functional representation $\delta_i(A, t_z)$, to get a best fit of the available data on isotope shifts for a variety of mass regions.

Moreover, the results from the phenomenological Duflo-Zuker formula (Eq. (3.9)) can still be improved, for example by expanding the number of fitted radii, or, as hinted in Ref. [14], by supplementing the Duflo-Zuker formula with an isovector term.

Finally, the behavior of the calcium isotopes is still challenging since it seems to be well-reproduced by considering only the "cross-shell excitations" between the sd and pf protons shells. However, this prescription only works in a very limited mass region ($N = 19 - 28$) and fails to reproduce the rapid increase of the radius after $N = 28$.
The three microscopic methods employed in this work give the correct slope for the increase after $N = 28$, thus interpreting the increase in isotope shifts with the occupation by neutrons of the low-ℓ orbit $p_{3/2}$. However, they do not describe well the parabolic behaviour of the isotope shifts for lighter isotopes.

In summary, in this thesis work we have explored different methods to obtain the isotopic shifts along a variety isotopic chains, from $Z = 11$ to $Z = 28$. In all cases the parameters used have been maintained constant without the scope of getting a best or "ad hoc" fit. The goal was to understand the role of the "halo" orbits in driving the radial behavior. The description of data is very satisfactory and this work paves the way for future studies.

Appendix A

Shell Model Calculations

In this appendix the occupation numbers obtained via the ANTOINE code [22], using the different effective interactions discussed in Chapter 2, will be reported. Also a selection of the excitation energy of some yrast states will be reported, in order to display how they describe the various isotopes, and compared with the available experimental data coming from [44].
These interaction have already been tested, in particular in the regions of the chart of nuclides important or this thesis' work (see Refs. [45], [46], [47], [48]).

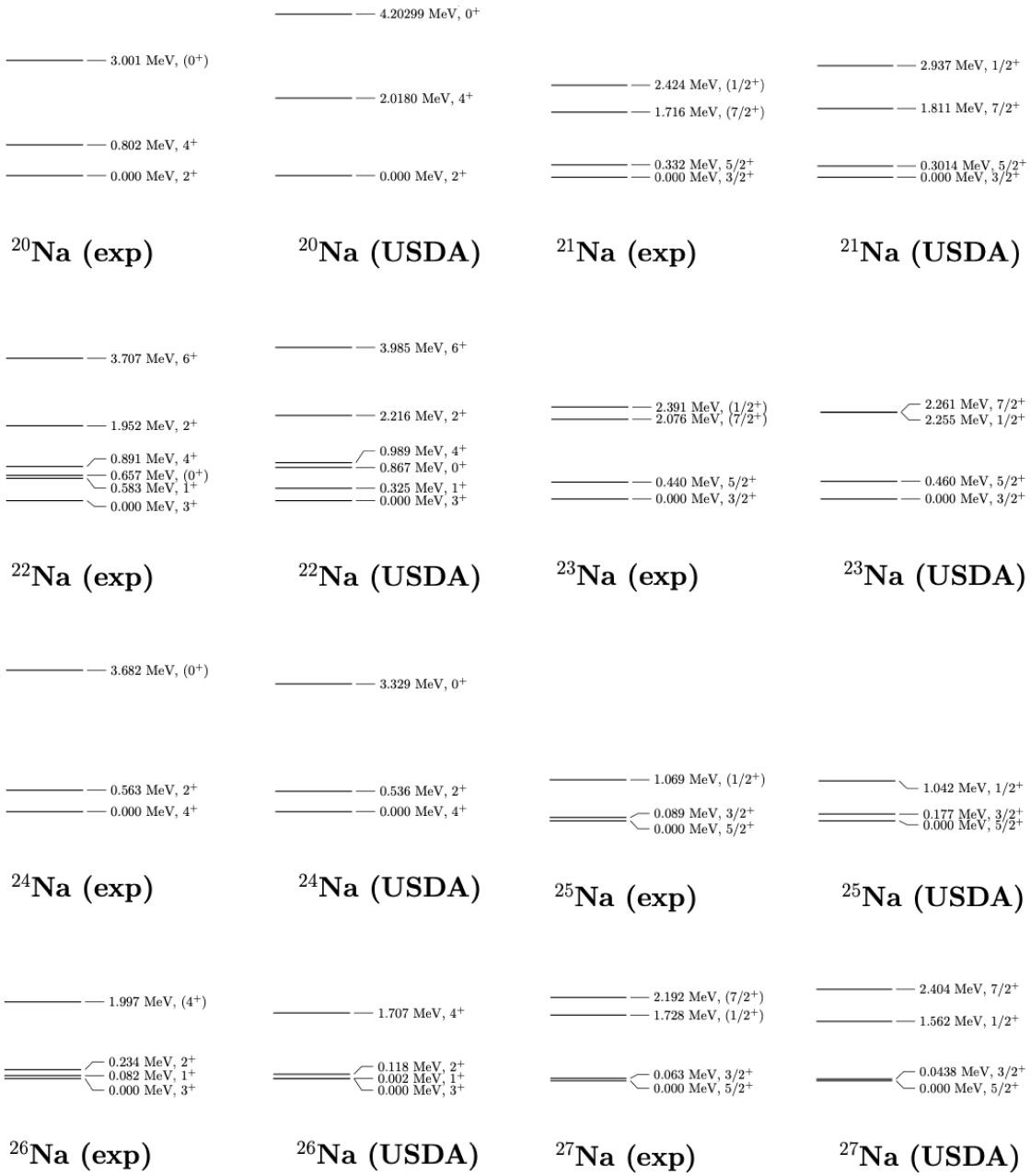

Figure A.1: Energy levels for the $^{20-27}$Na isotopes calculated via the USDa interaction [21] and then compared with the experimental ones [44].

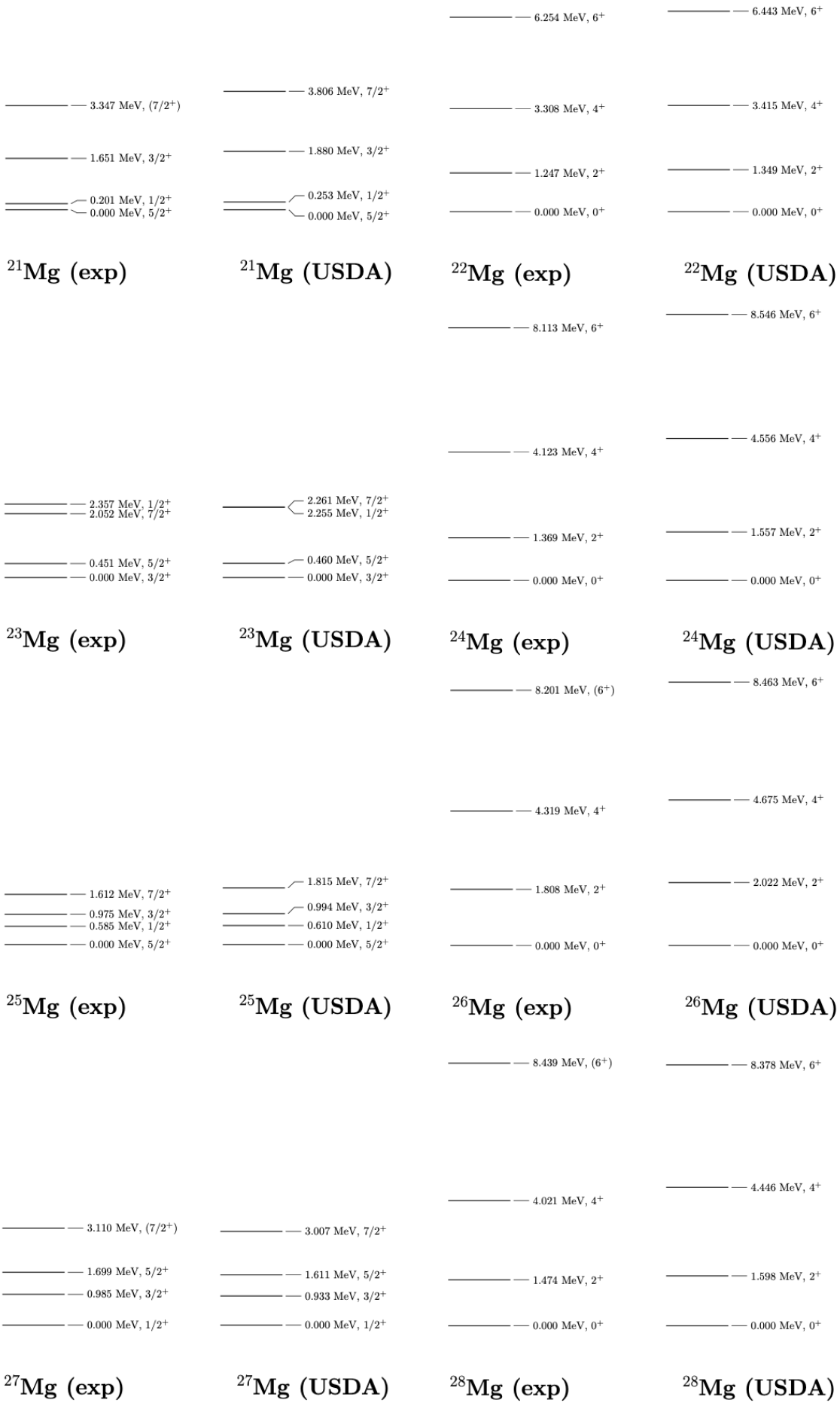

Figure A.2: Energy levels for the $^{21-28}$Mg isotopes calculated via the USDa interaction [21] and then compared with the experimental ones [44].

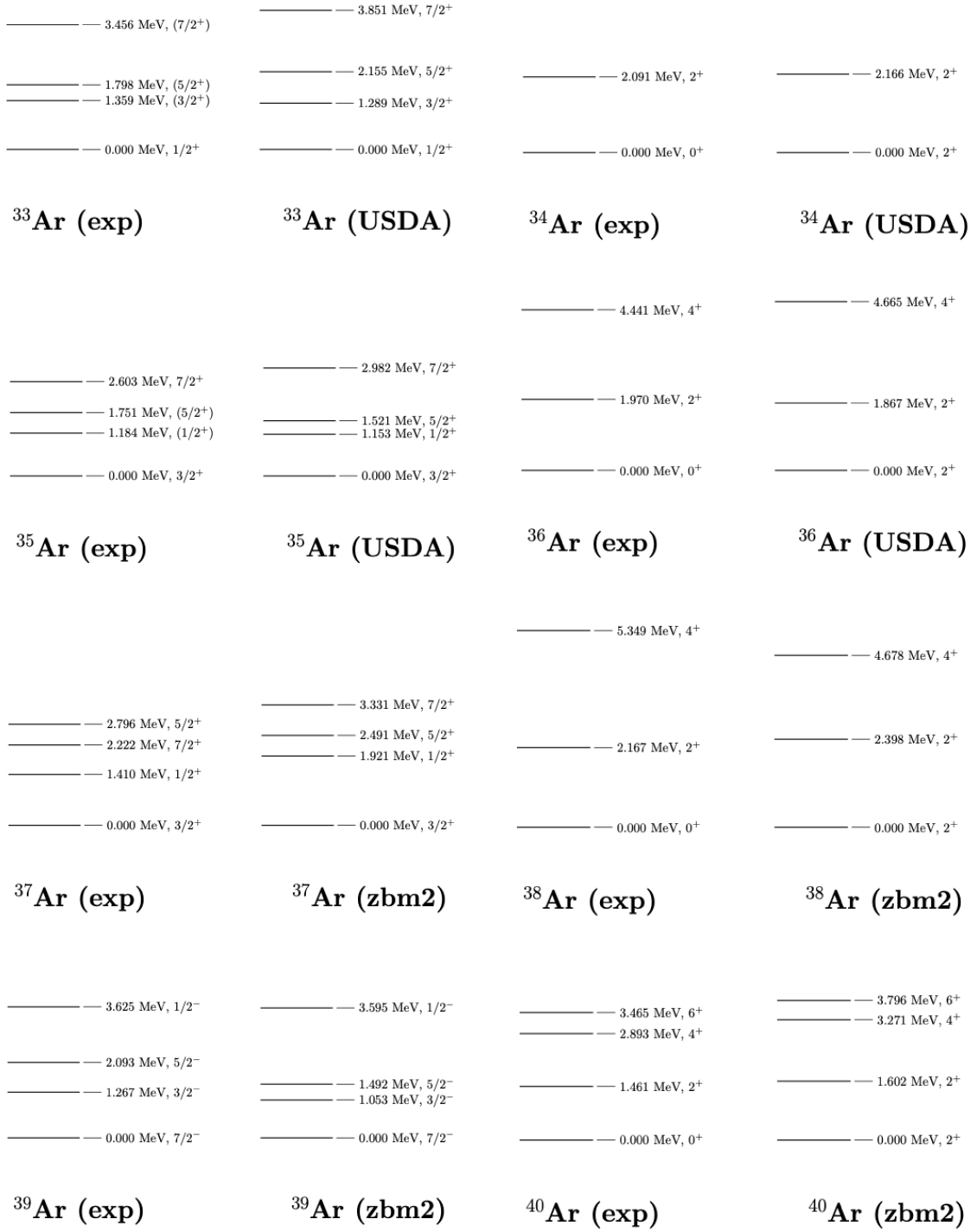

Figure A.3: Energy levels for the $^{33-36}$Ar isotopes calculated via the USDa interaction [21] and $^{37-40}$Ar via the zbm2 interaction [25], then compared with the experimental ones [44].

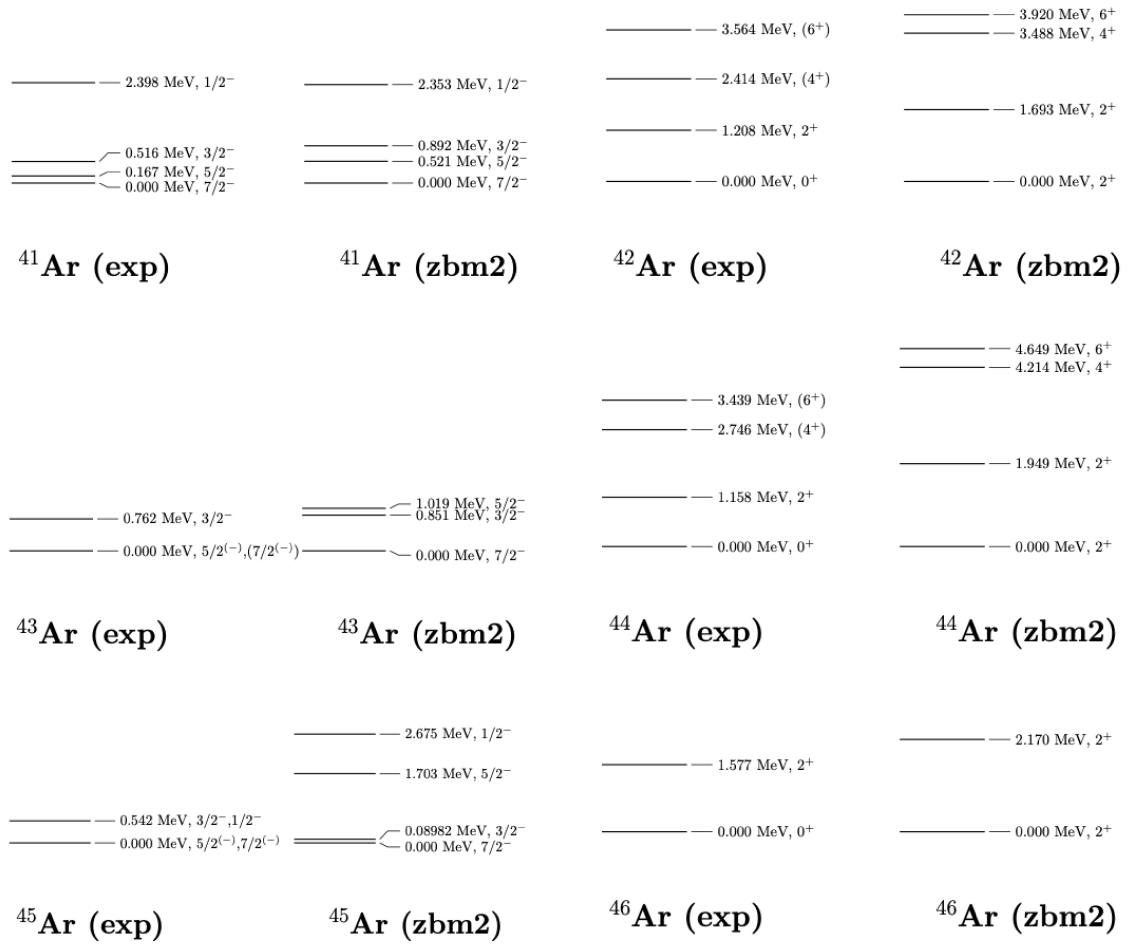

Figure A.4: Energy levels for the $^{41-46}$Ar isotopes calculated via the zbm2 interaction [25], then compared with the experimental ones [44].

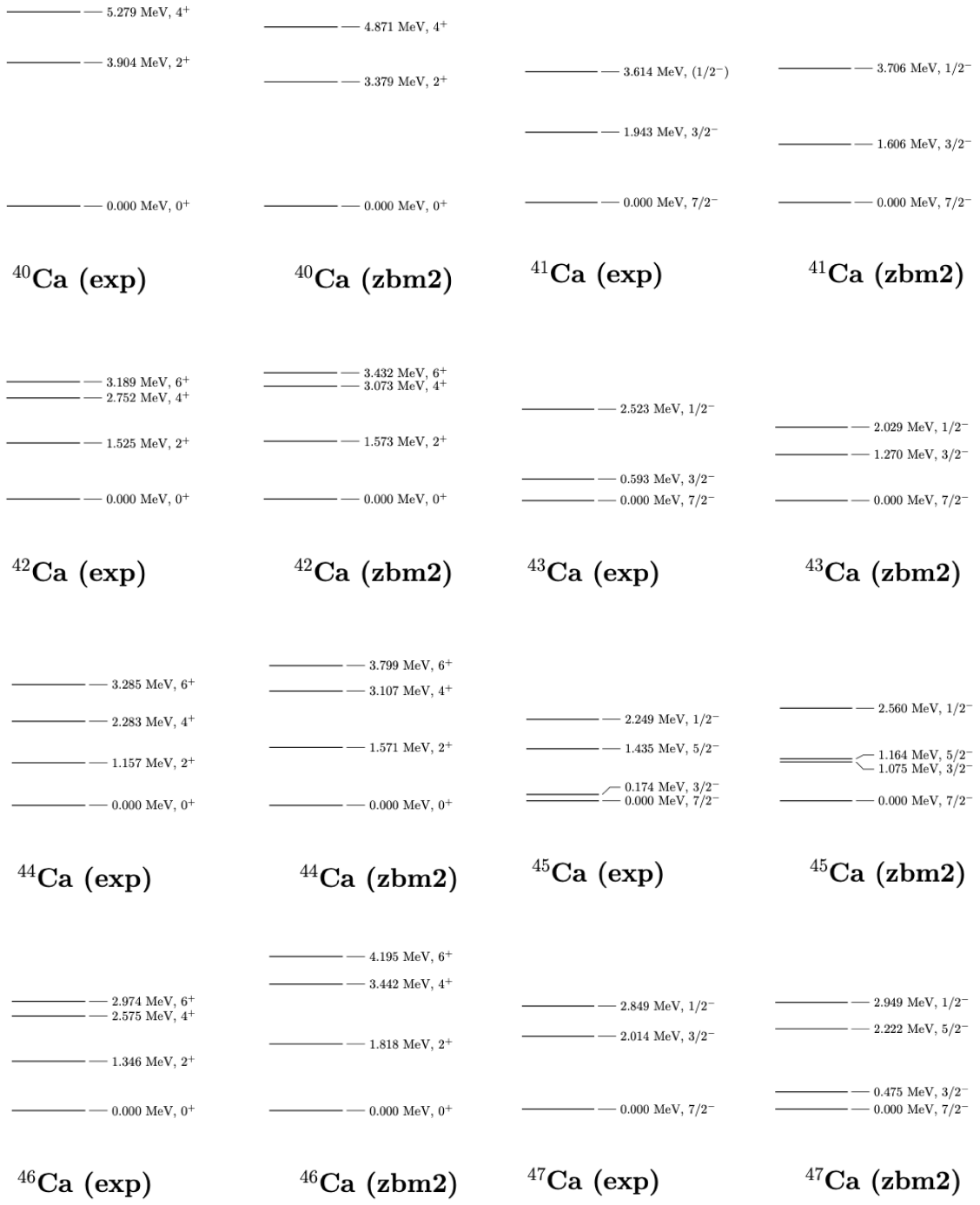

Figure A.5: Energy levels for the $^{40-47}$Ca isotopes calculated via the zbm2 interaction [25] and then compared with the experimental ones [44].

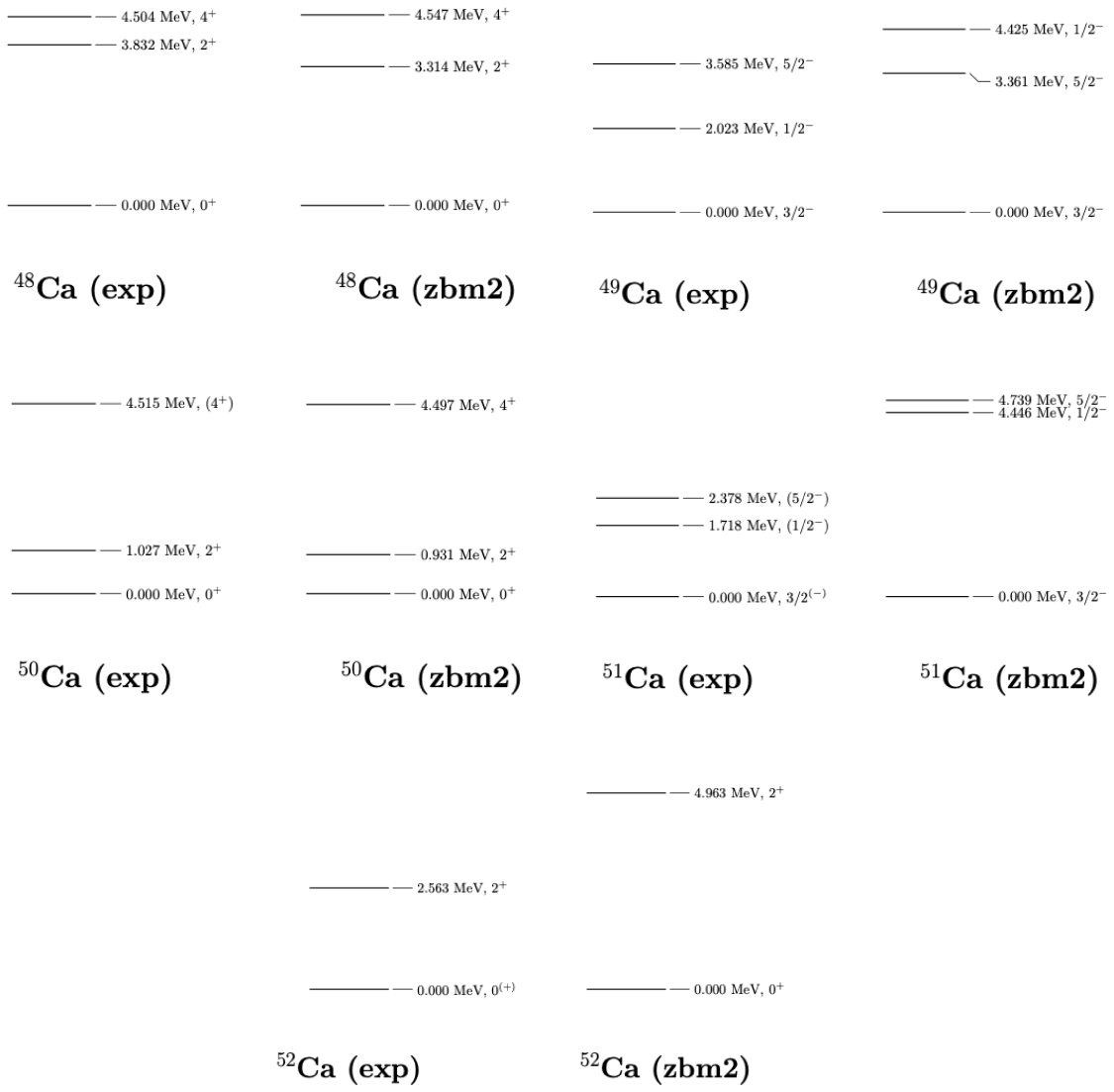

Figure A.6: Energy levels for the $^{48-52}$Ca isotopes calculated via the zbm2 interaction and then compared with the experimental ones [44].

Figure A.7: Energy levels for the Ni isotopes calculated via the GXPF1a interaction [27] for $^{54-64}$Ni isotopes and with the LNPS interaction [28] for $^{64-70}$Ni ones; the results are then compared with the experimental ones [44].

Isotope	g.s.	$\pi\ d_{5/2}$	$\pi\ s_{1/2}$	$\pi\ d_{3/2}$	$\nu\ d_{5/2}$	$\nu\ s_{1/2}$	$\nu\ d_{3/2}$
^{20}Na	2^+	2.43	0.33	0.23	0.68	0.23	0.09
^{21}Na	$3/2^+$	2.26	0.45	0.29	1.28	0.50	0.23
^{22}Na	3^+	2.28	0.44	0.28	2.28	0.44	0.28
^{23}Na	$3/2^+$	2.26	0.45	0.28	3.07	0.44	0.49
^{24}Na	4^+	2.41	0.31	0.28	4.18	0.37	0.45
^{25}Na	$5/2^+$	2.59	0.17	0.24	4.94	0.53	0.53
^{26}Na	3^+	2.61	0.18	0.22	5.38	1.09	0.54
^{27}Na	$5/2^+$	2.59	0.22	0.19	5.60	1.36	1.04
^{28}Na	1^+	2.60	0.25	0.15	5.81	1.70	1.49

Table A.1: Occupation numbers of the valence orbits for the Na isotopes as calculated via the USDa interaction.

Isotope	g.s.	$\pi\ d_{5/2}$	$\pi\ s_{1/2}$	$\pi\ d_{3/2}$	$\nu\ d_{5/2}$	$\nu\ s_{1/2}$	$\nu\ d_{3/2}$
^{21}Mg	$5/2^+$	3.33	0.34	0.34	0.82	0.14	0.04
^{22}Mg	0^+	3.18	0.38	0.44	1.43	0.39	0.18
^{23}Mg	$3/2^+$	3.07	0.44	0.49	2.26	0.45	0.28
^{24}Mg	0^+	2.98	0.44	0.58	2.98	0.44	0.58
^{25}Mg	$5/2^+$	3.07	0.38	0.55	4.05	0.43	0.52
^{26}Mg	0^+	3.17	0.33	0.50	4.75	0.57	0.68
^{27}Mg	$1/2^+$	3.29	0.30	0.41	5.36	0.94	0.70
^{28}Mg	0^+	3.36	0.32	0.32	5.56	1.08	1.37
^{29}Mg	$1/2^+$	3.48	0.26	0.26	5.75	1.28	1.97
^{30}Mg	0^+	3.60	0.16	0.24	5.82	1.91	2.27

Table A.2: Occupation numbers of the valence orbits for the Mg isotopes as calculated via the USDa interaction.

Isotope	g.s.	$\pi\ d_{5/2}$	$\pi\ s_{1/2}$	$\pi\ d_{3/2}$	$\pi\ f_{7/2}$	$\pi\ p_{3/2}$	$\nu\ d_{5/2}$	$\nu\ s_{1/2}$	$\nu\ d_{3/2}$	$\nu\ f_{7/2}$	$\nu\ p_{3/2}$
^{32}Ar	0^+	5.81	1.54	2.65	0.00	0.00	5.28	0.43	0.29	0.00	0.00
^{33}Ar	$1/2^+$	6.00	1.80	1.72	0.39	0.09	6.00	0.94	0.02	0.03	0.01
^{34}Ar	0^+	6.00	1.82	1.71	0.37	0.11	6.00	1.71	0.16	0.11	0.02
^{35}Ar	$3/2^+$	6.00	1.82	1.72	0.36	0.09	6.00	1.82	0.98	0.16	0.04
^{36}Ar	0^+	6.00	1.77	1.68	0.46	0.09	6.00	1.77	1.68	0.46	0.09
^{37}Ar	$3/2^+$	6.00	1.81	1.68	0.43	0.08	6.00	1.86	2.62	0.43	0.09
^{38}Ar	0^+	6.00	1.74	1.71	0.47	0.08	6.00	1.82	2.97	1.06	0.15
^{39}Ar	$7/2^-$	6.00	1.67	1.79	0.47	0.07	6.00	1.81	3.01	2.00	0.18
^{40}Ar	0^+	6.00	1.44	1.92	0.57	0.07	6.00	1.66	2.72	3.33	0.29
^{41}Ar	$7/2^-$	6.00	1.36	2.04	0.53	0.06	6.00	1.67	2.81	4.19	0.33
^{42}Ar	0^+	6.00	1.11	2.22	0.61	0.06	6.00	1.49	2.70	5.41	0.40
^{43}Ar	$7/2^-$	6.00	1.15	2.32	0.48	0.05	6.00	1.64	3.03	5.90	0.44
^{44}Ar	0^+	6.00	0.92	2.56	0.47	0.05	6.00	1.50	3.08	6.96	0.46
^{45}Ar	$7/2^-$	6.00	1.18	2.41	0.36	0.05	6.00	1.95	3.83	6.79	0.42
^{46}Ar	0^+	6.00	0.96	2.67	0.32	0.04	6.00	1.96	3.84	7.73	0.47

Table A.3: Occupation numbers of the valence orbits for the Ar isotopes as calculated via the USDa interaction for ^{32}Ar and the zbm2 interaction for all the other isotopes.

Isotope	g.s.	$\pi\ d_{5/2}$	$\pi\ s_{1/2}$	$\pi\ d_{3/2}$	$\pi\ f_{7/2}$	$\pi\ p_{3/2}$	$\nu\ d_{5/2}$	$\nu\ s_{1/2}$	$\nu\ d_{3/2}$	$\nu\ f_{7/2}$	$\nu\ p_{3/2}$
^{39}Ca	$3/2^+$	6.00	1.85	3.17	0.86	0.13	6.00	1.85	2.54	0.52	0.09
^{40}Ca	0^+	6.00	1.80	3.09	0.98	0.12	6.00	1.80	3.09	0.98	0.12
^{41}Ca	$7/2^-$	6.00	1.76	3.06	1.06	0.12	6.00	1.78	3.09	1.99	0.14
^{42}Ca	0^+	6.00	1.49	2.74	1.61	0.15	6.00	1.55	2.73	3.47	0.24
^{43}Ca	$7/2^-$	6.00	1.48	2.86	1.53	0.13	6.00	1.57	2.89	4.28	0.26
^{44}Ca	0^+	6.00	1.24	2.81	1.82	0.13	6.00	1.38	2.82	5.48	0.32
^{45}Ca	$7/2^-$	6.00	1.32	2.99	1.59	0.09	6.00	1.54	3.13	5.99	0.35
^{46}Ca	0^+	6.00	1.24	3.12	1.56	0.08	6.00	1.46	3.19	7.00	0.35
^{47}Ca	$7/2^-$	6.00	1.66	3.42	0.85	0.07	6.00	1.93	3.79	7.00	0.28
^{48}Ca	0^+	6.00	1.68	3.54	0.71	0.07	6.00	1.96	3.83	7.92	0.29
^{49}Ca	$3/2^-$	6.00	1.73	3.59	0.62	0.05	6.00	1.98	3.87	7.95	1.20
^{50}Ca	0^+	6.00	1.76	3.61	0.58	0.05	6.00	1.98	3.76	7.93	2.33
^{51}Ca	$3/2^-$	6.00	1.82	3.70	0.46	0.03	6.00	2.00	3.98	8.00	3.03
^{52}Ca	0^+	6.00	1.86	3.74	0.39	0.02	6.00	2.00	4.00	8.00	4.00

Table A.4: Occupation numbers of the valence orbits for the Ca isotopes calculated via the zbm2 interaction.

Isotope	g.s.	$\pi\ d_{5/2}+d_{3/2}$	$\pi\ s_{1/2}$	$\pi\ f_{7/2}$	$\pi\ p_{3/2}$	$\nu\ d_{5/2}+d_{3/2}$	$\nu\ s_{1/2}$	$\nu\ f_{7/2}$	$\nu\ p_{3/2}$
^{40}Ca	0^+	9.73	1.87	0.27	0.13	9.73	1.87	0.27	0.13
^{41}Ca	$7/2^-$	9.75	1.88	0.25	0.12	9.81	1.91	1.19	0.09
^{42}Ca	0^+	9.23	1.61	0.77	0.39	9.57	1.78	2.30	0.35
^{43}Ca	$7/2^-$	9.54	1.77	0.46	0.23	9.80	1.93	3.09	0.19
^{44}Ca	0^+	9.11	1.56	0.89	0.44	9.78	1.89	4.00	0.34
^{45}Ca	$7/2^-$	9.57	1.79	0.43	0.21	9.94	1.97	4.89	0.20
^{46}Ca	0^+	9.60	1.80	0.40	0.20	9.98	1.98	5.78	0.26
^{47}Ca	$7/2^-$	9.95	1.98	0.05	0.02	10.00	2.00	6.83	0.16
^{48}Ca	0^+	10.00	2.00	0.00	0.00	10.00	2.00	7.80	0.20
^{49}Ca	$3/2^-$	10.00	2.00	0.00	0.00	10.00	2.00	7.88	1.12
^{50}Ca	0^+	10.00	2.00	0.00	0.00	10.00	2.00	7.86	2.15
^{51}Ca	$3/2^-$	10.00	2.00	0.00	0.00	10.00	2.00	7.98	3.02
^{52}Ca	0^+	10.00	2.00	0.00	0.00	10.00	2.00	8.00	4.00

Table A.5: Occupation numbers of the valence orbits for the Ca isotopes calculated via the SDPF-U-MIX interaction.

Isotope	g.s.	$\pi\ f_{7/2}$	$\pi\ p_{3/2}$	$\pi\ f_{5/2}$	$\pi\ p_{1/2}$	$\nu\ f_{7/2}$	$\nu\ p_{3/2}$	$\nu\ f_{5/2}$	$\nu\ p_{1/2}$	$\nu\ g_{9/2}$	$\nu\ d_{5/2}$
^{50}Mn	0^+	4.23	0.43	0.27	0.07	4.23	0.43	0.27	0.07	0.00	0.00
^{51}Mn	$5/2^-$	4.45	0.28	0.22	0.05	5.29	0.32	0.32	0.07	0.00	0.00
^{52}Mn	6^+	4.57	0.17	0.22	0.04	6.44	0.23	0.28	0.05	0.00	0.00
^{53}Mn	$7/2^-$	4.65	0.10	0.22	0.03	7.40	0.22	0.32	0.06	0.00	0.00
^{54}Mn	3^+	4.64	0.23	0.09	0.03	7.57	0.95	0.26	0.21	0.00	0.00
^{55}Mn	$5/2^-$	4.60	0.21	0.15	0.04	7.54	1.29	0.70	0.46	0.00	0.00
^{56}Mn	3^+	4.44	0.35	0.18	0.03	7.40	1.96	1.21	0.43	0.00	0.00
^{57}Mn	$5/2^-$	4.46	0.36	0.16	0.03	7.27	2.50	1.73	0.51	0.00	0.00
^{58}Mn	1^+	4.47	0.35	0.15	0.02	7.58	2.85	2.04	0.53	0.00	0.00
^{59}Mn	$5/2^-$	4.57	0.30	0.13	0.02	7.85	3.58	2.26	0.59	0.00	0.00
^{60}Mn	1^+	4.60	0.27	0.11	0.02	8.00	3.70	2.69	0.37	0.20	0.04
^{61}Mn	$5/2^-$	4.45	0.33	0.19	0.03	8.00	3.66	2.46	0.51	1.16	0.21
^{62}Mn	1^+	4.36	0.36	0.25	0.04	8.00	3.76	2.77	0.51	1.65	0.30
^{63}Mn	$5/2^-$	4.34	0.37	0.25	0.04	8.00	3.78	2.88	0.63	2.26	0.45
^{64}Mn	1^+	4.16	0.46	0.32	0.06	8.00	3.82	2.80	0.46	3.17	0.75
^{65}Mn	$5/2^-$	4.29	0.40	0.27	0.04	8.00	3.89	3.51	0.66	3.26	0.69

Table A.6: Occupation numbers of the valence orbits for the Mn isotopes. The interaction used is the GXPF1a for the isotopes $^{50-59}$Mn isotopes, while the LNPS for the remaining ones.

Isotope	g.s.	$\pi\ f_{7/2}$	$\pi\ p_{3/2}$	$\pi\ f_{5/2}$	$\pi\ p_{1/2}$	$\nu\ f_{7/2}$	$\nu\ p_{3/2}$	$\nu\ f_{5/2}$	$\nu\ p_{1/2}$	$\nu\ g_{9/2}$	$\nu\ d_{5/2}$
^{54}Ni	0^+	7.43	0.29	0.22	0.05	5.62	0.19	0.16	0.03	0.00	0.00
^{55}Ni	$7/2^-$	7.55	0.24	0.18	0.03	6.66	0.19	0.13	0.02	0.00	0.00
^{56}Ni	0^+	7.60	0.22	0.16	0.03	7.60	0.22	0.16	0.03	0.00	0.00
^{57}Ni	$3/2^-$	7.51	0.29	0.15	0.04	7.64	1.08	0.21	0.07	0.00	0.00
^{58}Ni	0^+	7.40	0.38	0.16	0.06	7.66	1.41	0.73	0.19	0.00	0.00
^{59}Ni	$3/2^-$	7.39	0.40	0.14	0.07	7.75	2.29	0.70	0.25	0.00	0.00
^{60}Ni	0^+	7.29	0.49	0.15	0.07	7.76	2.33	1.53	0.38	0.00	0.00
^{61}Ni	$3/2^-$	7.12	0.64	0.16	0.08	7.75	2.48	2.30	0.46	0.00	0.00
^{62}Ni	0^+	7.16	0.62	0.14	0.08	7.84	2.82	2.59	0.74	0.00	0.00
^{63}Ni	$1/2^-$	7.23	0.59	0.12	0.06	7.88	3.32	2.72	1.08	0.00	0.00
^{64}Ni	0^+	7.50	0.37	0.10	0.03	7.92	3.22	4.03	0.83	0.00	0.00
^{65}Ni	$5/2^-$	7.44	0.35	0.18	0.03	8.00	3.68	4.20	0.64	0.45	0.03
^{66}Ni	0^+	7.47	0.32	0.18	0.03	8.00	3.71	4.62	0.90	0.73	0.04
^{67}Ni	$1/2^-$	7.71	0.15	0.12	0.01	8.00	3.90	5.56	1.04	0.46	0.03
^{68}Ni	0^+	7.75	0.11	0.12	0.01	8.00	3.91	5.60	1.76	0.67	0.05
^{70}Ni	0^+	7.50	0.25	0.22	0.03	8.00	3.92	5.56	1.63	2.75	0.14

Table A.7: Occupation numbers of the valence orbits for the Ni isotopes as calculated via the GXPF1a interaction for the $^{54-64}$Ni isotopes and the the LNPS interaction for the remaining ones.

Appendix B

Radii Dataset

In this appendix the data use for the fit of the Duflo-Zuker phenomenological formula will be reported in Appendix B.

Z	N	r_π [fm]	Δr_π [fm]	Z	N	r_π [fm]	Δr_π [fm]	Z	N	r_π [fm]	Δr_π [fm]
1	1	1.959	0.006	11	18	2.979	0.016	20	23	3.428	0.006
1	2	1.556	0.050	11	19	3.005	0.021	20	24	3.454	0.006
2	1	1.762	0.050	11	20	3.060	0.014	20	25	3.428	0.006
2	2	1.468	0.002	12	12	2.920	0.010	20	26	3.430	0.006
3	3	2.442	0.050	12	13	2.885	0.011	20	27	3.405	0.006
3	4	2.273	0.050	13	14	2.933	0.015	20	28	3.412	0.006
4	5	2.395	0.012	14	14	2.995	0.025	20	30	3.455	0.006
5	5	2.305	0.050	14	15	2.985	0.020	21	24	3.458	0.005
5	6	2.284	0.025	14	16	3.036	0.021	22	24	3.522	0.005
6	6	2.343	0.005	15	16	3.085	0.010	22	25	3.510	0.005
6	7	2.326	0.010	16	16	3.152	0.015	22	26	3.512	0.005
6	8	2.390	0.020	16	18	3.183	0.010	22	27	3.486	0.004
7	7	2.411	0.025	16	20	3.188	0.010	22	28	3.487	0.005
7	8	2.490	0.010	17	20	3.294	0.017	23	28	3.514	0.040
8	8	2.610	0.008	18	16	3.282	0.025	24	26	3.576	0.004
8	10	2.628	0.020	18	17	3.280	0.025	24	28	3.561	0.003
9	10	2.787	0.010	18	18	3.307	0.020	24	29	3.574	0.004
10	8	2.821	0.030	18	19	3.308	0.020	24	30	3.597	0.006
10	9	2.860	0.015	18	20	3.320	0.010	25	30	3.623	0.010
10	10	2.857	0.010	18	21	3.326	0.020	26	28	3.610	0.010
10	11	2.819	0.015	18	22	3.346	0.015	26	30	3.659	0.010
10	12	2.800	0.020	18	28	3.356	0.030	26	31	3.673	0.010
10	13	2.755	0.025	19	19	3.355	0.008	26	32	3.696	0.010
10	14	2.745	0.030	19	20	3.363	0.005	27	32	3.712	0.010
10	15	2.775	0.035	19	21	3.367	0.006	28	30	3.690	0.008
10	16	2.771	0.035	19	22	3.382	0.006	28	32	3.725	0.010
10	17	2.811	0.040	19	23	3.382	0.006	28	33	3.735	0.010
11	9	2.854	0.015	19	24	3.386	0.006	28	34	3.751	0.010
11	10	2.898	0.012	19	25	3.387	0.006	28	36	3.776	0.010
11	11	2.869	0.011	19	26	3.390	0.006	29	34	3.799	0.012
11	12	2.877	0.009	19	27	3.385	0.006	29	36	3.831	0.010
11	13	2.856	0.011	19	28	3.383	0.006	30	34	3.850	0.012
11	14	2.859	0.010	20	19	3.394	0.016	30	36	3.870	0.012
11	15	2.876	0.010	20	20	3.412	0.006	30	38	3.883	0.012
11	16	2.898	0.011	20	21	3.409	0.006	30	40	3.912	0.010
11	17	2.925	0.012	20	22	3.442	0.006				

Table B.1: Experimental set of data employed for the fit of the Duflo-Zuker phenomenologcal formula (Eq. (3.9), Eq. (3.7)).

Bibliography

[1] Martin Rahm, Roald Hoffmann, and N. W. Ashcroft. "Atomic and Ionic Radii of Elements 1–96". In: *Chemistry – A European Journal* 22.41 (2016), pp. 14625–14632. DOI: https://doi.org/10.1002/chem.201602949. eprint: https://chemistry-europe.onlinelibrary.wiley.com/doi/pdf/10.1002/chem.201602949. URL: https://chemistry-europe.onlinelibrary.wiley.com/doi/abs/10.1002/chem.201602949.

[2] M. Tanaka et al. "Swelling of Doubly Magic ^{48}Ca Core in Ca Isotopes beyond $N = 28$". In: *Phys. Rev. Lett.* 124 (10 Mar. 2020), p. 102501. DOI: 10.1103/PhysRevLett.124.102501. URL: https://link.aps.org/doi/10.1103/PhysRevLett.124.102501.

[3] H. De Vries, C.W. De Jager, and C. De Vries. "Nuclear charge-density-distribution parameters from elastic electron scattering". In: *Atomic Data and Nuclear Data Tables* 36.3 (1987), pp. 495–536. ISSN: 0092-640X. DOI: https://doi.org/10.1016/0092-640X(87)90013-1. URL: https://www.sciencedirect.com/science/article/pii/0092640X87900131.

[4] A.N. Bohr and B.R. Mottelson. *Nuclear Structure (In 2 Volumes)*. World Scientific Publishing Company, 1998. ISBN: 9789813105126. URL: https://books.google.it/books?id=NNZQDQAAQBAJ.

[5] I. Angeli and K.P. Marinova. "Table of experimental nuclear ground state charge radii: An update". In: *Atomic Data and Nuclear Data Tables* 99.1 (2013), pp. 69–95. ISSN: 0092-640X. DOI: https://doi.org/10.1016/j.adt.2011.12.006. URL: https://www.sciencedirect.com/science/article/pii/S0092640X12000265.

[6] H. Heylen et al. "Changes in nuclear structure along the Mn isotopic chain studied via charge radii". In: *Phys. Rev. C* 94 (5 Nov. 2016), p. 054321. DOI: 10.1103/PhysRevC.94.054321. URL: https://link.aps.org/doi/10.1103/PhysRevC.94.054321.

[7] Ronald Fernando Garcia Ruiz et al. "Unexpectedly large charge radii of neutron-rich calcium isotopes". In: *Nature Physics* 12.6 (2016), pp. 594–598.

[8] B. A. Marsh et al. "Characterization of the shape-staggering effect in mercury nuclei". In: *Nature Physics* 14.12 (2018), pp. 1163–1167. DOI: 10.1038/s41567-018-0292-8. URL: https://doi.org/10.1038/s41567-018-0292-8.

[9] G. Ulm et al. "Isotope shift of182Hg and an update of nuclear moments and charge radii in the isotope range181Hg-206Hg". In: *Zeitschrift für Physik A Atomic Nuclei* 325.3 (1986), pp. 247–259. DOI: 10.1007/BF01294605. URL: https://doi.org/10.1007/BF01294605.

[10] H. De Witte et al. "Nuclear Charge Radii of Neutron-Deficient Lead Isotopes Beyond $N = 104$ Midshell Investigated by In-Source Laser Spectroscopy". In: *Phys. Rev. Lett.* 98 (11 Mar. 2007), p. 112502. DOI: 10.1103/PhysRevLett.98.112502. URL: https://link.aps.org/doi/10.1103/PhysRevLett.98.112502.

[11] Jim Al-Khalili. "An Introduction to Halo Nuclei". In: vol. 651. Aug. 2004, pp. 77–112. ISBN: 978-3-540-22399-3. DOI: 10.1007/978-3-540-44490-9_3.

[12] J. Duflo and A. P. Zuker. "Mirror displacement energies and neutron skins". In: *Physical Review C* 66.5 (Nov. 2002). DOI: 10.1103/physrevc.66.051304. URL: https://doi.org/10.1103%2Fphysrevc.66.051304.

[13] J. Bonnard, S. M. Lenzi, and A. P. Zuker. "Neutron Skins and Halo Orbits in the *sd* and *pf* shells". In: *Phys. Rev. Lett.* 116.21 (2016), p. 212501. DOI: 10.1103/PhysRevLett.116.212501. arXiv: 1601.02168 [nucl-th].

[14] J. Bonnard and A. P. Zuker. "Radii in the sd shell and the 1s1/2 "halo" orbit: A game changer". In: *Journal of Physics: Conference Series* 1023.1 (May 2018), p. 012016. DOI: 10.1088/1742-6596/1023/1/012016. URL: https://dx.doi.org/10.1088/1742-6596/1023/1/012016.

[15] Maria Goeppert Mayer. "On Closed Shells in Nuclei. II". In: *Phys. Rev.* 75 (12 June 1949), pp. 1969–1970. DOI: 10.1103/PhysRev.75.1969. URL: https://link.aps.org/doi/10.1103/PhysRev.75.1969.

[16] Otto Haxel, J. Hans D. Jensen, and Hans E. Suess. "On the "Magic Numbers" in Nuclear Structure". In: *Phys. Rev.* 75 (11 June 1949), pp. 1766–1766. DOI: 10.1103/PhysRev.75.1766.2. URL: https://link.aps.org/doi/10.1103/PhysRev.75.1766.2.

[17] Roger D. Woods and David S. Saxon. "Diffuse Surface Optical Model for Nucleon-Nuclei Scattering". In: *Phys. Rev.* 95 (2 July 1954), pp. 577–578. DOI: 10.1103/PhysRev.95.577. URL: https://link.aps.org/doi/10.1103/PhysRev.95.577.

[18] E. Caurier et al. "The shell model as a unified view of nuclear structure". In: *Reviews of Modern Physics* 77.2 (June 2005), pp. 427–488. DOI: 10.1103/revmodphys.77.427. URL: https://doi.org/10.1103%2Frevmodphys.77.427.

[19] T.T.S. Kuo and G.E. Brown. "Structure of finite nuclei and the free nucleon-nucleon interaction: An application to 18O and 18F". In: *Nuclear Physics* 85.1 (1966), pp. 40–86. ISSN: 0029-5582. DOI: https://doi.org/10.1016/0029-5582(66)90131-3. URL: https://www.sciencedirect.com/science/article/pii/0029558266901313.

[20] S.K. Bogner, T.T.S. Kuo, and A. Schwenk. "Model-independent low momentum nucleon interaction from phase shift equivalence". In: *Physics Reports* 386.1 (Oct. 2003), pp. 1–27. DOI: 10.1016/j.physrep.2003.07.001. URL: https://doi.org/10.1016%2Fj.physrep.2003.07.001.

[21] B. Alex Brown and W. A. Richter. "New "USD" Hamiltonians for the *sd* shell". In: *Phys. Rev. C* 74 (3 Sept. 2006), p. 034315. DOI: 10.1103/PhysRevC.74.034315. URL: https://link.aps.org/doi/10.1103/PhysRevC.74.034315.

[22] Etienne Caurier and Frederic Nowacki. "Present Status of Shell Model Techniques". In: *Acta Physica Polonica B* 30.3 (Mar. 1999), p. 705.

[23] Cornelius Lanczos. "An iteration method for the solution of the eigenvalue problem of linear differential and integral operators". In: (1950).

[24] R. R. Whitehead et al. "Computational Methods for Shell-Model Calculations". In: *Advances in Nuclear Physics*. Ed. by Michel Baranger and Erich Vogt. Boston, MA: Springer US, 1977, pp. 123–176. ISBN: 978-1-4615-8234-2. DOI: 10.1007/978-1-4615-8234-2_2. URL: https://doi.org/10.1007/978-1-4615-8234-2_2.

[25] E Caurier et al. "Shell model description of isotope shifts in calcium". In: *Physics Letters B* 522.3-4 (Dec. 2001), pp. 240–244. DOI: 10.1016/s0370-2693(01)01246-1. URL: https://doi.org/10.1016%2Fs0370-2693%2801%2901246-1.

[26] E. Caurier, F. Nowacki, and A. Poves. "Merging of the islands of inversion at $N = 20$ and $N = 28$". In: *Phys. Rev. C* 90 (1 July 2014), p. 014302. DOI: 10.1103/PhysRevC.90.014302. URL: https://link.aps.org/doi/10.1103/PhysRevC.90.014302.

[27] M. Honma et al. "Shell-model description of neutron-rich pf-shell nuclei with a new effective interaction GXPF 1". In: *The European Physical Journal A - Hadrons and Nuclei* 25.1 (2005), pp. 499–502. DOI: 10.1140/epjad/i2005-06-032-2. URL: https://doi.org/10.1140/epjad/i2005-06-032-2.

[28] S. M. Lenzi et al. "Island of inversion around ^{64}Cr". In: *Phys. Rev. C* 82 (5 Nov. 2010), p. 054301. DOI: 10.1103/PhysRevC.82.054301. URL: https://link.aps.org/doi/10.1103/PhysRevC.82.054301.

[29] B. H. Wildenthal, M. S. Curtin, and B. A. Brown. "Predicted features of the beta decay of neutron-rich sd-shell nuclei". In: *Phys. Rev. C* 28 (3 Sept. 1983), pp. 1343–1366. DOI: 10.1103/PhysRevC.28.1343. URL: https://link.aps.org/doi/10.1103/PhysRevC.28.1343.

[30] A. Poves and A. Zuker. "Theoretical spectroscopy and the fp shell". In: *Physics Reports* 70.4 (1981), pp. 235–314. ISSN: 0370-1573. DOI: https://doi.org/10.1016/0370-1573(81)90153-8. URL: https://www.sciencedirect.com/science/article/pii/0370157381901538.

[31] Morten Hjorth-Jensen, Thomas T.S. Kuo, and Eivind Osnes. "Realistic effective interactions for nuclear systems". In: *Physics Reports* 261.3 (1995), pp. 125–270. ISSN: 0370-1573. DOI: https://doi.org/10.1016/0370-1573(95)00012-6. URL: https://www.sciencedirect.com/science/article/pii/0370157395000126.

[32] S. Kahana, H. C. Lee, and C. K. Scott. "Effect of Woods-Saxon Wave Functions on the Calculation of $A = 18, 206, 210$ Spectra with a Realistic Interaction". In: *Phys. Rev.* 180 (4 Apr. 1969), pp. 956–966. DOI: 10.1103/PhysRev.180.956. URL: https://link.aps.org/doi/10.1103/PhysRev.180.956.

[33] EP Wigner. "Proceedings of the Robert A. Welch Foundation Conference on Chemical Research". In: (1957).

[34] J A Nolen and J P Schiffer. "Coulomb Energies". In: *Annual Review of Nuclear Science* 19.1 (1969), pp. 471–526. DOI: 10.1146/annurev.ns.19.120169.002351. eprint: https://doi.org/10.1146/annurev.ns.19.120169.002351. URL: https://doi.org/10.1146/annurev.ns.19.120169.002351.

[35] D.R. Entem and R. Machleidt. "Accurate nucleon–nucleon potential based upon chiral perturbation theory". In: *Physics Letters B* 524.1 (2002), pp. 93–98. ISSN: 0370-2693. DOI: https://doi.org/10.1016/S0370-2693(01)01363-6. URL: https://www.sciencedirect.com/science/article/pii/S0370269301013636.

[36] M. Enciu et al. "Extended $p_{3/2}$ Neutron Orbital and the $N = 32$ Shell Closure in ^{52}Ca". In: *Phys. Rev. Lett.* 129 (26 Dec. 2022), p. 262501. DOI: 10.1103/PhysRevLett.129.262501. URL: https://link.aps.org/doi/10.1103/PhysRevLett.129.262501.

[37] J. L. Friar and J. W. Negele. "Theoretical and Experimental Determination of Nuclear Charge Distributions". In: *Advances in Nuclear Physics: Volume 8*. Ed. by Michel Baranger and Erich Vogt. Boston, MA: Springer US, 1975, pp. 219–376. ISBN: 978-1-4757-4398-2. DOI: 10.1007/978-1-4757-4398-2_3. URL: https://doi.org/10.1007/978-1-4757-4398-2_3.

[38] Peter J. Mohr, Barry N. Taylor, and David B. Newell. "CODATA recommended values of the fundamental physical constants: 2010". In: *Rev. Mod. Phys.* 84 (4 Nov. 2012), pp. 1527–1605. DOI: 10.1103/RevModPhys.84.1527. URL: https://link.aps.org/doi/10.1103/RevModPhys.84.1527.

[39] J. Retamosa et al. "Shell model study of the neutron-rich nuclei around $N = 28$". In: *Physical Review C* 55.3 (Mar. 1997), pp. 1266–1274. DOI: 10.1103/physrevc.55.1266. URL: https://doi.org/10.1103%2Fphysrevc.55.1266.

[40] D. T. Yordanov et al. "Nuclear Charge Radii of $^{21-32}$Mg". In: *Phys. Rev. Lett.* 108 (4 Jan. 2012), p. 042504. DOI: 10.1103/PhysRevLett.108.042504. URL: https://link.aps.org/doi/10.1103/PhysRevLett.108.042504.

[41] Felix Sommer et al. "Charge Radii of ^{55,56}Ni Reveal a Surprisingly Similar Behavior at $N = 28$ in Ca and Ni Isotopes". In: *Phys. Rev. Lett.* 129 (13 Sept. 2022), p. 132501. DOI: 10.1103/PhysRevLett.129.132501. URL: https://link.aps.org/doi/10.1103/PhysRevLett.129.132501.

[42] S. Malbrunot-Ettenauer et al. "Nuclear Charge Radii of the Nickel Isotopes $^{58-68,70}$Ni". In: *Phys. Rev. Lett.* 128 (2 Jan. 2022), p. 022502. DOI: 10.1103/PhysRevLett.128.022502. URL: https://link.aps.org/doi/10.1103/PhysRevLett.128.022502.

[43] S. J. Novario et al. "Charge radii of exotic neon and magnesium isotopes". In: *Phys. Rev. C* 102 (5 Nov. 2020), p. 051303. DOI: 10.1103/PhysRevC.102.051303. URL: https://link.aps.org/doi/10.1103/PhysRevC.102.051303.

[44] Data extracted using the National nuclear data center World Wide Web site from the evaluated nuclear structure data file. URL: https://www.nndc.bnl.gov/ensdf/.

[45] X.Y. Liu et al. "Spectroscopy of 2565,67Mn: Strong coupling in the N=40 "island of inversion"". In: *Physics Letters B* 784 (2018), pp. 392–396. ISSN: 0370-2693. DOI: https://doi.org/10.1016/j.physletb.2018.06.067. URL: https://www.sciencedirect.com/science/article/pii/S0370269318305239.

[46] H. Heylen et al. "Spins and magnetic moments of ^{58,60,62,64}Mn ground states and isomers". In: *Phys. Rev. C* 92 (4 Oct. 2015), p. 044311. DOI: 10.1103/PhysRevC.92.044311. URL: https://link.aps.org/doi/10.1103/PhysRevC.92.044311.

[47] T. Baugher et al. "In-beam γ-ray spectroscopy of ^{63}Mn". In: *Phys. Rev. C* 93 (1 Jan. 2016), p. 014313. DOI: 10.1103/PhysRevC.93.014313. URL: https://link.aps.org/doi/10.1103/PhysRevC.93.014313.

[48] T. Marchi et al. "Quadrupole Transition Strength in the ^{74}Ni Nucleus and Core Polarization Effects in the Neutron-Rich Ni Isotopes". In: *Phys. Rev. Lett.* 113 (18 Oct. 2014), p. 182501. DOI: 10.1103/PhysRevLett.113.182501. URL: https://link.aps.org/doi/10.1103/PhysRevLett.113.182501.

Acknowledgments

I would like to extend my sincere thanks to my supervisor Prof. Silvia Monica Lenzi for all her help, advice and her insightful comments and suggestions.

I would also like to thank my colleagues and friends, who accompanied me along this path, from the very beginning. Without the sharing of our work this goal would have not been possible to reach.

I am also very grateful for my parents who, among all the beautiful things they have done for me, gave me the possibility to study here in Padova.
Then, I would like to tank my sister Marta and my cousin Fabrizio, who always supported and helped me.

I am grateful for my family, whom without I would not be the person I am today.
I have to thank you for giving me the opportunity to better myself, while having the best support someone might need.

A special thank to Miriam, whom with I had the opportunity to share my studies, and also my life.
I am so very grateful for everything you do for me and Luce everyday.